Silicon for Solar Cells

Part I: Oxidative refining of carbon and boron from liquid silicon

Part II: Si_3N_4- and SiC inclusion formation in industrially produced multi-crystalline silicon

Thesis submitted in partial fulfilment of the requirements for the degree Doktor Ingeniør

Department of Materials Technology
Norwegian University of Science and Technology
www.ntnu.no

Anne-Karin Søiland

October 2004

IMT-report 2004:65

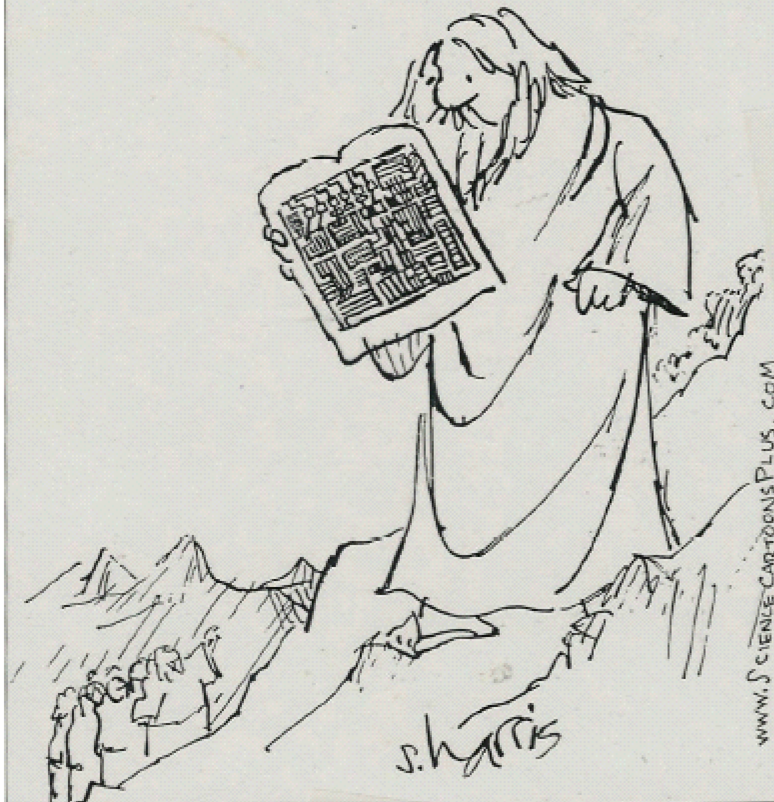

Cartoon by Sidney Harris

PREFACE

This thesis work has been conducted mostly at the Norwegian Technical University in the period from 2000-2004. It was a part of the research project From Sand to Solar Cells. It has been funded by the Norwegian Research Council, Næringslivets idéfond for NTNU, ScanWafer ASA, Sintef Materials and Chemistry, and Elkem. The work was interrupted by a maternity leave in 2002.

Part I on the oxidative refining of carbon and boron was a collaboration with the SINTEF Materials and Chemistry group. After two experiments it was decided to close this project. The results of these two experiments were presented in a paper in the Proceedings for the 17th European Photovoltaic Solar Energy Conference and Exhibition, Münich 2001. This paper is enclosed in Part I of this book, which also covers a discussion of the oxidative removal of carbon from liquid silicon.

Part II of this thesis covers the main work which is SiC- and Si_3N_4- inclusion formation in multi-crystalline silicon ingots. This work was initiated in collaboration with ScanWafer ASA, a supplier of multi-crystalline silicon wafers for the photo-voltaic industry. One part of the experimental work was conducted in industry at ScanWafer ASA's plant in Glomfjord. The second part, the characterisation work on the material produced was carried out at the university. The experimental work in industry consisted of collecting melt samples during the crystallisation of silicon ingots. This was a challenging and interesting experimental work. I am grateful to have had this opportunity, and the staff in Glomfjord was very helpful and made my stays pleasant. The sampling was conducted during normal production runs. It has the advantage of being as close to "real" industrial conditions as possible. However, "jumping" into production runs in this manner has the drawback that you have to accept conditions as they are.

Parts of this thesis have previously been published:

1) Søiland A.K., J.K.Tuset, R.Jensen, S.Prytz and I.Solheim (2001), *Removal of carbon and boron from liquid silicon by the use of a plasma arc*, 17th European Photovoltaic Solar Energy Conference and Exhibition, Vol. II, 1780-1782

2) Søiland A.K., E.J.Øvrelid, T.A.Engh, O.Lohne, J.K.Tuset and Ø.Gjerstad (2004), *SiC and Si_3N_4 inclusions in multicrystalline silicon ingots*, Materials Science in Semiconductor Processing, Vol.7, 39-43

3) Søiland A.K., E.J.Øvrelid, O.Lohne, J.K.Tuset, T.Engh and Ø.Gjerstad (2004), *Carbon and nitrogen contents and inclusion formation during crystallisation of multi-crystalline silicon*, Proceedings for the 19th European Photovoltaic Solar Energy Conference and Exhibition, Paris June 2004, in press

ACKNOWLEDGEMENTS

I profoundly thank my supervisors Prof. Otto Lohne and Prof.Em. Johan Kristian Tuset for their suggestions, guidance and fruitful discussions throughout this work. I am very grateful to Prof.Em. Thorvald Abel Engh for being a technical supervisor on parts of this thesis work. I also thank him for encouragement and inspiration.

At Sintef Materials and Chemistry department thanks are due to the following people for cooperation, assistance and discussions; Pål Tetlie, Ingeborg Solheim, Steinar Prytz, Irene Bragstad, John Åge Byberg, Wilhelm Dall, Dr.Ola Raaness, Morten Raaness, Dr. Eivind Johannes Øvrelid, Dr. Aud Nina Wærness, Tor J.Wærøe and Dr.Roar Jensen. I profoundly thank Eivind for his interest and many good proposals with regard to this work (Part II).

At ScanWafer ASA, my thanks go first to Øivind Gjerstad and Dr. Erik Sauar for making part II of this work possible, and for discussions and input in the field. I thank Bertil Johansen for invaluable help with the coordination of the experiments with the production staff, and for the minority carrier lifetime measurements of the blocks. I profoundly acknowledge the whole staff at Glomfjord, and particularly, the operators assisting me during the melt sampling experiments. They are also acknowledged for keeping me awake during night work when crime-literature failed! Furthermore, I thank Dr. Harsharn Singh Tathgar and Paul Christian Hjemås for many nice discussions and interest in the work. Thanks are also due to Prof.David Hukin and Dr.Franz Hugo for interest and comments on the work.

I thank Dr. Bart Geerligs at ECN and Dr.Maurizio Acciarri at UniMiB for participation in the round robin test, and for discussion of the results. Bart is also thanked for giving valuable information when starting up the measurements. Thanks goes also to Eirik Ottesen at SiNor AS for his FTIR measurements.

John Rasmus Leinum is thanked for his help on the Electron Backscatter Diffraction analysis. I also thank Jan Arve Båtnes and Bjørn Olsen with team for valuable technical assistance. Prof.Em. Ketil Motzfeldt is thanked for his comments on part I of this work.

I thank friends and colleagues of the “round lunch table” at the institute for a nice ambience. Thanks are also due to Øyvind Mjøs and Dr.Gaute Stokkan, my sweetest solar colleagues ;-) for numerous discussions in and out of the field. The project leaders Prof. Georg Hagen and Dr.Espen Olsen of “From Sand to Solar Cells” and “Si-cost reduction”, respectively, are thanked for enthusiastic spirits. The financial support from the project partners is greatly acknowledged.

Finally, thanks go to my dearest Fred, who has been supportive and given me optimism when this was needed. I also “thank” our two “trolls” for getting mummy out of bed on lazy mornings:.......STÅ OPP!

Trondheim October 2004,

Anne-Karin Søiland

SUMMARY

This thesis work consists of two parts, each with a different motivation. Part II is the main part and was partly conducted in industry, at ScanWafer ASA's plant no.2 in Glomfjord.

The large growth in the Photo Voltaic industry necessitates a dedicated feedstock for this industry, a socalled Solar Grade (SoG) feedstock, since the currently used feedstock rejects from the electronic industry can not cover the demand. Part I of this work was motivated by this urge for a SoG- feedstock. It was a cooperation with the Sintef Materials and Chemistry group, where the aim was to study the kinetics of the removal reactions for dissolved carbon and boron in a silicon melt by oxidative gas treatment. The main focus was on carbon, since boron may be removed by other means. A plasma arc was employed in combination with inductive heating. The project was, however, closed after only two experiments. The main observations from these two experiments were a significant boron removal, and the formation of a silica layer on the melt surface when the oxygen content in the gas was increased from 2 to 4 vol%. This silica layer inhibited further reactions.

Multi-crystalline (mc) silicon produced by directional solidification constitutes a large part of the solar cell market today. Other techniques are emerging/developing and to keep its position in the market it is important to stay competitive. Therefore increasing the knowledge on the material produced is necessary. Gaining knowledge also on phenomenas occurring during the crystallisation process can give a better process control.

Part II of this work was motivated by the industry reporting high inclusion contents in certain areas of the material. The aim of the work was to increase the knowledge of inclusion formation in this system. The experimental work was divided into three different parts;

1) Inclusion study
2) Extraction of melt samples during crystallisation, these were to be analysed for carbon- and nitrogen. Giving thus information of the contents in the liquid phase during soldification.
3) Fourier Transform Infrared Spectroscopy (FTIR)-measurements of the substitutional carbon contents in wafers taken from similar height positions as the

melt samples. Giving thus information of the dissolved carbon content in the solid phase.

The inclusion study showed that the large inclusions found in this material are β-SiC and β-Si_3N_4. They appear in particularly high quantities in the top-cuts. The nitrides grow into larger networks, while the carbide particles tend to grow on the nitrides. The latter seem to act as nucleating centers for carbide precipitation. The main part of inclusions in the top-cuts lie in the size range from 100- 1000 µm in diameter when measured by the Coulter laser diffraction method.

A method for sampling of the melt during crystallisation under reduced pressure was developed, giving thus the possibility of indicating the bulk concentration in the melt of carbon and nitrogen. The initial carbon concentration was measured to ~30 and 40 ppm mass when recycled material was employed in the charge and ~ 20 ppm mass when no recycled material was added. Since the melt temperature at this initial stage is ~1500 °C these carbon levels are below the solubility limit. The carbon profiles increase with increasing fraction solidified. For two profiles there is a tendency of decreasing contents at high fraction solidified.

For nitrogen the initial contents were 10, 12 and 44 ppm mass. The nitrogen contents tend to decrease with increasing fraction solidified. The surface temperature also decreases with increasing fraction solidified. Indicating that the melt is saturated with nitrogen already at the initial stage. The proposed mechanism of formation is by dissolution of coating particles, giving a saturated melt, where β-Si_3N_4 precipitates when cooling. Supporting this mechanism are the findings of smaller nitride particles at low fraction solidified, that the precipitated phase are β-particles, and the decreasing nitrogen contents with increasing fraction solidified.

The carbon profile for the solid phase goes through a maximum value appearing at a fraction solidified from 0.4 to 0.7. The profiles flatten out after the peak and attains a value of ~ 8 ppma. This drop in carbon content is associated with a precipitation of silicon carbide. It is suggested that the precipitation of silicon carbide occurs after a build-up of carbon in the solute boundary layer.

FTIR-measurements for substitutional carbon and interstitial oxygen were initiated at the institute as a part of the work. A round robin test was conducted, with the Energy Research Centre of the Netherlands (ECN) and the University of Milano-Bicocci (UniMiB) as the participants. The measurements were controlled against Secondary Ion Mass Spectrometer analyses. For oxygen the results showed a good correspondence between the FTIR-measurements and the SIMS. For carbon the SIMS-measurements were significantly lower than the FTIR-measurements. This is probably due to the low resistivity of the samples (~1 Ω cm), giving free carrier absorption and an overestimation of the carbon content.

LIST OF ABBREVIATIONS AND SYMBOLS

MC	Multi-crystalline
SC	Single-crystalline
MG	Metallurgic Grade
SoG	Solar Grade
EG	Electronic Grade
FTIR	Fourier Transform infrared spectroscopy
EBSD	Electron Back Scatter Diffraction
LOM	Light Optical Microscopy
SEM	Scanning Electron Microscopy
EPMA	Electron Probe Micro Analyzer
HEM	Heat Exchange Method
EFG	Edge-defined film-fed growth
EDS	Energy Dispersive Spectroscopy
WDS	Wavelength Dispersive Spectroscopy
SIMS	Secondary Ion Mass Spectrometry
GDMS	Glow Discharge Mass Spectrometry
CZ	Czochralski
FZ	Float zone
ASTM	The American Society for Testing and Materials
FWHM	Full width half maximum
ppma	parts per million atoms
ppm mass	parts per million mass
Re	Reynold’s number
Sc	Schmidt’s number
Sh	Sherwood’s number
k_0	equilibrium distribution coefficient
k_{eff}	effective distribution coefficient
X_s	fractional composition solid

X_l	fractional composition liquid	
f_l	fraction liquid	
ΔG^0	Gibbs standard free energy change	J mol^{-1}
ΔG_f	Gibbs free energy of formation	J mol^{-1}
ΔH^0	Enthalpy change	J mol^{-1}
k_g	mass transfer coefficient in the gas phase	m s^{-1}
v	growth rate	mm h^{-1}
v_c	critical velocity for the interphase	µm s^{-1}
d_0	interatomic distance in the melt	m
r	particle radius	m
c_p	specific heat capacity particle	J kg^{-1} K^{-1}
c_l	specific heat capacity liquid	J kg^{-1} K^{-1}
K	Equilibrium constant	
Ptot	Total pressure	bar
p_{COb}	CO-pressure in the bulk	bar
p_{COi}	CO-pressure at the interface	bar
D	Diffusion coefficient	m^2 s^{-1}
L	Plate length	m
M	Molecular mass	g mol^{-1}
T	Temperature	K
T	Transmittance	
Tp	Peak transmittance	
Tb	Baseline transmittance	

Greek symbols:

µ	viscosity	kg m^{-1}s^{-1}
γ	activity coefficient	
σ_{sg}	interfacial energy solid-gas	N m^{-1}
σ_{lg}	interfacial energy liquid-gas	N m^{-1}
σ_{sl}	interfacial energy solid-liquid	N m^{-1}
σ_{sp}	interfacial energy solid-particle	N m^{-1}

σ_{sl}	interfacial energy solid-liquid	$N\ m^{-1}$
σ_{lp}	interfacial energy liquid-particle	$N\ m^{-1}$
$\Delta\sigma_0=\sigma_{ps}-(\sigma_{pl}+\sigma_{sl})$	interfacial energy difference	$N\ m^{-1}$
λ_p	thermal conductivity particle	$W\ m^{-1}\ K^{-1}$
λ_l	thermal conductivity liquid	$W\ m^{-1}\ K^{-1}$
c_p	specific heat capacity particle	$J\ kg^{-1}\ K^{-1}$
c_l	specific heat capacity liquid	$J\ kg^{-1}\ K^{-1}$
ρ_p	density of particle	$g\ cm^{-3}$
ρ_l	density of liquid	$g\ cm^{-3}$
α	absorption coefficient	
α_p	peak absorption coefficient	
α_b	baseline absorption coefficient	
ν	kinematic viscosity	$m^2\ s^{-1}$
ν_g	gas velocity	$m\ s^{-1}$

TABLE OF CONTENTS

Chapter 1 Introduction 1
1•1 SOLAR GRADE (SoG) SILICON 2
1•2 MULTICRYSTALLINE (MC) SILICON 5

Chapter 2 Theoretical background 11
2•1 SOLUTE PARTITIONING PROCESS 11
2•2 THE Si-C SYSTEM 14
2•2•1 Compounds and phase diagram 14
2•2•2 Carbon solubility in liquid silicon 17
2•2•3 Effect of alloying elements on carbon solubility 23
2•2•4 Carbon solubility in solid silicon and k_0 24
2•3 THE Si-N SYSTEM 25
2•3•1 Phase diagram and compounds 25
2•3•2 Nitrogen solubility in liquid and solid silicon and k_0 26
2•4 IMPORTANT EQUILIBRIA IN THE FURNACE CHAMBER 27
2•4•1 CO-producing reactions 28
2•4•2 CO incorporation in the melt 31
2•5 SiC AND Si_3N_4 PARTICLES IN MC-SILICON 35
2•6 PARTICLE PUSHING BY A PLANE SOLIDIFICATION FRONT 38

Part I: Oxidative refining of carbon and
boron from liquid silicon 47
Chapter 3 Part I: Oxidative refining of carbon and
boron from liquid silicon 49
3•1 OXIDATIVE REFINING OF SILICON WITH RESPECT TO CARBON . . . 56
3•2 CONCLUDING REMARKS 61

Part II: Si_3N_4- and SiC inclusion formation in industrially
produced multi-crystalline silicon 65
Chapter 4 Experimental 67
4•1 FURNACE 67
4•2 CRUCIBLE AND COATING 70
4•3 SAMPLING OF THE MELT 71
4•3•1 Sampling unit for molten metal 71
4•3•2 Sampling procedure 73
4•3•3 Samples for analysis 73

4•3•4 Analyzing technique for the melt samples 74
4•3•5 Contamination sources 75
4•3•6 Fraction solidified and growth rate 76
4•4 CONVECTION IN THE MELT 77
4•5 FTIR-MEASUREMENTS 77
4•5•1 Principle of FTIR-measurements 78
4•5•2 Measurement procedure 79
4•5•3 Calculation of carbon- and oxygen- concentration 82
4•5•4 Factors influencing the measurements 83
4•6 CHARACTERISATION OF INCLUSIONS 85
4•6•1 Mechanical polishing and chemical/mechanical polishing 85
4•6•2 Dissolution. 85
4•6•3 Inclusion analysis 86
4•7 MINORITY CARRIER LIFETIME 87
4•8 EXPERIMENTAL OVERVIEW 87

Chapter 5 Round robin test 93
5•1 RESULTS ROUND ROBIN TEST 93
5•2 SUMMARY 97

Chapter 6 Results 99
6•1 RESULTS FROM THE MELT SAMPLING EXPERIMENTS 99
6•1•1 Test experiment (January-03) 99
6•1•2 Melt sampling experiment no. 1, MS-Exp 1 (March-03) 100
6•1•3 Melt sampling experiment no. 2, MS-Exp 2 (May-03). 103
6•1•4 Melt sampling experiment no. 3, MS-Exp 3
(September-03) : Reduced growth rate, reduced quantity of
recycled material in the feedstock 106
6•1•5 Melt sampling experiment no. 4, MS-Exp 4
(December-03) : Reduced growth rate, “pure” feedstock 109
6•1•6 Nitrogen- and oxygen- analysis of selected melt samples 112
6•1•7 Metallographic studies of selected melt samples 113
6•1•8 Minority carrier life-time measurements of selected blocks 115
6•2 FTIR-MEASUREMENTS OF WAFERS 118
6•3 CHARACTERISATION AND IDENTIFICATION OF INCLUSIONS 121
6•3•1Mechanically polished samples 121
6•3•2 Dissolution experiments 123
6•3•3 Inclusions in filter paper and in chemical-mechanical
polished samples 129
6•3•4 Summary on dissolution experiments 133
6•3•5 Identification of phase modification 133
6•3•6 Cumulative particle size distribution 137

Chapter 7 Discussion 141
7•1 SILICON NITRIDE FORMATION 141
7•1•1 Sources to nitrogen in the melt 141
7•1•2 Nitrogen contents in the melt- comment on the nitrogen solubility 143
7•1•3 Silicon nitride inclusions 145
7•1•4 Effect of the coating on the silicon nitride formation 147
7•2 SILICON CARBIDE FORMATION 150
7•2•1 Carbon contents in the melt. 150
7•2•2 Evolution of carbon concentration in the melt after Scheil equation 155
7•2•3 Silicon carbide inclusions 157
7•3 OXYGEN CONTENTS IN THE MELT 161
7•4 PUSHING OF PARTICLES BY A PLANE FRONT 161
7•5 EFFECTS FROM OTHER ELEMENTS ON THE PRECIPITATION 167
7•6 LOW LIFE-TIME DIP 167
7•7 CARBON SOLUBILITY 168
7•8 TEMPERATURE GRADIENT IN THE MELT 169

Chapter 8 Conclusions and suggestions for further work 177

APPENDIX 1 181
APPENDIX 2 182
APPENDIX 3 183
APPENDIX 4 184
APPENDIX 5 192

Chapter 1 Introduction

During the last years there has been a growing interest in renewable energy. This is not solely due to the necessity for an alternative energy source to fossil fuel, but is also related to the availability of such sources. In addition the environmental benefit is an encouraging factor for these energy sources. Several governments have therefore initiated various programs to encourage and develop the technology for renewable energy sources. These programs have increased the knowledge and use of energy sources as for instance wind, biomass and solar energy. The 70 000 roof program initiated by Japans government has for instance been the driver of Japan's photovoltaic(PV)-expansion. During the last decade the PV industry has experienced a tremendous growth, see Figure 1•1. The sharp market increase the last years is partly due to the governmental programs, and partly due to an increase in effectiveness and a decrease in cost of the solar cell [Komp, 2001].

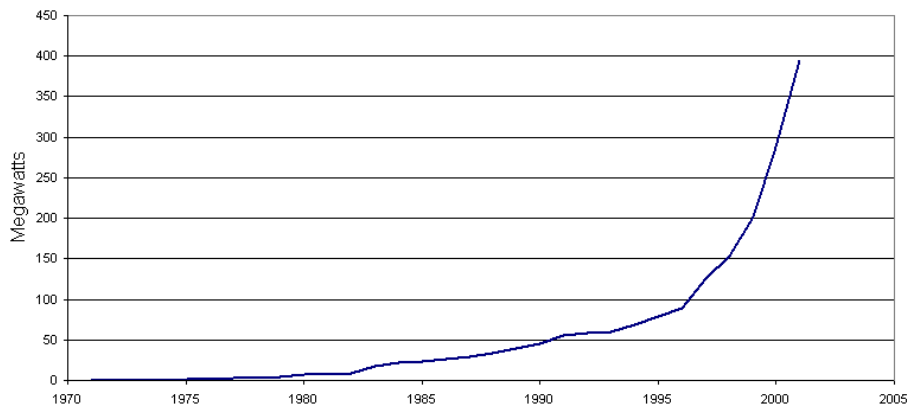

Figure 1•1: World photovoltaic shipments in the period 1971-2001 [Fischowitz-Roberts, 2002].

1•1 Solar Grade (SoG) Silicon

The vast majority of today's solar cells is made of silicon, and the prospect is that it will remain so in the future years as well. Silicon has the physical properties needed, the industry is getting more mature and for the moment is unchallenged by other materials. Silicon is the second most abundant element in the Earth crust, where it is present as different forms of SiO_2 (f.instance as quartz and quartzite). Silicon is produced by carbothermic reduction of silicon dioxide in large arc furnaces. Figure 1•2 gives an illustration of a typical plant for the production of silicon.

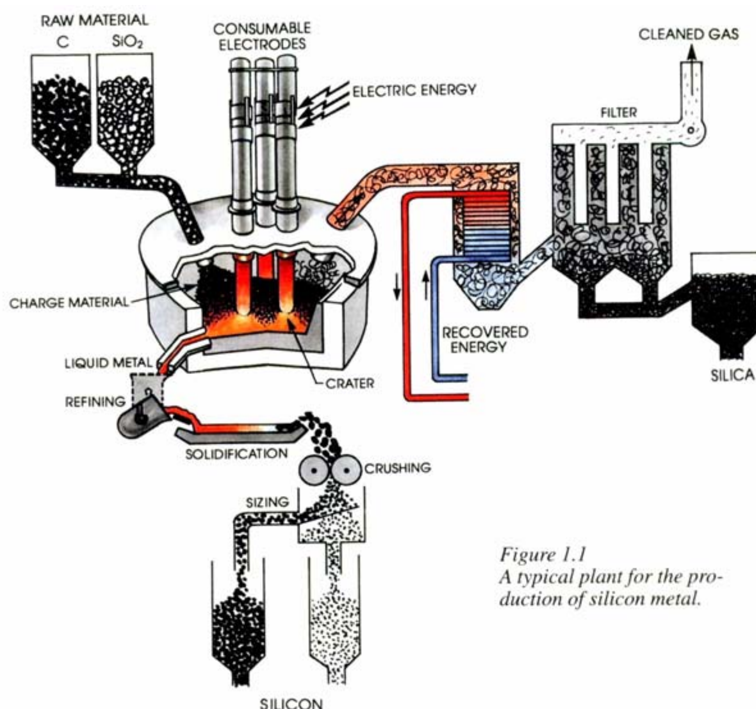

Figure 1•2: Typical plant for the production of silicon metal, from Schei et al. [1998]

The total reduction reaction can be written as:

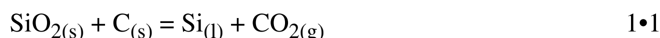

$$SiO_{2(s)} + C_{(s)} = Si_{(l)} + CO_{2(g)} \quad 1•1$$

The silicon resulting from this process is called metallurgical grade (MG) silicon and has a purity of 98-99%. The main impurities are carbon, aluminium, calcium, titanium and iron

[Schei *et al.*, 1992]. The price of MG-Si lies in the range of 0.8-1.5 US $/kg [Luque and Hegedus, 2003]. However, MG-Si is far too impure for electronic- and photovoltaic purposes, but an electronical grade (EG) silicon exists, which is produced by the Siemens process. This product has a purity of 99.9999% and meets the high purity needed for the electronic industry. The raw material for the Siemens process is in fact MG-Si, the silicon is reacted with hydrochloric acid, the reaction is induced by the use of a copper catalyst. The main product obtained is trichlorosilane ($SiHCl_3$), which is purified through fractional destillation. The separated $SiHCl_3$ is decomposed and reduced at high temperature (T >1000 °C), where silicon is deposited on a silicon U-formed rod in a bell jar.

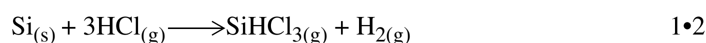

$$Si_{(s)} + 3HCl_{(g)} \longrightarrow SiHCl_{3(g)} + H_{2(g)} \qquad 1•2$$

The product is polycrystalline silicon, or polysilicon as it is frequently referred to. The price of polysilicon is 35-55 US $ /kg [Luque and Hegedus, 2003], which clearly indicates the high cost of the Siemens process.

There is a clear gap both in price and purity between MG-Si and EG-Si, and the idea is that this gap should be filled by a special solar grade (SoG) silicon. What the quality requirements with regard to various elements should be for SoG-Si is not well established. An indication of the purity needed is given in Table 1•1, where the chemical purity of the lowest grade silicon currently purchased to produce multi-crystalline wafers is specified.

Table 1•1: Specification of chemical impurities in lowest-grade silicon currently purchased to produce mc- silicon wafers, from [Luque and Hegedus, 2003]

Impurity	Specification
Fe, Al, Ca, Ti, metallic impurities	Less than 0.1 ppm mass each
C	Less than 4 ppm mass
O	Less than 5 ppm mass
B	Less than 0.3 ppm mass
P	Less than 0.1 ppm mass

. The photovoltaic industry mainly uses rejects from the electronic industry as feedstock. However, this source is no longer sufficient since the photovoltaic industry is in sharp growth. Today there is already a lack in feedstock supply, see Figure 1•3.

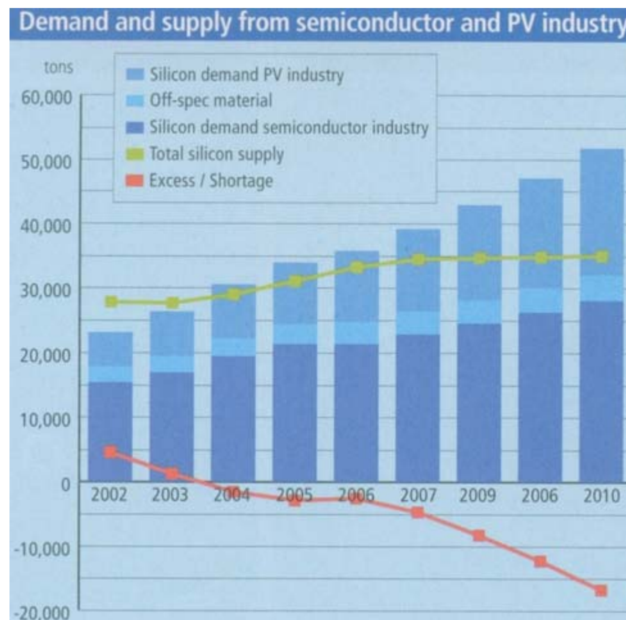

Figure 1•3: Evolution of demand and supply from semiconductor and PV industry [Bernreuter, 2004]

Several companies are currently involved with the development of SoG-Si by different approaches.

Elkem Solar is working with a metallurgical route involving different refining steps, interesting and promising results have been obtained recently [Zahedi *et al.*, 2004]. Another route to SoG-Si that is investigated by SINTEF/ECN through a European project is Si-production from highly pure raw materials; carbon black and high purity quartz. Also, chemical decomposition routes similar to the Siemens route are under development. For instance Wacker Chemie is working with the decomposition of trichlorosilane in a fluidized bed reactor, the result is polysilicon in a granular form [Weidhaus *et al.*, 2004]. Another route to polysilicon is through decomposition of silane (SiH_4), reaction 1•3. The advantage is that the temperature needed for decomposition is lower than for

trichlorosilane and the conversion efficiency is higher. One has also the benefit that corrosive compounds are not formed [Hegedus and Luque, 2003].

$$SiH_{4(g)} = Si_{(l)} + 2H_{2(g)} \quad 1•3$$

None of the above mentioned routes to SoG-Si are yet fully developed to supply the photovoltaic industry with a suitable feedstock. The feedstock issue was the motivation for my initial work on the carbon and boron removal with a plasma arc. Both MG-silicon and silicon from the production by high purity raw materials will contain substantial amounts of carbon.

1•2 Multicrystalline (MC) Silicon

Presently, a large portion of solar cells are made from multi-crystalline material, see Figure 1•4.

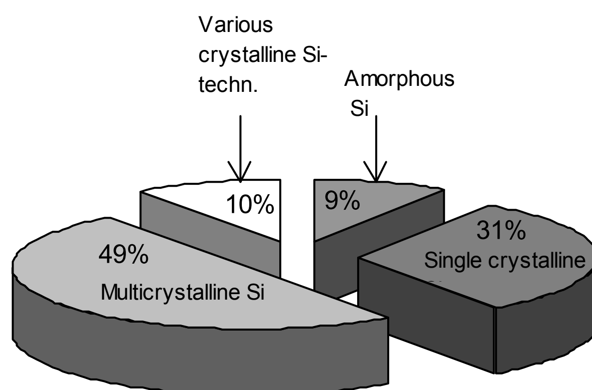

Figure 1•4: Solar modules shipments by technology from 2001, adapted from Luque and Hegedus [2003]

There exists different techniques for the production of mc-wafers, but the dominating techniques are based on directional solidification. In the heat exchanger method (HEM) the crucible is in a fixed position and the solidification proceeds by removal of heat from

the bottom, while in the Bridgman-Stockbarger process the crucible is moving and the heating zone is in a fixed position, see Figure 1•5. Other variants also exist.

Recently developing processes are the electromagnetic continuous pulling (ECMP), which is a crucibleless continuous process [Perichaud *et al.*, 2002], and the block cast technique of larger ingots where the melting and solidification steps use different crucibles [Ghosh *et al.*, 2004].

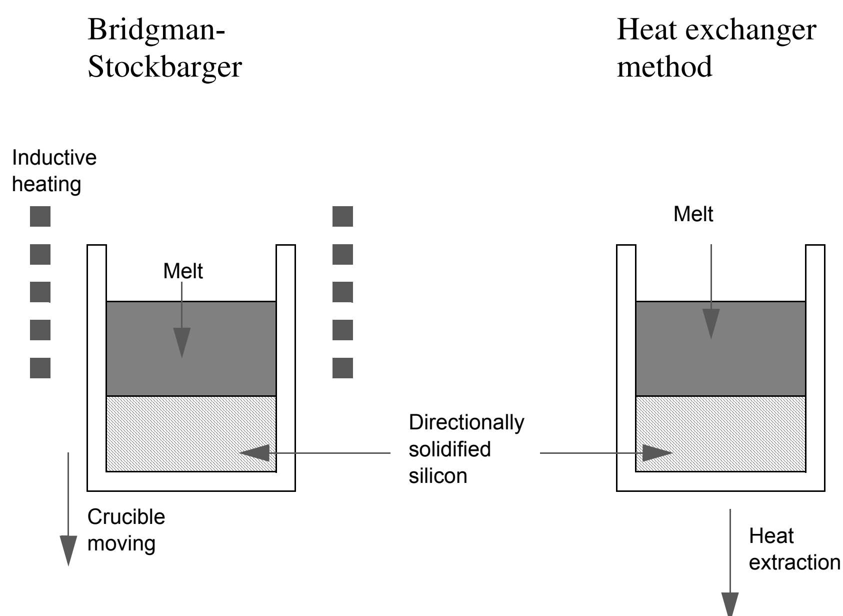

Figure 1•5: Principle sketch of the Bridgman-Stockbarger technique and the Heat exchanger method (HEM)

Although the purity requirements for the photovoltaic industry is lower than for the electronical industry, careful handling and control of the feedstock is necessary when producing silicon ingots for the PV-industry. It is important to avoid contamination of the feedstock throughout the whole process. As already mentioned, there is no dedicated feedstock under production yet for the solar cell industry. Therefore, as feedstock mainly rejects from polysilicon and rejects from crystal growth (single crystals) are still used. To lower the production cost, parts of the ingot produced is recycled into the process (recycled material). A description of these three categories of materials is given in Table 1•2. The carbon and oxygen contents in prime polysilicon was reported to be 0.2~0.4 and

0.9~3.5 ppm mass respectively [Nozaki *et al.*, 1974]. However, when using a mixture of different material types the actual purity level in the feedstock is unknown, at least for certain elements (carbon, oxygen, nitrogen and iron) that are susceptible to being introduced during both the single crystalline and multicrystalline processes .

Table 1•2: Different material categories used as feedstock in mc-industry, adapted from Luque and Hegedus [2003]

Material Category	Type	Description
Rejects from crystal growth (single crystals)	- Tops and tails - Off spec - Remelt - Pot scrap	- End parts of crystal, different resistivity - Multicrystalline crystals, high O-content, crystal defects - Broken single crystal pieces - Silicon from Cz-process with attached quartz
Rejects from polysilicon	- “Popcorn” - “Carbon ends” - Chips - Chunks	- Unacceptable surface structure - Parts of the rod close to the electrical graphite contacts - Small chips generated during processing of rods into chunk form - Chunks and rods from aborted runs, includes purified “carbon ends”
Recycled material	- Multicrystalline ingot parts	- Side cuts, bottom cuts and part of the top cut

The mc-industry producing wafers for PV-purposes is a fairly recent industry. According to Luque and Hegedus [2003] the major cost in producing mc-solar cell panels is the wafer production, where the crystal growth constitutes 35% of the cost in wafer production, see Figure 1•6. Improvements of the process can lead to lower cost. Therefore, to keep the market share in PV and to stay competitive with new developing technologies it is essential to improve the understanding of the actual process and phenomena occuring during solidification.

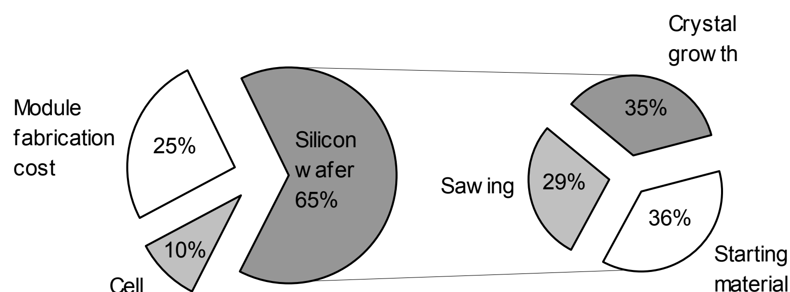

Figure 1•6: Cost distribution for modules and silicon wafers, adapted from Luque and Hegedus, [2003]

At Scanwafer ASAs second plant in Glomfjord a new type of furnace was installed. In some of these furnaces large inclusion contents were observed in occasional runs (visual observation). These inclusions were sometimes found in the middle of the ingot. Also a drop in the lifetime measurements of the blocks was observed occasionally around the same position (Personal communication, Erik Sauar at REC). High inclusion contents may lead to difficulties in the wafer fabrication process. Other consequences are the eventual effects on the solar cell performance, as shunting and lifetime degradation.

At the start of this work these large inclusions were thought to be essentially silicon carbide, since this was the most reported inclusion type in the literature for mc-silicon. This thesis work therefore first aimed at establishing knowledge on the carbon contents in the liquid- and solid phases, and its evolution during solidification. Information on the carbon content give an indication of the potential for forming inclusions in this system. A method to retrieve liquid samples during solidification (under reduced pressure) had to be developed.

It was also important to identify the type of inclusions formed, as well as information on the vertical distribution in the ingot. These findings would be important to elucidate mechanisms behind the formation of large inclusions in the process.

REFERENCES

Bernreuter J. (2004), *The delay A lack of silicon supply for the photovoltaics industry over the next two to three years*, Photon International 6/04, 36-42

Fischowitz-Roberts B. (2002-8), Worldwatch insitute and Earth Policy Institute, June 11 www.earth-policy.org/Updates/Update12_data.htm

Ghosh M., A.Müller and T.Bähr (2004), *Larger ingots for multicrystalline solar silicon wafers*, Proceedings for the 19th European Photovoltaic Solar Energy Conference and Exhibition, in press

Komp R.J. (2001), *Practical Photovoltaics - Electricity from Solar Cells*, 3rd edition, aatec publications

Luque A. and Hegedus (2003), *Handbook of photovoltaic science and engineering*, John Wiley and Sons Ltd

Nozaki T., Y.Yatsurugi, N.Akiyama, Y.Endo and Y.Makide (1974), *Behaviour of light impurity elements in the production of semiconductor silicon*, J.Radioanal.Chem, Vol.19, 109-128

Schei A., H.Rong and A.G.Forwald (1992), *Impurity distribution in silicon*, Silicon for Chemical Industry, Norway, pp 11-23

Schei A., J.K.Tuset and H.Tveit (1998), *Production of high silicon alloys*, Tapir Forlag, Norwegian University of Science and Technology (Trondheim)

Zahedi C., E.Enebakk, K.Friestad, K.Peter and R.Kopcek (2004), *A metallurgical route to solar grade silicon*, Proceedings for the 19th European Photovoltaic Solar Energy Conference and Exhibition, in press

Weidhaus D., E.Schindlbeck and K.Hesse (2004), *Granular polysilicon deposition from trichlorosilane by using a fluidized bed reactor*, Proceedings for the 19th European Photovoltaic Solar Energy Conference and Exhibition, in press

Chapter 2 Theoretical background

In this section relevant theory and literature for the interpretation of the results are presented. This includes: the solute partitioning process, the solubility in the solid and liquid phases of carbon and nitrogen, CO-producing reactions, SiC and Si_3N_4 precipitates reported in multi-crystalline silicon, and particle pushing.

2•1 Solute partitioning process

The solidification of most metals from their melts is closely approximated by the assumption of equilibrium at the interface. If the solidification is occurring at a temperature T, the condition of equilibrium at the interface requires that the liquid and solid compositions at the interface x_l and x_s, respectively, be fixed by the phase diagram [Flemings, 1974], see Figure 2•1. This is the base for the definition of the equilibrium distribution coefficient, k_0, where,

$$k_0 = \frac{x_s}{x_l} \qquad \text{eq•2•1}$$

where x_s is the fractional composition in the solid and x_l the fractional composition of the liquid.

Often the solidus- and liquidus- lines are approximated as straight, then k_0 is constant for a given system.

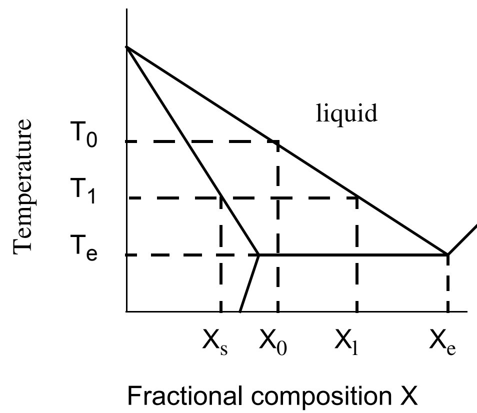

Figure 2•1: Solidification of an alloy with equilibrium at the liquid-solid interface, phase diagram relations adapted from Flemings [1974]

Solidification under the assumption of no solid diffusion and complete mixing in the liquid can be described by the Scheil equation:

$$x_l = x_0 f_l^{(k_0 - 1)} \qquad \text{eq•2•2}$$

where x_l is the fractional composition of the liquid phase, x_0 is the initial composition, f_l is fraction liquid and k_0 is the equilibrium distribution coefficient

A more empirical version of the Scheil equation is obtained by replacing the equilibrium distribution coefficient (k_0) with the effective distribution coefficient (k_{eff}). This is the case when there is some convection present, and a solute boundary layer is formed at the front. Within this layer diffusion is the mechanism for mass transport, and outside the layer the composition is uniform due to convection, see Figure 2•2. The effective distribution coefficient, k_{eff} can be described as:

$$k_{eff} = \frac{k_0}{k_0 + (1 - k_0)e^{-(v\delta / D_l)}} \qquad \text{eq•2•3}$$

where v is the growth rate, δ thickness of the diffusion boundary layer and D_l the liquid diffusivity. It is seen that when v -> 0, k_{eff} -> k_0. To approach equilibrium conditions the solidification must be very slow. However, at a slow solidification rate the validity of the assumption of no diffusion in the solid phase will not be met, and some “back” diffusion will take place.

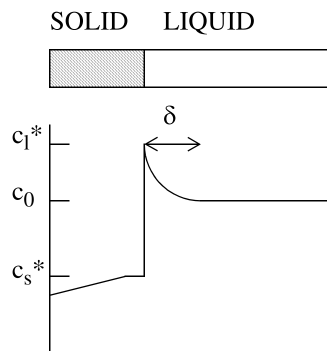

Figure 2•2:Solute profile in the liquid for solidification with convection, from Flemings [1974].

For many systems, k_0 has a value less than unity, so that solute is rejected from the the solid as it forms, and accumulates in the liquid. Plane front solidification is a way of obtaining non-uniform compositions within the material grown. The growth takes place with a plane interface between the solid and liquid phases. In this sense it may be refining, this is also why plane front solidification is widely used for production of mc-silicon.

In the production of mc-ingots there are, however, some elements that may enter during solidification due to reactions between the melt and the atmosphere, coating and crucible. Particularly carbon, nitrogen, oxygen and iron are susceptible of being introduced. When an element is present in a high concentration, for instance it has reached the eutectic composition, the temperature will be invariant, and the liquid will solidify at eutectic composition. Therefore the system is no longer described by the Scheil equation.

2•2 The Si-C system

2•2•1 Compounds and phase diagram

The only stable condensed compound in the binary system is SiC. The eutectic temperature is slightly below the melting point of pure Si, the lowering of the melting point is less than 0.04 °C, see Figure 2•3. The SiC phase occurs in two modifications, α (hexagonal) and β (cubic), the α-modification exists in several polytypes. The density of SiC is reported to be 3.22 g/cm^3 [Lide, 1991-1992]. According to thermochemical data from JANAF Thermochemical tables [Chase *et al.* 1985] the β-phase is most stable for all temperatures, but the stability difference is small, as can be seen from Gibbs free energy of formation in Figure 2•4. The phase diagrams for the system determined by Scace and Slack [1959] and Olesinski and Abbaschian [1984] respectively, are given in Figure 2•5. According to Scace and Slack [1959] SiC decomposes peritectically forming Si with 19 at% C and C at 3103 K (2830 °C), while according to Olesinski and Abbaschian [1984] this reaction occurs at 2818 K (2545 °C) forming Si with 27 at%.

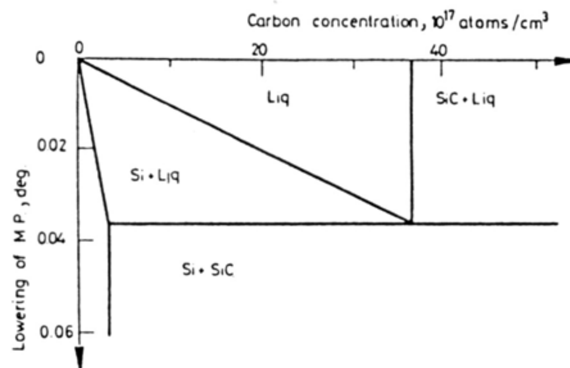

Figure 2•3: Lowering of the melting point in the Si-C phase diagram at extremely low carbon concentrations, from Nozaki et al. [1970]

SiC (α– Silicon Carbide) [85JANAF]

T	$S°$	$H°_{298} - H°_0$	$\Delta_f H°$	$\Delta_f S°$	$\Delta_f G°$
298.15	· 16.485	3252.0	–71546.0	–8.067	–69140.8

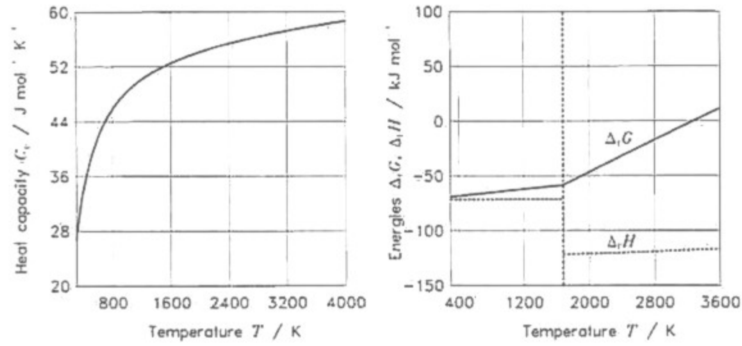

SiC (β– Silicon Carbide) [85JANAF]

T	$S°$	$H°_{298} - H°_0$	$\Delta_f H°$	$\Delta_f S°$	$\Delta_f G°$
298.15	16.610	327.0	–73220.0	–7.942	–70852.1

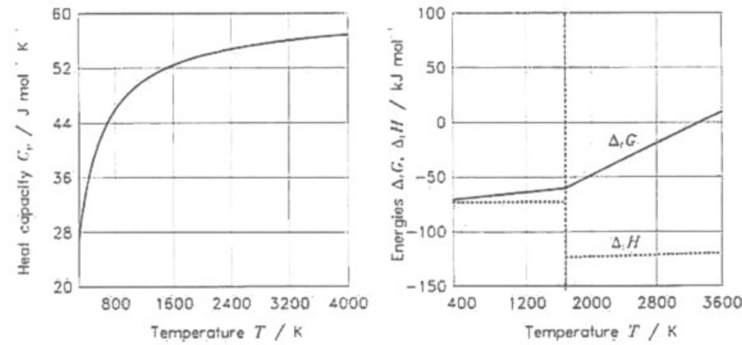

Figure 2•4: Values for the heat capacities and Gibbs free energy of formation as a function of temperature for α- and β-SiC, from JANAF [Chase et al. 1985]

a)

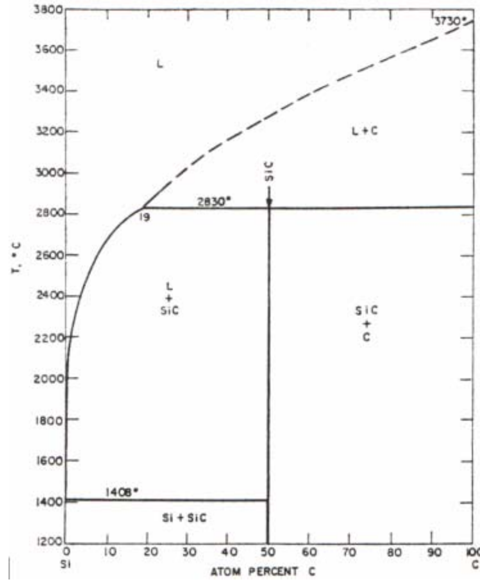

(b)

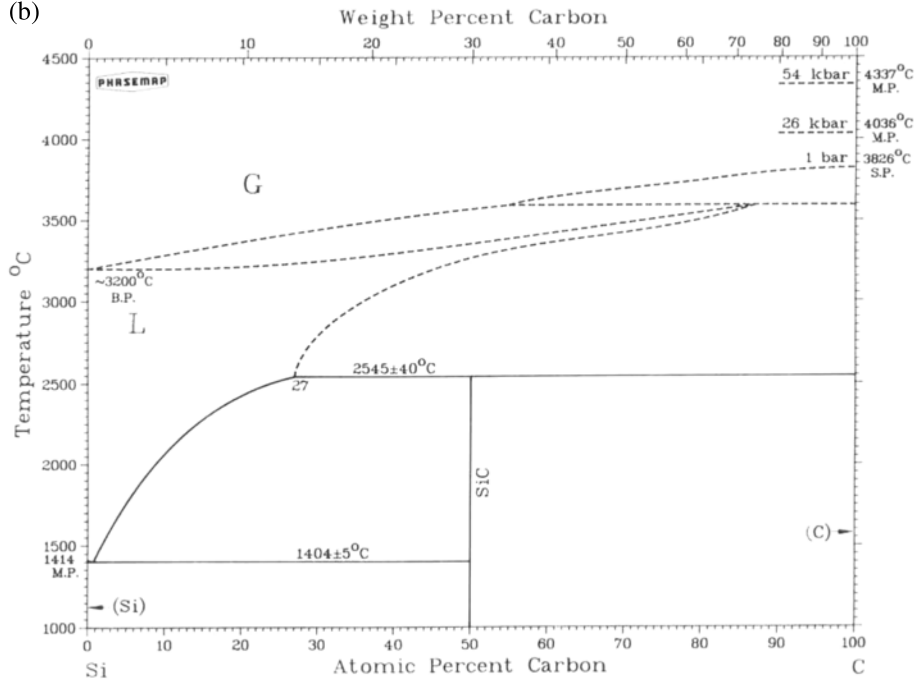

Figure 2•5:Phase diagram of Si-C from a) Scace and Slack [1959] and b) Olesinski and Abbaschian, [1984]

2•2•2 Carbon solubility in liquid silicon

The solubility of carbon in liquid silicon equilibrated with silicon carbide is represented by reaction 2•1.

$$SiC_{(s)} = Si_{(l)} + \underline{C} \quad 2•1$$

This system has two components and two condensed phases. According to Gibbs phase rule (F + Ph = C + 2 or F + Ph_c = C + 1) the system has one degree of freedom (at fixed pressure). Thus if the temperature is fixed the composition of the two phases will be set. By measuring the amount of dissolved carbon in the silicon phase at different temperatures a relation for the carbon solubility as a function of temperature is obtained.

A number of researchers have studied the solubility of carbon in liquid silicon by use of the above mentioned method. They have often used different experimental set-ups and different analyzing techniques as summarized in Table 2•1. There is a considerable variation in the results, up to a factor 10 in difference, see Figure 2•6.

.

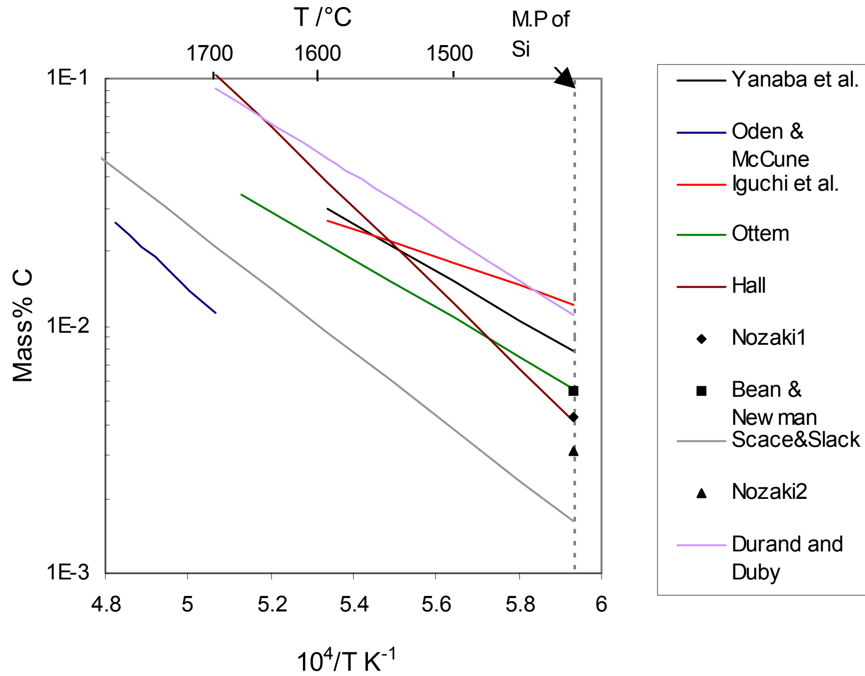

Figure 2•6: Literature survey, the solubility of carbon in liquid silicon as a function of temperature. Extrapolated value at m.p. for Oden and McCune and the calculated value at m.p. from Tang [2003] are not shown, but both lie ~ $5x10^{-4}$ mass% (5 ppm mass)

Both Nozaki *et al.* [1970] and Bean and Newman [1971] measured the solubility of carbon in solid silicon. For comparison with the liquid solubilities we have used the equilibrium distribution coefficient $k_0 = x_s/x_l$ to calculate the liquid solubility from the solid solubility. The equilibrium distribution coefficient (k_0) of carbon between solid and liquid silicon determined to be 0.07±0.01 by Nozaki *et al.* [1970] was used. This value was determined experimentally. Their experimental set-up consisted of passing a molten zone through carbon painted silicon rods. The carbon content was obtained for different zone velocities. From this information the effective distribution coefficient was calculated for the different zone velocities, and the equilibrium distribution coefficient k_0 was obtained by extrapolation to 0 velocity. The calculated value for the liquid solubility employing the solid solubility and k_0 from Nozaki, is 43 ppm mass. This is higher than the value given

by Nozaki in his phase diagram, which is 31 ppm mass. From where or how they obtained this value for the liquid solubility is, however, not mentioned.

Scace and Slack [1959] equilibrated the melt with a graphite container. They determined the carbon content by weighing the SiC formed upon solidification. This involved a rather cumbersome experimental procedure, where the SiC formed by surface reaction had to be removed, followed by a dissolution process to extract the SiC-particles in the matrix. Furthermore they did not take into account the possibility that some of the SiC from dissolved carbon may form close to the container walls, and therefore will not be included in the measurements.

Iguchi and Narushima [1993] and Yanaba *et al.* [1997] have used the same experimental set-up in their measurements. Nevertheless, they have obtained different results for the solubility of carbon. CO was added to the gas stream to reduce the oxygen content in the melt and prevent formation of a SiO_2-film on the surface of Si, which may disturb the SiC/Si equilibrium. However, the effect of CO on the equilibrium may also be argued. It is known that CO may readily dissolve in Si-melts [Endo *et al.*, 1979].

The use of oxide (SiO_2) crucibles in these experiments, as for instance Hall did, has been criticised. Since the oxygen in the melt may react with dissolved carbon and produce CO it can lead to erroneous measurements. Durand and Duby [1999] determined the solubility by extrapolation of solubility data from three different literature sources, one of these was Hall [1958]. The selection was based on a critical judgment of measurements from several different works. The experimental set-up and analyzing methods were different in these three works. Durand and Duby obtained a value of 110 ppm mass by extrapolating the data from the three experimental works. This is more than twice the value obtained when extrapolating Hall's measurements alone. Moreover, their literature survey did not include the works of Ottem [1993], Iguchi *et al.* [1993] and Yanaba *et al.* [1998].

The low solubility obtained by extrapolating the results from Oden and McCune [1987] was explained by Durand and Duby [1999] by the fact "that they removed the outer surface (0.065 mm) of their ingot and that a major portion of the SiC-particles being located close to the external wall because of nucleation conditions". Also Tang [2003] obtained a low value (5 ppm mass) for the solubility of carbon in liquid silicon. Such a low

solubility would mean that the equilibrium distribution coefficient would be around 0.6, taking the solid solubility as 3 ppm mass. This high value for the equilibrium distribution coefficient means that there would hardly be any segregation of carbon during solidification. It is also one order higher than the equilibrium distribution coefficients reported in the literature, see Table 2•2.

Table 2•1: Experimental and calculated values of carbon solubility in liquid silicon equilibrated with silicon carbide, adapted from Yanaba *et al.* [1997]

Investigators	Silicon melting	Analyzing technique	Temperature / K	Solub. at m.p. / mass ppm	Remarks
Yanaba *et al.* and Iguchi *et al.*	SiC-crucible Ar+CO(5%) gas flowing	Combustion IR absorption and coulometric titration	1723-1873	79 123	
Oden and McCune	Graphite crucible Vacuum or Ar	Combustion-IR absorption (?)	1973-2423	5.7	
Bean and Newman	CZ-Si high C-content, annealing at diff. T's	IR-absorption	873-1623	55	From solid sol.
Hall	Silica crucible Ar gas flowing	Gravimetry	1793-1998	41	
Ottem	Silica crucible Ar gas flowing	Combustion-IR absorption	1720-1950	56	
Scace and Slack	Graphite or alumina crucible, Ar gas flowing	Gravimetry	1833-2500	16	
Tang			1685	5	Thermochem. calc.

Table 2•1: Experimental and calculated values of carbon solubility in liquid silicon equilibrated with silicon carbide, adapted from Yanaba *et al.* [1997]

Investigators	Silicon melting	Analyzing technique	Temperature / K	Solub. at m.p. / mass ppm	Remarks
Durand and Duby			1685-3101	110	Extrapol. of data from three sources
Nozaki *et al*. (1)	FZ-Si with carbon painted on the surface	Charged particle act. analysis + IR-absorption	1685	43	From solid sol.
Nozaki *et al.* (2)				31	From phase diag.

The experimental measurements with liquid Si are complex as interaction with the ambient atmosphere and the crucible may disturb the measurements. Since the measurements of the solid solubility involve a crucibleless process and vacuum conditions they may be less affected by experimental sources of errors. In the work of Nozaki *et al.* [1970] the solubility was measured by charged particle analysis and was in good agreement with IR-measurement. Carbon concentration just prior to the appearance of silicon carbide was always found to be 3 ppm mass (3.5 atoms/cm^3) regardless of the quantity of carbon painted on the rod. If we consider this as a fairly accurate measurement and use an equilibrium distribution coefficient for carbon between 0.058 to 0.07 (literature values, see Table 2•2), we obtain a liquid solubility ranging from 43 ppm mass to 52 ppm mass.

Thus, in conclusion it is suggested that based on the above discussions the solubility at the melting point is 40 ppm ± 10 ppm by mass. The solubility values from Ottem [1993], Hall [1958], Bean and Newman [19] and Nozaki [1970] are in reasonable agreement with this range.

2•2•3 Effect of alloying elements on carbon solubility

Yanaba *et al.* [1998] have measured the effect of boron, iron and phosphorous on the carbon solubility in liquid silicon equilibrated with silicon carbide, see Figure 2•7. Both phosphorous and boron increase the carbon solubility, while iron has the opposite effect according to these measurements. Durand and Duby [2000] calculated the solid-liquid equilibria in the silicon rich corner of the Si-O-C system from the solubility data in binary systems using the model of a regular solution. One of their conclusions was that oxygen slightly increases the carbon solubility.

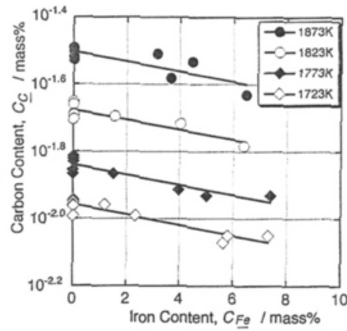

Fig. 1 Effect of iron content on carbon solubility.

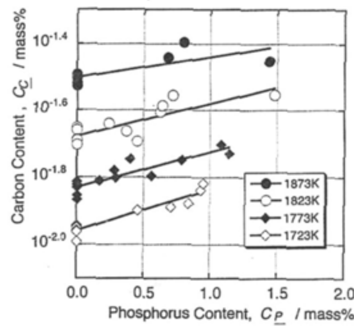

Fig. 2 Effect of phosphorus content on carbon solubility.

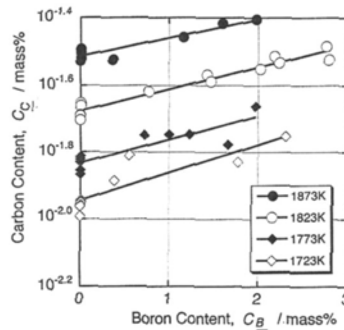

Fig. 3 Effect of boron content on carbon solubility.

Figure 2•7: Effect of alloying element on the solubility of carbon in liquid silicon, from Yanaba et al. [1998]

2•2•4 Carbon solubility in solid silicon and k_0

As previously mentioned Bean and Newman [1971] determined the solid solubility of carbon in silicon in the temperature interval 873-1623 K. Extrapolation to the melting point of silicon gave a value of 3.85 ppm mass for the solid solubility in silicon. Nozaki *et al.* [1970] determined the solubility to 3 ppm mass at the melting point. Thus, there is

good agreement between these measurements. Values for the equilibrium distribution coefficient for carbon in silicon determined by two different investigators are assembled in Table 2•2.

Table 2•2: Equilibrium distribution coefficients for carbonin silicon from literature

k_0	Investigators	Method
0.07 ± 0.01	Nozaki *et al.* [1970]	Low growth rate k_{eff} extrapolation to zero growth rate
0.058 ± 0.005	Kolbesen and Mühlbauer [1982]	Low growth rate k_{eff} extrapolation to zero growth rate

2•3 The Si-N system

2•3•1 Phase diagram and compounds

There is one known compound for this system, Si_3N_4. It crystallises generally in two polymorphs; the trigonal α-phase and the hexagonal β-phase. Recently, a new cubic phase has been discovered, formed at high temperature and pressure [Melendez-Martinez and Dominguez-Rodriguez, 2003, reference therein]. The α-phase has a density of 3.16-3.19 g/cm^3 [Wang *et al.*, 1996], while the β-phase density is 3.19-3.20 g/cm^3 [Riley, 2000]. A tentative phase diagram by Yatsurugi *et al.* [1973] is shown in Figure 2•8. We see that the lowering of the melting point for the eutectic is very small due to the low solubility.

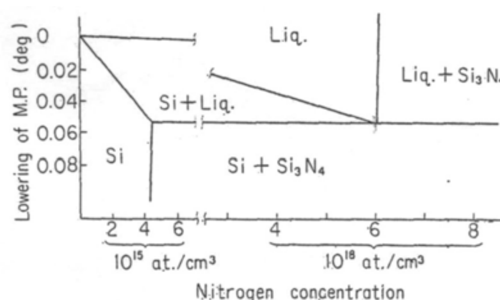

Figure 2•8: Phase diagram of Si-N in the very low N-content corner, from Yatsurugi et al. [1973].

2•3•2 Nitrogen solubility in liquid and solid silicon and k_0

We have found three studies of this system, and these show a large deviation for the liquid solubility, see Table 2•3. Only Yatsurugi *et al.* [1973] has measured the solid solubility and obtained an equilibrium distribution coefficient for nitrogen.

Iguchi and Narushima [1993] studied the liquid solubility by equilibrating silicon contained in a Si_3N_4-container with a N_2:H_2 gas mixture. They measured the solubility at four different temperatures in the interval 1723-1873 K. Their value at the melting point of silicon is an extrapolation of the measurements. Kaiser and Thurmond [1959] measured the nitrogen solubility at one temperature reported to be “in the region of the silicon melting point”. They used a float-zone techniqe, thus crucible-less, where Si_3N_4 was formed in glow discharge or NH_3-gas. The appearance of a glow discharge was explained by a presence of “active nitrogen”. They observed that the reaction rate was greatly enhanced when the glow discharge appeared and that this was caused by active nitrogen having a higher activity in chemical reactions. Iguchi and Narushima [1993] propose that liquid silicon might react with active nitrogen, thus giving higher nitrogen contents than the equilibrium value in the study of Kaiser and Thurmond [1959]. When it comes to the study of Yatsurugi *et al.* [1973] silicon was contained in an evacuated silica ampoule and equilibrated by silicon nitride powder, they measured the nitrogen solubility only at the melting point. The presence of silica and thus oxygen in the system may affect the equilibrium. For silicon in equilibrium with SiO_2 the stable nitride is the Si_2ON_2-phase as seen in Figure 2•9. Also undissolved silicon nitride powder may affect the experimental results.

Table 2•3: Data for nitrogen solubility in silicon and k_0

Investigators	Liquid solubility / ppm mass	Solid solubility / ppm mass	Equilibrium dist. coeff., k_0
Kaiser and Thurmond [1959]	100		
Iguchi and Narushima [1993]	4		
Yatsurugi *et al.* [1973]	60	0.042	$7x10^{-4}$

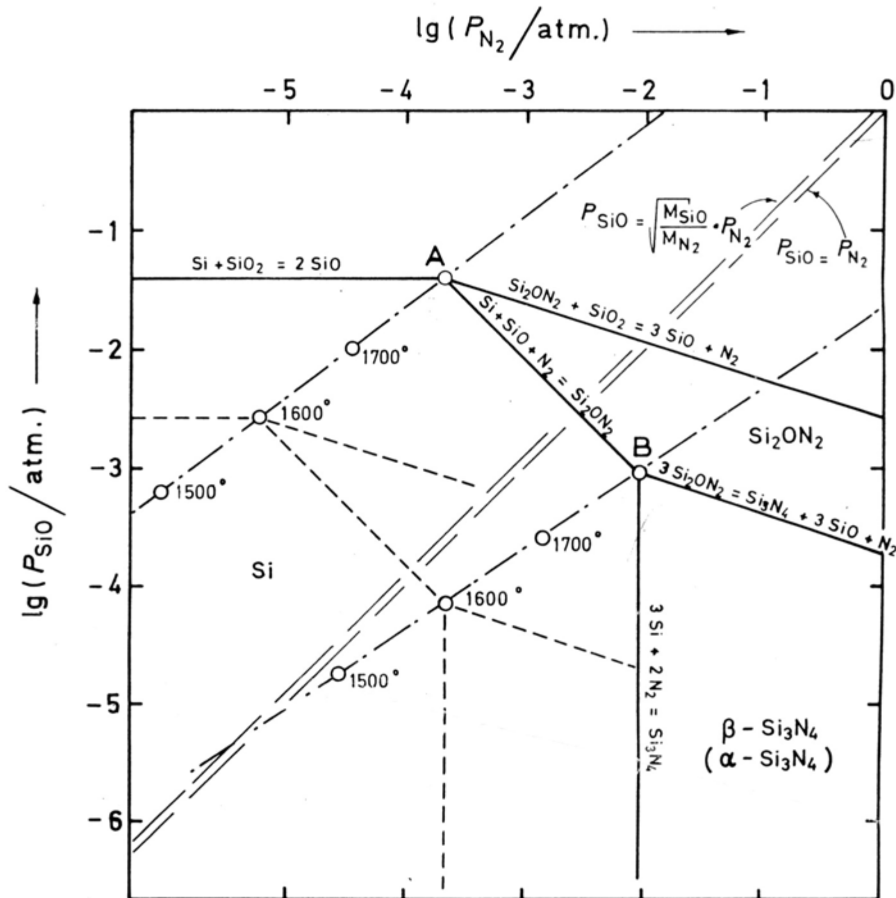

Figure 2•9: Calculated equilibrium diagram for the system Si-O-N at 1800 K. Point A represents coexistence of $Si+SiO_2+Si_2ON_2$, point B $Si+Si_2ON_2+\beta-Si_3N_4$, from Blegen [1976]

2•4 Important equilibria in the furnace chamber

There are numerous equilibria that can occur in a furnace containing silica, graphite components, silicon melt and silicon nitride coating. Especially at elevated temperatures some reactions become important. In this section, the equilibria that are considered of importance for the carbon content in liquid silicon during crystallisation of multicrystalline silicon, are presented. We have found no work discussing the nitrogen uptake in multicrystalline silicon, and proposed routes for this incorporation are therefore in the discussion.

2•4•1 CO-producing reactions

Schmid *et al.* [1979] conducted a thermodynamic analysis of several different reactions that could cause carbon contamination in the melt for a HEM-furnace. They concluded that the major contributors were reactions between the graphite supporter elements and the silica crucible, reactions 2•2 and 2•3. Their conclusions were confirmed by experiments where direct contact between the silica and graphite proved necessary to get a contamination of the melt.

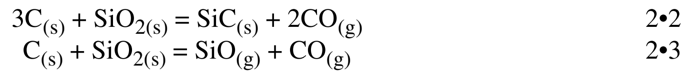

$$3C_{(s)} + SiO_{2(s)} = SiC_{(s)} + 2CO_{(g)} \qquad 2•2$$

$$C_{(s)} + SiO_{2(s)} = SiO_{(g)} + CO_{(g)} \qquad 2•3$$

However, the direct reaction between two solid phases can be questionned. According to Motzfeldt [1988] the reaction between carbon and silicon produces a layer of solid compound silicon carbide and therefore further reaction can occur only by solid diffusion, which is a slow process. He suggested that in vacuum the reaction may take place by thermal dissociation of silica, followed by the reaction between oxygen and carbon.

$$SiO_{2(s)} = SiO_{(g)} + 1/2O_{2(g)} \qquad 2•4$$

When CO is present the reactions proposed by Lee *et al.* [1977] is :

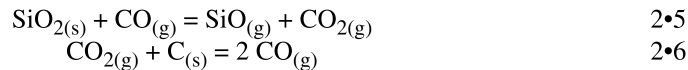

$$SiO_{2(s)} + CO_{(g)} = SiO_{(g)} + CO_{2(g)} \qquad 2•5$$

$$CO_{2(g)} + C_{(s)} = 2\,CO_{(g)} \qquad 2•6$$

The sum of reactions 2•5 and 2•6 gives reaction 2•3. It is probable that reactions 2•2 and 2•3 represents the total reactions and that close contact between the solid phases facilitate the sub-reactions.

The standard Gibbs free energy change for reactions 2•2 and 2•3 at various temperatures are given in Table 2•4, ΔG_f values were taken from JANAF thermochemical tables [Chase, 1985].

Table 2•4: Standard free energy change for reactions 2·2 and 2·3 at different temperatures

Reaction 2.2		*Reaction 2.3*	
T /K	**ΔG^0 /J mol^{-1}**	T /K	**ΔG^0 /J mol^{-1}**
1600	62144	1600	139937
1700	29005	1700	106681
1800	-4001	1800	73672
1900	-36880	1900	40805

The thermodynamic equilibrium constant, K, is expressed as:

$$K = \exp\left(\frac{-\Delta G^0}{R \times T}\right) \qquad \text{eq•2•4}$$

For reaction 2.2 and 2.3 the K is defined as:

$$K_{2.2} = \frac{p_{CO}^2 \times a_{SiC}}{a_C^3 \times a_{SiO_2}} \qquad \text{eq•2•5}$$

$$K_{2.3} = \frac{p_{CO} \times p_{SiO}}{a_c \times a_{SiO_2}} \qquad \text{eq•2•6}$$

P_{CO} can then be calculated from the thermodynamic equilibrium constant, assuming that the activity of the condensed phases are equal to 1, and p_{CO} is equal to p_{SiO} for reaction 2·3 since n_{CO} is equal to n_{SiO}. The dependence of p_{CO} on temperature for the two reactions is then shown in Figure 2•10 below.

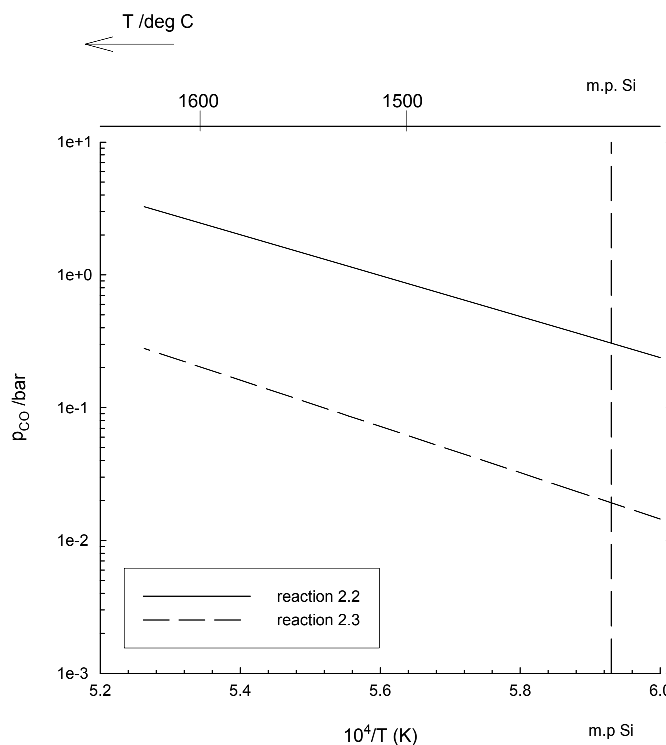

Figure 2•10: P_{CO} as a function of temperature for reactions 2•2 and 2•3.

The thermodynamic equilibrium constant, K, used for calculating the partial pressure of CO is independent of pressure in the furnace chamber. From "Le Chatelier's principle", since the reactions above are gas producing, an increase in P_{tot} means a shift towards reactants. An increase in P_{tot} will thus favour the reactants. The pressure in the process is therefore of importance for both reactions 2•2 and 2•3.

The SiO gas produced by reaction 2•3 may also react with available carbon (graphite) according to reaction and thus contribute in a build-up of the CO-pressure in the furnace atmosphere

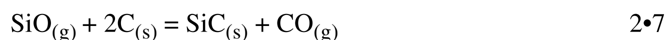

$$SiO_{(g)} + 2C_{(s)} = SiC_{(s)} + CO_{(g)} \qquad 2•7$$

Schmid *et al.* [1979] conducted experiments in a HEM-furnace to verify their thermodynamic analysis. Crystallisation was conducted with both a molybdenum and a graphite retainer, the silicon was contained in a silica crucible, the process was run at a 0.1

Torr ($1.3x10^{-4}$ bar). In the case with a graphite retainer the entire top surface of the ingot was covered with SiC! Dendrite-like precipitates of SiC were also found in the ingot. In the experiment conducted with a molybdenum retainer the top surface of the ingot was clean and shiny with no evidence of SiC-layers. Also the carbon level in this ingot was lower.

CO might of course also come from direct reaction with oxygen and graphite if the furnace chamber is not gas tight, and also from reaction with humidity absorbed on the supporting- and insulation- elements in the furnace.

2•4•2 CO incorporation in the melt

The equilibrium of CO and dissolved carbon and oxygen in liquid silicon has been studied by Endo *et al.* [1979]. They considered the following reaction:

$$\underline{C} + \underline{O} = CO_{(g)} \qquad 2•8$$

$$K_{2.8} = \frac{p_{CO}}{[C]_{Si} \times [O]_{Si}} = 9.6 \times 10^{-8} \qquad eq•2•7$$

where p_{CO} is expressed in atm, and $[C]_{Si}$ and $[O]_{Si}$ in ppma. $K_{2\cdot8}$ is at the m.p. of silicon.

The equilibrium constant was determined experimentally, by finding the CO pressure at carbon and oxygen saturation in the melt. High purity Si with small amounts of β-SiC and SiO_2 powder was sealed in a quartz crucible. The crucible was set in graphite blocks for uniform temperature. Mixtures of He containing a known concentration of CO was bubbled into the melt with various flow rates, and the CO concentration in the outgoing gas was measured. Three different inlet gas mixtures were used. By plotting the CO concentration versus flow rate for each inlet gas and extrapolating the resultant curve to zero flow rate, the equilibrium CO pressure was obtained. The value for $K_{2.8}$ obtained by this method corresponded well with measurements on CZ-crystal growth.

The CO-pressure at the melting point was found to be $3.8x10^{-4}$, when the solubilities were taken to be 90- and 44- ppma for carbon and oxygen respectively. The low equilibrium constant, $K_{2.8}$, means that the equilibrium CO pressure is small. This pressure is shown as a function of temperature in Figure 2•11 . For the inverse reaction, CO incorporation in the melt, the equilibrium constant is $1/K_{2.8}$, thus equal to $1.04x10^{7}$.

From $K_{2.8}$ it is also seen that for a constant oxygen content in the melt the carbon content in the melt is proportional to the ambient CO-pressure.

.

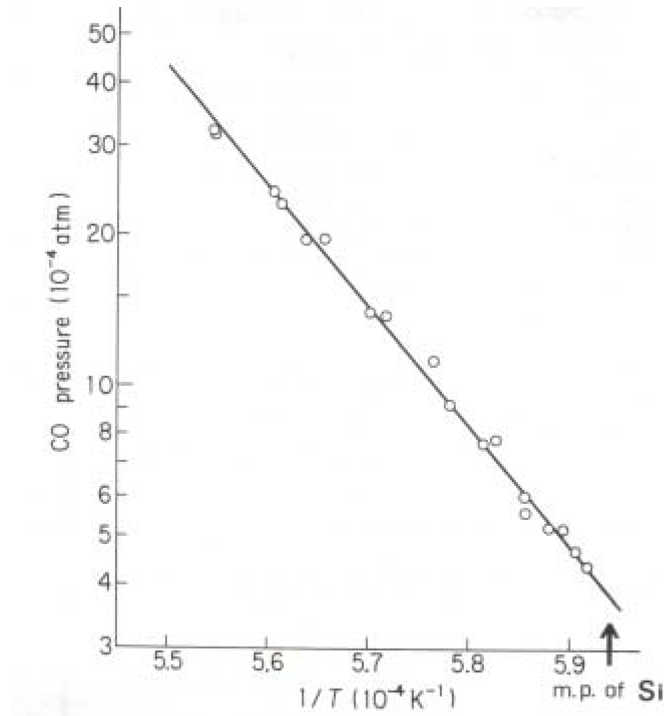

Figure 2•11: Equilibrium CO pressure as a function of temperature, from Endo et al. [1979]

When the melt is saturated with carbon the following equilibrium is considered for the incorporation of carbon:

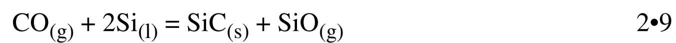

$$CO_{(g)} + 2Si_{(l)} = SiC_{(s)} + SiO_{(g)} \qquad 2•9$$

The equilibrium constant for the reaction is defined by the ratio of the pressure of SiO over the pressure of CO, if the activities of the condensed phases are considered equal to 1.

$$K_{2.9} = \frac{p_{SiO}}{p_{CO}} \qquad eq•2•8$$

Standard free energy change for the reaction at different temperatures is given in Table 2•5 As can be seen from Figure 2•12, the equilibrium p_{SiO}/p_{CO} pressure decreases with increasing temperature, thus a low temperature favours the products. It is worth noting that the P_{tot} has no influence on this equilibrium, since the reactants and the products consist of the same number of gas species

.

Table 2•5: Standard free energy change for reaction 2•9 at different temperatures

Reaction 2•9	
T /K	**ΔG^0 /J mol^{-1}**
1600	-41582
1700	-34117
1800	-26653
1900	-19190

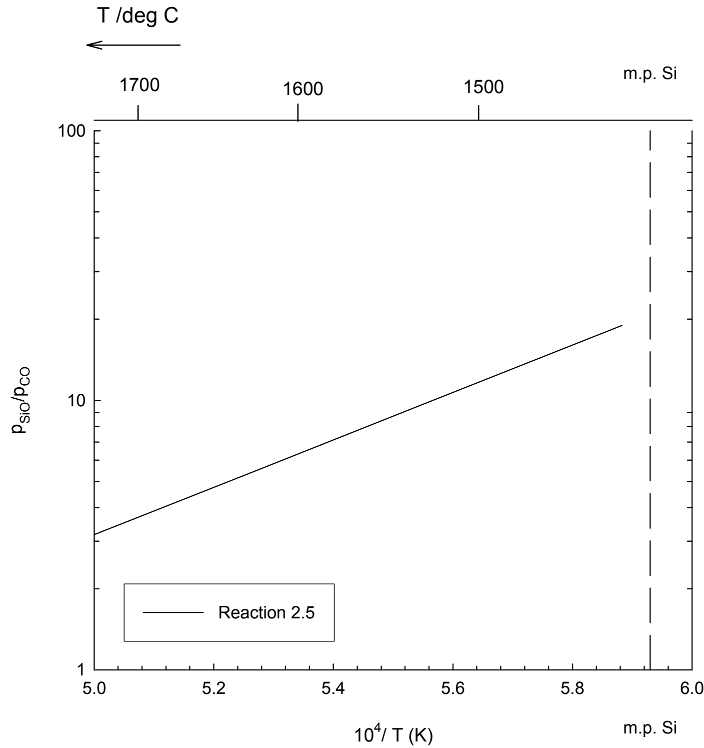

Figure 2•12: Equilibrium p_{SiO}/p_{CO} as a function of temperature for reaction 2•9.

Carlberg *et al.* [1983] presented a model for CO-incorporation in a CZ-melt that was verified with existing experimental data. The model was in reasonable agreement with the experimental data. The carbon concentration curves proved to be sensitive to k_g, the mass transfer coefficient for transport through the ambient atmosphere, see Figure 2•13. Thus, they concluded that the rate-determining step was the transport in the gas phase from the graphite furnace parts to the melt surface. The carbon concentration levels were below 2 ppma for $k_g < 3x10^{-4}$, up to a fraction solidified of 0.9, see Figure 2•13.

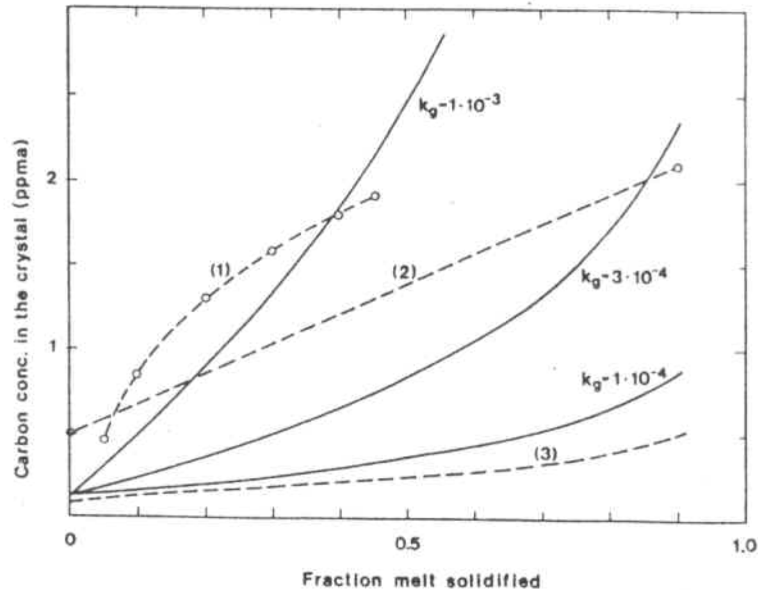

Figure 2•13: Calculated carbon distribution in 10 cm Cz-crystals for different values of k_g, dashed lines show experimental results, from Carlberg [1983].

2•5 SiC and Si_3N_4 particles in mc-silicon

Below the solid solubility limit carbon is incorporated at a substitutional position in the silicon lattice, it is bonded tetrahedrally to silicon atoms. In this position it is electricially neutral [Pivac *et al.*, 1996]. Substitutional carbon gives rise to an IR-band at 607 cm^{-1}, and this band is used to calculate the substitutional carbon content in silicon wafers. Carbon is known for its strong interaction with oxygen forming carbon-oxygen (CO_n) complexes. These complexes give rise to infrared bands [Newman and Smith, 1969]. High carbon contents influences oxygen precipitation as SiO_x-species. This is possibly due to the small size of carbon atom (decrease the volume) while oxygen has an expanding effect because of its larger size.

Supersaturation of carbon in the solid phase has been observed for different manufactureurs of multicrystalline silicon [Schönecker *et al.*, 2004, Pivac *et al.*, 1992]. Solid phase precipitation may occur in material that is supersaturated at a given temperature. Precipitates may then form during cool down or during subsequent processing if suitable nuclei are present. However, precipitation may also occur during the crystallisation process if the liquid phase is enriched in carbon. From a supersaturated liquid primary precipitates may form, and at saturation the eutectic reaction can take place. Particles formed from the melt are frequently observed in edge-defined film-fed (EFG) grown silicon ribbons [f.ins. Dietze *et al.* 1981, Katcki 1987]. In this type of process the SiC-particles grow on the die surface, graphitic dies are used in this process thus resulting in a carbon saturated liquid. The particles are eroded from the die by melt convection during growth and may thereby be included in the ribbon.

Also, in multi-crystalline material produced by other casting processes SiC may form during the casting process. Examples of such particles are shown in Figure 2•14, this material was prepared by a mold-casting technique [Dietze *et al.*, 1981]. Carbon precipitation particularly in EFG-material has been connected to twinning formation [Möller, 2003]. This carbon-induced twinning process generates high internal stresses in the material.

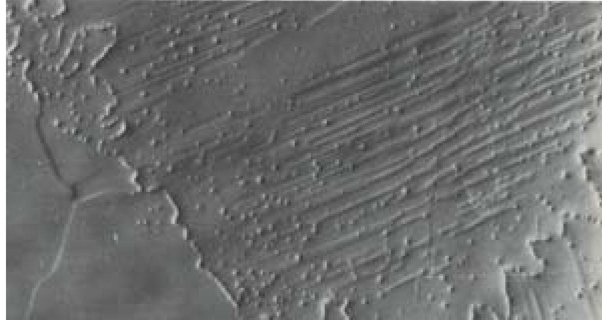

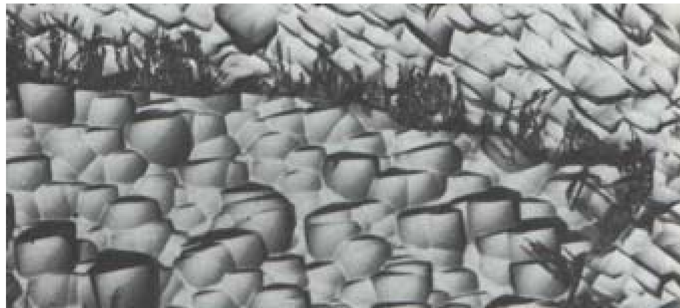

Figure 2•14: a) Optical micrograph of mold-cast Si , mechanically polished surface (35x), dots are SiC-particles b) Etched surface with SiC segregation (200x), from Dietze et al. [1981]

Nitrogen has been much less studied than carbon. It forms various N-O complexes with oxygen [Pivac *et al.*, 1996, reference therein]. In a recent work, silicon nitride precipitation was observed as filament-like precipitates [Lawerenz *et al.*, 2004]. It was assumed that these precipitates grew at the liquid-solid interface from the melt during crystallisation. Also Hejjo Al Rifai *et al*. [2004] report a similar type of filament-like precipitate of Si_3N_4, they also report a second type of silicon nitride precipitate appearing as a monocrystalline rod.

The effects of these inclusions on the solar cell characteristics are not yet well established. Silicon carbides have been connected to shunting activity, but it appeared to be more an effect of the impurities gettering around the particles than to the particles themselves [Rao *et al*., 1976]. The silicon nitrides on the other hand have previously been reported to have no negative effect on the solar cell [Schätzle *et al*., 1993]. Hejjo Al Rifai

et al. [2004] found that SiC-filaments in large-angle grain boundaries caused shunting in the cells studied, but none of the silicon nitride precipitates had such an effect. This is, however, in contrast to the work of Binetti *et al.* [1996], where silicon nitride and iron silicides at the ingot edges were related to lifetime degradation.

2•6 Particle pushing by a plane solidification front

Particles present in a melt can be pushed or engulfed by the plane front. An illustration of particle pushing is given in Figure 2•15. This kind of pushing has been described by Uhlmann *et al.* [1964] as a steady state phenomenon where the particle and the front move with the same velocity, and the gap width between the particle and front remains constant.This gap width is created when the surface energy between the solid and the particle (σ_{sp}) is greater than the solid-liquid (σ_{sl}) and the liquid-particle (σ_{lp}) surface energies, see Figure 2•16. As can be seen from this figure the surface energy increases with decreasing separation between the particle and the solid front, this increase in energy gives the driving force for keeping a gap between the particle and the front. Particle pushing does only occur when the front is moving below a certain velocity, known as the critical velocity (V_c), see Figure 2•17. This velocity increases, in general, with decreasing particle size.

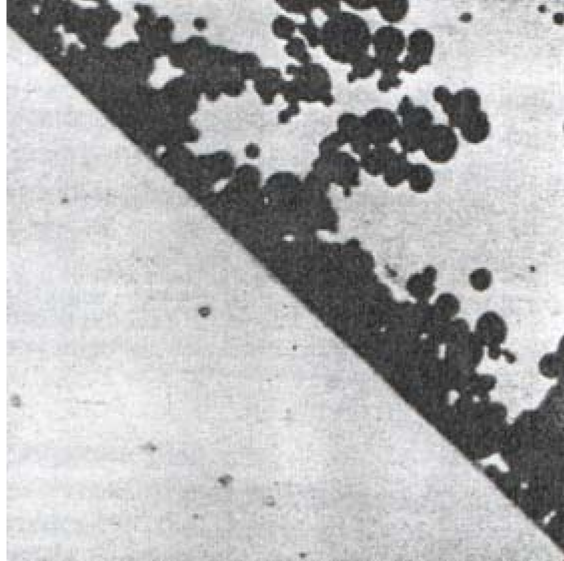

Figure 2•15: Pile-ups of particles at a solid-liquid interface, thymol +Zn, from Uhlmann et al. [1964]

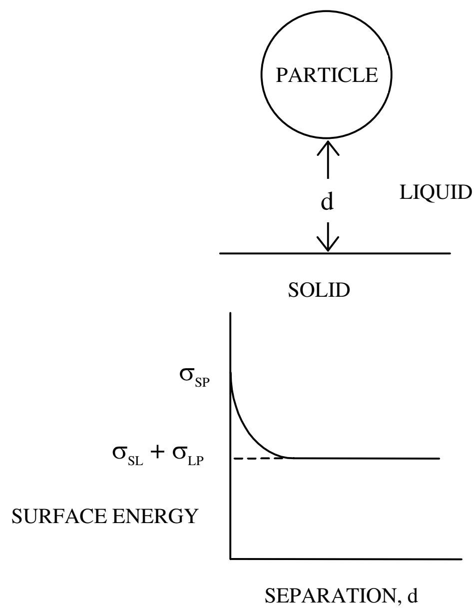

Figure 2•16: Pushing of a particle by a liquid-solid interface. Top: particle at a distance d from the interface, at bottom: surface free energy for the solid-liquid and liquid-particle interfaces vs. d, after Uhlmann et al. [1964].

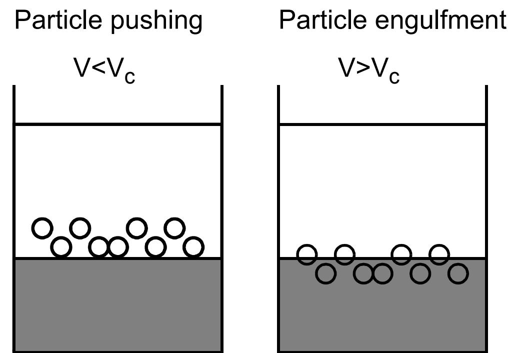

Figure 2•17:Illustration of particle pushing/engulfment as a function of growth rate, V

Several models for calculating V_c have been developed over the last years. Some of them are based on the surface energy theory above, while others also take into account effects like the thermal properties of the particle and the melt, and blocking of solute diffusion from the front by the particles [Sasikumar and Ramamohan, 1991, Kim and Rohatgi, 1998, Stefanescu *et al.* 1990]. Figure 2•18 below, from Kim and Rohatgi [1998], shows some of these models and calculated V_c's for the Al-SiC-system. We see from the figure that the calculated values scatter from 0.180 μm/s to 14800 μm/s for a particle radius of 10μm.

Although several models have been presented to describe the V_c for particle pushing, they seem to have limitations. They do not take into account effects as fluid flow, shape of the growth front, pushing of clusters, and non-spherical particles. They also scatter significantly in calculated V_c for the same system.

Model	Criteria	Calculated results
Uhlman *et al.* [1]	$V = \frac{(n+1)}{2}\left(\frac{La_0 V_0 D_l}{KTR^2}\right)$	$V = 0.18 \times 10^{-6}$ m/s
Chernov *et al.* [4]	$V = \frac{0.14B_3}{\eta R}\left(\frac{\sigma_a}{B_3 R}\right)^{1/3}$; $\frac{\lambda^2}{l} > R$	$V = 1.96 \times 10^{-6}$ m/s
	$V = \frac{0.15B_3}{\eta Rl}$; $\frac{\lambda^2}{l} < R$	$V = 2.38 \times 10^{-6}$ m/s
Cisse and Bolling [2]	$V = \left(\frac{4\Psi(\alpha)KT\sigma_{sl}A_0}{9\pi\eta^2 R^3}\right)^{1/2}$; $R < R_b$	$V = 4.24 \times 10^{-6}$ m/s
Stefanescu [8]	$V = \frac{\Delta\sigma_0 a_0}{6(n-1)\eta R}\left(2 - \frac{k_p}{k_l}\right)$	$V = 3.12 \times 10^{-3}$ m/s $n = 2$
Shangguan [9]	$V = \frac{\Delta\sigma_0 a_0}{6(n-1)\eta\pi R}\left(\frac{n-1}{n}\right)^n$	$V = 9.86 \times 10^{-4}$ m/s $n = 2$
Wu *et al.* [17]	Experimental observation	$V = 1.48 \times 10^{-2}$ m/s
Present Paper Model	Steady state	$V = 3.4 \times 10^{-3}$ m/s

Figure 2•18: Calculated results of V_c for Al-10μm SiC from different models, from Kim and Rohatgi [1998]

REFERENCES

Bean A.R. and R.C.Newman (1971), *The solubility of carbon in pulled silicon crystals*, J.Phys.Chem.Solids., Vol.32, 1211-1219.

Binetti S., M.Acciarri, C.Savigni, A.Brianza, S.Pizzini and A.Musino (1996), *Effect of nitrogen contamination by crucible encapsulation on polycrystalline silicon material quality*, Mat.Sci.Eng., B36 68-72

Blegen K. (1976), *Equilibria and kinetics in the systems Si-N, Si-O-N and Si-C-O-N*, PhD-thesis, Norwegian University of Science and Technology (Trondheim)

Carlberg T. (1983), *A quantitative model for carbon incorporation in czochralski silicon melts*, J.Electrochem.Soc.:Solid-state science and technology, Vol.130, No.1, 168-171.

Chase M.W. Jr., C.A.Davies, J.R.Downey Jr., D.J.Frurip, R.A.McDonald and A.N.Syverud (1985), *JANAF Thermochemical Tables*, Third Edition, Part 1 and 2.

Dietze W., W.Keller and A.Mühlbauer (1981), *5 Crystals Growth, Properties and Applications: Float-Zone Grown Silicon*, Springer-Verlag

Durand F. and J.C.Duby (1999), *Carbon solubility in solid and liquid silicon- A review with reference to eutectic equilibrium*, J.Phase Equil., Vol.20, No.1, 61-63

Durand F. and J.C.Duby (2000), *Solid-liquid equilibria in the silicon rich corner of the Si-O-C system*, J.Phase Equil., Vol.21, No.2, 130-135

Endo Y.m Y.Yatsurugi, Y.Terai and T.Nozaki (1979), *Equilibrium of carbon and oxygen in silicon with carbon monoxide in ambient atmosphere*, J.Electrochem.Soc.:Solid-state science and technology, Vol.126, No.8, 1422-1425.

Flemings M.C. (1974), *Materials Science and Engineering Series Solidification Processing*, McGraw Hill, Inc.

Hall R.N. (1958), *Electrical contacts to silicon carbide*, J.Appl.Phys., Vol.29, No.6, 914-917.

Hejjo Al Rifai M., O.Breitenstein, J.P.Rakatoniaina, M.Werner, A.Kaminski and N. Le Quang (2004), I*nvestigation of material-induced-shunts in block-cast multicrystalline silicon solar cells caused by SiC precipitate filaments*, 19th European Photovoltaic Solar Energy Conference and Exhibition, Paris

Iguchi Y. and T.Narushima. (1993), *Solubility of oxygen, nitrogen and carbon in liquid silicon*, First International Conference on Processing Materials for Properties, The Minerals, Metals & Materials Society, 437-440

Kaiser W. and C.D.Thurmond (1959), *Nitrogen in Silicon*, J.Appl.Phys., Vol.30, No.3, 427-431.

Katcki J. (1987), *A review of structural defect generation mechanisms in EFG ribbons*, J.Cryst.Growth, Vol.82, 197-202.

Kim J.K. and P.K.Rohatgi (1998), *The effect of the diffusion of solute between the particle and the interface on the particle pushing phenomena*, Acta mater., Vol.46, No.4, 1115-1123.

Kolbesen B.O. and A.Mühlbauer (1982), *Carbon in silicon: Properties and impact on devices*, Solid-State Electronics Vol.25, No.8, 759-775

Lawerenz A., M.Ghosh, K.Kremmer, V.Klemm, A.Müller and H.J.Möller (2004), *Infrared Transmission of rod-like defects in multicrystalline silicon*, Solid State Phenomena, Vols.95-96, 501-506

Lee L.G., P.D.Miller and I.B.Cutler (1977), in *Reactivity of Solids*, (8th ISRS), ed. by J.Wood, O.Lindqvist, C.Helgesson and N.G.Vannerberg, Plenum Press, 701-711

Lide D.R. (1991-1992), CRC Handbook of chemistry and physics, 72nd edition, CRC Press, Inc.

Melendez-Martinez J.J. and A.Dominguez-Rodriguez (2004), *Creep of silicon nitride*, Progress in Materials Science, Vol.49, Issue 1, 19-107.

Motzfeldt K. (1988), *Oxides plus carbon*, Proceedings of the Terkel Rosenqvist symposium, ed. by S.E.Olsen and J.K.Tuset, The Norwegian Technical University, Trondehim, 127-150.

Möller H.J. (2004), *Carbon-induced twinning in multicrystalline silicon*, Solid State Phenomena, Vols.95-96, 181-186.

Newman R.C. and R.S.Smith (1969), *Vibrational absorption of carbon and carbon-oxygen complexes in silicon*, J.Phys.Chem.Solids, Vol.30, 1493-1505

Nozaki T., Y.Yatsurugi and N.Akiyama (1970), *Concentration and behavior of carbon in semiconductor silicon*, J.Electrochem.Soc.:Solid state science,Vol.117, No.12, 1566-1568

Oden L.L. and R.A.McCune (1987), *Phase Equilibria in the Al-Si-C system*, Metallurgical Trans.A, Vol.18A, 2005-2014.

Olesinski R.W. and G.J.Abbaschian (1984), *The C-Si (carbon-silicon) system*, Bulletin of Alloy Phase Diagrams, Vol.5, No.5, 486-489.

Ottem L. (1993), *Løselighet og termodynamiske data for oksygen og karbon i flytende legeringer av silisium og ferrosilisium*, SINTEF Report, STF34 F93027

Pivac B., M.Amiotti, A.Borghesi, A.Sassella and J.Kalejs (1992), *Effect of annealing on carbon concentration in edge-defined film-fed grown polycrystalline silicon*, J.Appl.Phys., Vol.71, No.8, 3785-3787

Pivac B., A.Sassella and A.Borghesi (1996), *Non-doping light impurities in silicon for solar cells,* Materials Science and Engineering B36, 55-62

Rao C.V., H.E.Bates and K.V.Ravi (1976), *Electricial effects of SiC inclusions in EFG silicon ribbon solar cells*, J.Appl.Phys., Vol.47, No.6, 2614-

Riley F.L. (2000), *Silicon nitride and related materials*, J.Am.Cer.Soc., Vol.83, 245-288

Sasikumar R. and T.R.Ramamohan (1991), *Distortion of the temperature and solute concentration fields due to the presence of particles at the solidification front-effects on particle pushing*, Acta metall.mater., Vol.39, No.4, 517-522

Scace R.I. and G.A.Slack (1959), *Solubility of carbon in silicon and germanium*, The Journal of Chemical Physics, Vol.30, No.6, 1551-1555

Schätzle P., Th.Zöllner, R.Schindler and A.Eyer (1993), *Homogeneity analysis of multicrystalline silicon ingots with columnar grain structure*, IEEE, 78-82

Schmid F., C.P.Khattak, T.G.Digges and L.Kaufmann. (1979), *Origin of SiC Impurities in Silicon Crystals Grown from the Melt in Vacuum*, J.Electrochem.Soc.: Electrochemical Science and Technology, Vol.126, No.6, 935-938

Schönecker A., L.J.Geerligs and A.Müller (2004), *Casting technologies for solar silicon wafers :block casting and ribbon-growth-on substrate*, Solid State Phenomena, Vols.95-96, 149-158

Stefanescu D.M., A.Moitra, A.Kakar and B.K.Dhindaw (1990), *The influence of buoyant forces and volume fraction of particles on the particle pushing/entrapment transition during directional solidification of Al/SiC and Al/Graphite composites*, Metall.Trans., Vol.21A, 231

Tang K. (2003), *Thermochemical Database for MS-Si and SoG-Si Metals*, Sintef report STF24 F04509, Sintef Materials Technology

Uhlmann D.R. and B.Chalmers (1964), *Interaction between particles and a solid-liquid interface*, J.Appl.Phys., Vol.35, No.10, 2986-2993

Yanaba K., M.Akasaka, M.Takeushi, M.Watanabe, T.Narushima and Y.Iguchi (1997), *Solubility of carbon in liquid silicon equilibrated with silicon carbide*, Mat.Trans., JIM, Vol.38, No.11, 990-994

Yanaba K., Y.Matsumura, T.Narushima and Y.Iguchi (1998), *Effect of alloying elements on the carbon solubility in liquid silicon equilibrated with silicon carbide*, Mat.Trans., JIM, Vol.39, No.8, 819-823

Yatsurugi Y., N.Akiyama, Y.Endo and T.Nozaki. (1973), Concentration, *Solubility, and Equilibrium Distribution Coefficient of Nitrogen and Oxygen in Semiconductor Silicon*, J.Electrochem.Soc.: Solid-State Science and Technology, Vol.120, No.7, 975-979

Part I

Oxidative refining of carbon and boron from liquid silicon

Chapter 3 Part I: Oxidative refining of carbon and boron from liquid silicon

In this part the initial experiments, on the removal of dissolved carbon and boron from liquid silicon by use of an oxidative plasma treatment, are presented in the form of a paper that was presented at the 17th European Solar Energy Conference and Exhibition, Münich, 2001. These experiments were conducted in collaboration with SINTEF Materials and Chemistry. The oxidative carbon removal was the main focus of the study when starting the Ph.D-work, since boron can be removed by slag-treatment [Schei *et al.* 1998]. It was decided to end these experiments at an early stage, since the experimental set-up proved unsuitable for carbon removal. The two major defaults were the lack of a vacuum unit and the extended use of graphite. Unfortunately the costs and resources involved to reconstruct the experimental set-up would be too high.

The paper is followed by a discussion of the oxidative removal of carbon in 3•1, emphasizing some points that seem important in order to achieve a removal of carbon. Concluding remarks are given in section 3•2.

REMOVAL OF CARBON AND BORON FROM LIQUID SILICON BY THE USE OF A PLASMA ARC

Søiland A.K.[1], Tuset J.K.[1], Jensen R.[2], Prytz, S.[2] and Solheim I. [2]

1) Norwegian University of Science and Technology, Institute of Materials Technology and Electrochemistry, Alfred Getz v. 2b, 7491 Trondheim.
2) Sintef Materials Technology, Process Metallurgy, Alfred Getz v. 2b, 7465 Trondheim.

ABSTRACT: A plasma arc in combination with inductive heating has been used to study the removal of dissolved carbon and boron from liquid silicon. The non-transferred arc was run with equal quantities of H_2 and Ar, containing 2 vol% and 4 vol% O_2 in the flow. Temperatures employed were 1823 K and 1753 K. EG-Si was used with controlled amounts of C and B added before melting. A decreasing level of boron was measured; from 35 ppmw to 20 ppmw during 100 minutes of oxidative plasma treatment. The carbon level varied all along the experiments due to contamination from the atmosphere above the liquid surface. This was probably caused by a reaction between humidity contained in the furnace insulation and the graphite susceptor, producing CO gas. When the oxygen content was increased to 4 vol% an immediate formation of a silica film on the surface was observed.
Keywords: Si - 1: Carbon - 2: Multi-Crystalline - 3

1. INTRODUCTION

In the future years, the growing multicrystalline photovoltaic industry will be in the need for an alternative feedstock source, as the present one being rejects from the semiconductor industry, is limited and is not expected to increase [1,2] .

Great efforts have therefore been made to develop processes for production of a low-cost solar grade silicon (SoG-Si) especially designed as a future feedstock for the fast growing PV-industry. Recent examples of such are NEDO and ARTIST [3,4], but none has so far been considered as sufficently cost effective. The Norwegian Research program, "From Sand to Solar Cells", has recently been started. In this program an electrochemical process for production of SoG-Si is investigated [14], as well as the present study of plasma treatment combined with inductive heating for the removal of carbon and boron from liquid Si. These elements are always present at unacceptable levels in metallurgical grade silicon which is the original source for an upgraded quality (UMG-Si) as used in the mentioned examples. Both elements have a rather high segregational coefficient, k_0 (B): $8x10^{-1}$ and k_0 (C): $6x10^{-2}$ [13], and are therefore difficult to remove by directional solidification.

Several groups have studied plasma purification of UMG-Si before [4-10], with O_2 or H_2O as the reacting specie, but only the latest one in combination with inductive heating [4,5].

In the present study the starting material is however not UMG-Si, but EG-Si contaminated with controlled quantities of carbon and boron, and it is a large scale

experiment (24 kg). The plasma treatment gives the possiblity of a locally high temperature on the liquid surface, which is favorable for the reactions, without heating too much the silica crucible that cannot withstand higher temperatures than 1873-1973 K. The inductive heating provides stirring of the melt which facilitates the diffusion of elements.

2. EXPERIMENTAL

2.1 Experimental Set Up (figure 1)

An inductive furnace of 200 kW power and a frequency of 2000 Hz, was used for melting and keeping the temperature stable. The silicon was loaded in an amorphous silica crucible (type used for Czochralski pulling) with an inner diameter of 29 cm, and height of 22 cm. Since Si at room temperature is not a conductor the crucible was surrounded by a graphite susceptor. The furnace was covered with a watercooled lid in stainless steel. The lid contained 5 ports, 1) observation port, 2) lock port for adding silicon when melting has started, 3) port for measuring temperature and taking melt samples, 4) port for gas outlet, and 5) port for the plasma torch. The underside of the lid was insulated with alumina castable. Alumina fibre insulation was used between the graphite susceptor and the induction coil. A Plasma Systems plasma torch with a pencil shaped 2% thoriated tungsten cathode and a copper anode/nozzle was used. It was run at power 25 kW in a non-transferred arc mode at a distance of approximately 5 cm above the bath surface.

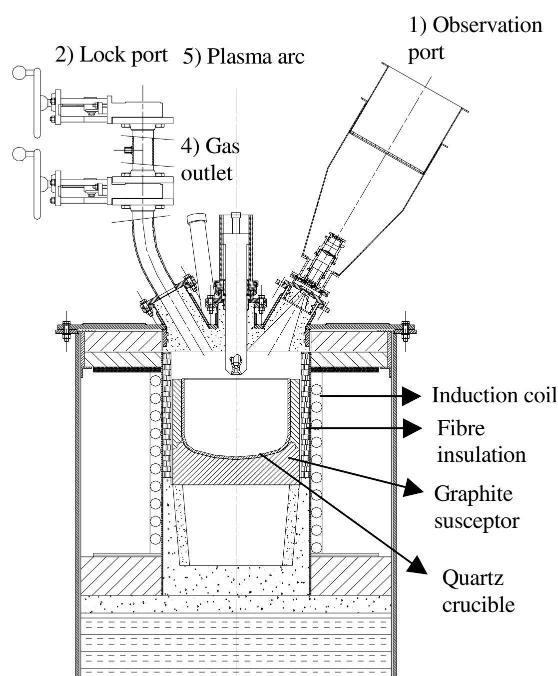

Figure 1: Experimental Set Up; furnace and lid.

2.2 Experimental Procedure

A quantity of 24 kg of silicon was charged in the crucible along with a master alloy containing boron (35-40 ppmw). In the first experiment carbon was introduced as carbon tablets once the silicon had melted, while in the second experiment it was loaded as SiC (58 ppmw) along with silicon and the master alloy of boron. Inductive heating was used for the melting of the charge. During heating the system was flushed with 50 Nl/min Ar through the plasma torch, 10 Nl/min Ar through the observation port and 10 Nl/min through the lock port. The gas furnished came from AGA AS (purity 99.99%).

The plasma arc was started once the charge had melted, and run with Ar (25 Nl/min first exp., and 50 Nl/min second exp.) for 10-20 min. Then H_2 (AGA AS, purity 99.60%) was introduced in the torch with the same flow as Ar. After a while the oxygen (AGA AS, purity 99.95%) was introduced first with 2 vol% in the flow, and at a later stage 4 vol%. Temperatures were registered at four different positions; in the top of the graphite susceptor, in the bottom of the graphite susceptor, in the bath and in the gas outlet. The effect of purification was measured by regularly taking melt samples, approximately from the vertical middle of the melt, by suction with a silica tube. These samples were analyzed at Elkem Research Center. ICP was the technic used for boron detection, while the carbon content was measured by LECO-analysis.

3. RESULTS

In the first experiment the temperature was set at 1823 K, a maximum temperature of 1819 K was registered in the bath after the plasma torch was introduced. This temperature proved to be too high for the silica crucible that cracked due to a volume increase, caused by crystallization of the crucible. This happened approximately 10 minutes after the oxygen was introduced in the plasma torch. Figure 2 shows the evolution in the carbon and boron contents during this experiment. The carbon content varies a lot during the experiment and is much higher than anticipated from the quantities added to the melt, indicating carbon pickup from the surroundings. For boron, the content decreases after introduction of oxygen in the plasma gas, from 40 ppmw to 15 ppmw. The results from this experiment should however be interpreted with precaution, because of the cracking of the crucible, resulting in a subsequent downfall of the melt level and direct contact between the melt and the susceptor.

Due to the cracking of the crucible, the temperature was set at 1753 K in the second experiment. A maximum temperature of 1761 K was registered in the bath. Also this experiment started out with 2 vol% O_2 in the plasma gas, but when the oxygen content was increased to 4 vol%, the formation of a silica layer on the bath surface started. The silica crucible preserved its original amorphous structure, and only cracks due to solidification was observed after the experiment. Figure 3 shows the carbon and boron contents during this experiment. Also here a higher level of carbon is measured than expected from the quantities charged. A decreasing boron level, from 35 ppmw to 20 ppmw, is observed during 100 minutes of oxidative plasma treatment.

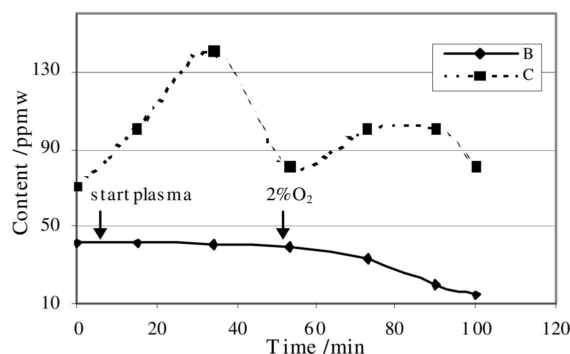

Figure 2: Boron and Carbon contents in a Si-melt during plasma treatment with oxygen and hydrogen, T=1820 K, exp.1.

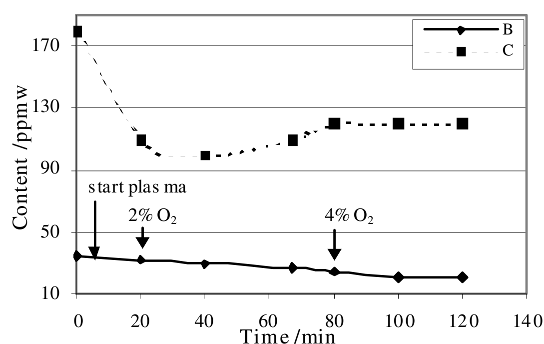

Figure 3: Boron and Carbon contents in a Si-melt during plasma treatment with oxygen and hydrogen, T= 1750 K exp.2.

4. DISCUSSION

Several suboxides of boron can form during a plasma treatment with gas containing H_2O and H_2. Preliminary equilibrium calculations were carried out using a commercially available program for thermodynamic calculations, FactSage 5.0. Thermodynamic data for boron in liquid silicon was taken from Noguchi et al. [12]. In our calculations HBO was found as the major specie formed, with minor quantities (50 times smaller at 1800 K) of HBO_2, BO and BH_2. Increasing temperature favours the formation of these suboxides of boron. Also manuel calculations of the simultaneous equilibria predicted HBO as the far most important specie formed. Alemany et al. [5] found as well HBO to be the major

specie formed in their thermodynamic study using another program. However, the calculated value for the mole fraction of HBO in the gas phase is as low as $9.5x10^{-7}$ at 1800 K. Consequently when these data are used in calculating the amount of boron being removed over a 100 minutes treatment time there will be no significant change in contrast to the results obtained. This indicates that the thermodynamic data are erroneous or that these vaporization reactions are enhanced in some way for kinetic reasons.

Under an oxidative plasma treatment carbon is removed as CO by the reaction;

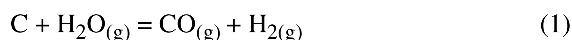

$$C + H_2O_{(g)} = CO_{(g)} + H_{2(g)} \quad (1)$$

In our experiments it has unfortunately not been possible to control the carbon content in the melt, which has shown great variations and higher levels than the added amount. This means that the liquid bath has been contaminated with carbon from the surroundings. The carbon source is most probably the graphite susceptor. In contact with an oxygen containing gas the graphite reacts to CO. In a quantitative model for carbon incorporation in Czochralski Si-melts, the carbon monoxide evolved stemmed from a reaction between the silica crucible and the graphite susceptor, because of the direct contact between these [11].

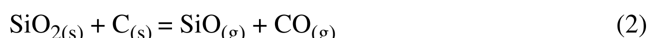

$$SiO_{2(s)} + C_{(s)} = SiO_{(g)} + CO_{(g)} \quad (2)$$

The rate limiting step is supposed to be the CO-transport from the graphite to the melt, this transport is controlled by the flow conditions in the furnace. In the present experiments the gas flows have been turbulent because the gas from the plasma torch has a tangential movement, and the flow rate is high, thus giving flow conditions that can transport CO to the melt. However, we find it more plausible that CO primarily comes from a reaction between humidity evolved from the furnace insulation and the graphite susceptor, since the chamber had no evacuation possiblity. The quantities of carbon incorporated in the melt are so high that it seems less possible that the reaction between the silica crucible and the graphite susceptor is the dominant source.

When increasing the oxygen content to 4% O_2 (8 vol% H_2O) in the gas flow, the formation of a silica film on the surface was clearly seen. At first it was dispersed and the bath just below the arc remained open, but after a while the surface was completely covered. This layer inhibit further reactions on the surface, as the last melt measurements in figure 3 indicate. Since the carbon content does not increase after the silica formation, the view that the carbon contamination stems from the gas atmosphere over the bath seems fairly reasonable. Earlier works on plasma refining have also observed the formation of such a silica layer [3,4]. This was reported to occur at 7.2 vol% H_2O in the gas flow by Baba et al. [3], which is quite close to the conditions used in experiment 2, but where a lower temperature was used than by Baba *et al.*

5. CONCLUSION

During the plasma treatment with 2 vol% and 4 vol% O_2 in the Ar/H_2-flow a significant boron removal has been measured. At 4 vol% O_2 the formation of a silica film which inhibited further reactions was observed. In these experiments the silicon melt was contaminated by carbon from the surroundings. This was probably due to a CO production caused by humidity in the furnace insulation reacting with the graphite susceptor. With the equipment available at the moment this problem is difficult to solve.

REFERENCES

[1] D.Sarti and R.Einhaus, E-MRS 2001 Spring Meeting, Strasbourg, France , Paper reference: E6.2
[2] P.Woditsch and W.Koch, E-MRS 2001 Spring Meeting, Strasbourg, France, Paper reference: E 1.2
[3] H.Baba, K.Hanazawa, N.Yuge, Y.Sakaguchi, H.Terashima and F.Aratani, 13th European Photovoltaic Solar Energy Conference, Nice, France, 1995, 390-394
[4] S. De Wolf, J.Szlufcik, Y. Delannoy, I.Périchaud, C.Hãßler, R.Einhaus, , E-MRS 2001 Spring Meeting, Strasbourg, France ,Paper reference: E-I.4
[5] C.Alemany, C.Trassy, B.Pateyron, K-I. Li, Y.Delannoy, E-MRS 2001 Spring Meeting, Strasbourg, France , Paper reference: E I.3.
[6] J.Amouroux and D.Morvan, High Temp.Chem.Processes 1 (1992), 537-560.
[7] R.Combes, D.Morvan, G.Picard and J.Amouroux,
J.Phys.III France 3 (1993), 921-943
[8] J.Erin, D.Morvan and J.Amouroux, J.Phys.III France 3 (1993), 633-652
[9] T.Ikeda and M.Maeda, ISIJ International, Vol. 32 (1992), No. 5, 635-642
[10] N.Yuge, M.Abe, K.Hanazawa, H.Baba, N.Nakamura, Y.Kabo, Y.Sakaguchi, S.Hiwasa and F.Aratani, Progress in Photovoltaics: research and appl. (2001) : 9: 203-209.
[11] T.Carlberg, J.Electrochem.Soc.: Solid-state Science and Technology, Vol.130, No.1 (1983), 168-171
[12] R.Noguchi, K.Suzuki, F.Tsukihaski and N.Sano, Metallurgical and Materials Transactions B, Vol. 25B (1994), 903-907.
[13] W.Dietze, W.Keller, A.Mühlbauer, J.Dietl, D.Helmreich, E.Sirtl, T.F.Ciszek and F.V.Wald, Crystals Growth, Properties, and Applications 5 (1981), Springer-Verlag.
[14] E.Olsen and G.Hagen, presented in this conference; 17th European Photovoltaic solar energy conference and exhibition, REF; OC6.2

3•1 Oxidative refining of silicon with respect to carbon

For silicon supersaturated with carbon, there will be both silicon carbide particles and dissolved carbon present. Previous studies have shown that silicon carbide may be removed by filtration [f.inst. Sakaguchi and Maeda, 1992, and Klevan, 1997].

For the removal of dissolved carbon oxidative gas treatment can be considered. The removal of carbon may be described by the following reaction:

$$\underline{C} + 1/2O_{2(g)} = CO_{(g)} \qquad 3•1$$

There is, however, a parallel reaction occurring:

$$Si(l) + 1/2O_{2(g)} = SiO_{(g)} \qquad 3•2$$

This reaction gives a continous loss of silicon, and SiO condensates at the colder parts in the furnace as a mixture of Si and SiO_2.

If the oxygen pressure is above a certain limit an oxidic film may form on the melt surface. This was observed in the second plasma experiments (Paper I). It was seen in this experiment that there was no change in carbon nor boron content after the formation of this layer. The formation of the silica layer inhibited further reaction. The formation of this layer was in our case observed already at 4 vol% O_2 in the gas stream.

<u>Decarburization:</u>

If the silicon melt is contained in a silica crucible, which is often the case, the decarburization reaction is written as:

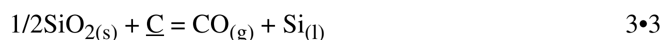

$$1/2SiO_{2(s)} + \underline{C} = CO_{(g)} + Si_{(l)} \qquad 3•3$$

$$K_{3\cdot 3} = \frac{p_{CO} \times a_{Si}}{\sqrt{a_{SiO2}} \times a_c} \qquad \text{eq•3•1}$$

where $K_{3.3}$ is the equilibrium constant for reaction 3•3, p_{CO} is the partial pressure of CO, a_{Si} the activity of silicon, a_{SiO2} the activitiy of SiO_2 and a_C the activity of carbon.

The following expression for X_C is obtained when a_{Si} and a_{SiO2} are equal to one:

$$X_C = \frac{p_{CO}}{\gamma_C \times K_{3\cdot3}} \qquad \text{eq•3•2}$$

where γ_C is the activity coefficient for carbon. The calculated values for $K_{3\cdot3}$ and γ_C at different temperatures are given in Table 3•1. Thermochemical data are taken from JANAF Thermochemical Tables [Chase *et al.*, 1985]. The relation for γ_C estimated by Ottem [1992] from his solubility experiments has been employed and is given below, it applies to concentrations of carbon close to the solubility limit [Ottem, 1992].

$$\gamma_C^{Si-C-O} = \exp\left(0.086 + \frac{7672}{T}\right) \qquad \text{eq•3•3}$$

From Table 3•1 it is seen that $K_{3\cdot3}$ increases with increasing temperature, while γ_C decreases. The product $K_{3\cdot3}$ and γ_C increases, however, with increasing temperature. This means that the decarburization of dissolved carbon is favoured by high temperatures and low CO partial pressure.

Table 3•1: Thermochemical values for reaction 3·3 and the activity coefficient at different temperatures.

Temperature / K	1700	1800	1900	2000	2100
$\Delta G^0_{3\cdot3}$ / J mol^{-1}	44317	25947	7644.5	-10593	-28769
$K_{3\cdot3}$	0.04	0.18	0.62	1.89	5.2
γ_C	99	77	62	51	42
$K_{3\cdot3}$*γ_C	4.3	13.7	38.1	95.5	218.6

When the decarburization takes place in a silica crucible the SiO-pressure is given by the following reaction:

$$SiO_{2(s)} + Si_{(l)} = 2SiO_{(g)} \qquad 3•4$$

$$p_{SiO} = \sqrt{K_{3\cdot4}} \qquad eq•3•4$$

Since there will always be a loss of silicon to evaporation of SiO, it is interesting to look at the ratio p_{CO}/p_{SiO} for the decarburization as a function of temperature. This ratio should be as high as possible. We have calculated p_{CO} from reaction 3•3 at different temperatures for a melt containing 40 ppm mass (95 ppma) of carbon. The SiO pressure was calculated from eq·3·4 employing thermochemical data from JANAF Thermochemical Tables [Chase *et al.*, 1985]. The partial pressure of CO and the p_{CO}/p_{SiO} ratio as a function of temperature are shown in Figure 3•1. It is seen that a temperature increase enhance the decarburization, but has the drawback of increasing the silicon loss.

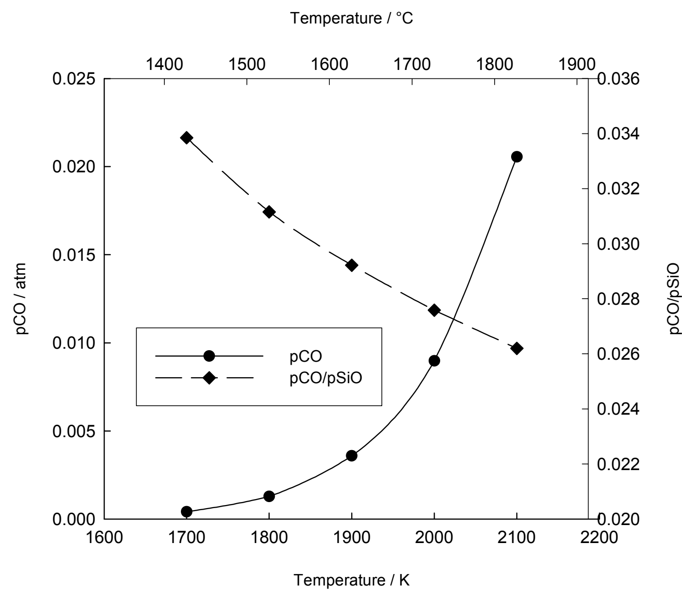

Figure 3•1: Equilibrium CO-pressure for reaction 3·4 and p_{CO}/p_{SiO} ratio as a function of temperature. Calculated from eq 3·3 for a melt containing 40 ppm mass of carbon.

Importance of CO-pressure:

When discussing the decarburization, the work of Endo *et al.* [1979] should also be considered, see section 2·4·2. They measured the pressure of CO in equilibrium with a silicon melt saturated with carbon and oxygen. The equilibrium CO pressure at the melting point was found to be $3.8x10^{-4}$ atm. For the removal of carbon it is, as seen also from Figure 3•1, important/vital to keep the CO -pressure at the melt surface below the equilibrium CO-pressure to prevent back-reaction. That is to prevent an incorporation of carbon to the melt instead of a removal. It is also seen from eq 2·7 that the carbon concentration is inversely proportional to the oxygen concentration. Thus a high oxygen concentration will yield a lower carbon concentration.

To ensure a low pressure of CO at the surface must not only CO contamination from the surroundings be eliminated, but CO from decarburization reaction itself must be efficiently removed from the surface. Therefore should the resistance for mass transport in the gas boundary layer be kept at a minimum. Harris and Davenport [1982] derived an operational vacuum distillation criterion which ensures little resistance to mass transport in the gas phase. The criterion is: chamber pressure must be less than the total melt vapour pressure;

$$P_{ch} < \sum_{i=1}^{Z} P_{i,s} \qquad \text{eq•3•5}$$

In our case SiO and CO are considered as the melt vapour species. Since p_{SiO} is much higher than p_{CO} it will decide the most favourable chamber pressure according to this criterion. The p_{SiO} pressure at for instance 1800 K (1527 °C) is 0.04 atm. Thus, if the chamber pressure is kept below this value the resistance to mass transport in the gas phase should be at a minimum according to this criterion. The pressure of SiO increases with increasing temperature, thus allowing higher chamber pressure.

However, it will still be necessary to ensure a low CO pressure at the surface to prevent back-reaction. This can be obtained by combining gas purging with reduced pressure.

Graphite-free environment:

If decarburization is conducted in a furnace containing graphite parts (f.inst. heaters, support plates), there will be various side-reactions taking place which produce CO, see section 2·4·1. These reactions will increase the CO-pressure in the furnace chamber and make it more difficult to attain a sufficiently low CO pressure at the surface. Air leakage should of course also be avoided, since oxygen will react immediately with the graphite producing CO. A graphite-free environment would thus be a clear advantage for the decarburization.

Summary:

In order to achieve carbon removal by oxidative treatment some points seem necessary; graphite parts should be avoided, a low chamber pressure combined with gas purging of the surface, and a high oxygen content. These points are consistent with the experimental results from Sakaguchi and Maeda [1992] who reduced the carbon content form 50 ppm mass to 10 ppm mass by oxidative refining. They used a silica crucible (~60 mm height, diameter 40 mm), no graphite parts, low chamber pressure ($<10^{-3}$ atm), gas purging of the surface and silica addition to the surface to ensure a high oxygen content at the surface.

Increasing the temperature should be an advantage for the decarburization, although the silicon loss will be higher. Employing a plasma treatment provides a high surface temperature. In the study of Amouroux *et al.* [1992] a combination of plasma/slag resulted in a carbon content as low as 0.04 ppm mass, this was in a laboratory scale equipment. However, larger scale studies involving only plasma have not given clearly positive results for the decarburization [f.inst. Fourmond *et al.*, 2004 and Yuge *et al.*, 2001]. An explanation could be that it is difficult to ensure a low enough CO-pressure at the surface in larger units.

3•2 Concluding remarks

The oxidative removal of carbon and boron was attempted by use of a plasma arc. Significant boron removal was measured, but for carbon CO contamination in the furnace made it impossible to study the decarburization. To remove carbon by oxidative treatment is difficult since the equilibrium CO pressure is very low, and one must avoid the formation of an oxidic layer on the surface. Therefore the oxygen content must be controlled. To avoid back- reaction it is important to have a system operated under vacuum and purging the surface to efficiently remove evolved CO. In such a system it would also be an advantage to avoid graphite components that by various reactions produce additional CO.

An alternative to the oxidative removal of carbon, could be the use of directional solidification. If the silicon carbides precipitated during solidification are pushed by the interface, the majority of particles can be captured in the last part to solidify. The bulk material will then have a purity with respect to carbon that is close to the solid solubility limit, or somewhat higher depending on the quantity of particles that are engulfed during solidification.

REFERENCES

Amouroux J. and D.Morvan (1992), *Heat and mass transfer phenomena during plasma/ slag interactions. Applications on the production of ultrapur material.*, High Temp.Chem.Processes, Vol.1, 537-560

Chase M.W. Jr., C.A.Davies, J.R.Downey Jr., D.J.Frurip, R.A.McDonald and A.N.Syverud (1985), *JANAF Thermochemical Tables*, Third Edition, Part 1 and 2.

Endo Y., Y.Yatsurugi, Y.Terai and T.Nozaki (1979), *Equilibrium of Carbon and Oxygen in Silicon with Carbon Monoxide in Ambient Atmosphere*, J.Electrochem.Soc.: Solid-State Science and Technology, Vol.126 No.8, 1422-1425

Fourmond E., C.Ndzogha, D.Pelletier, Y.Delannoy, C.Trassy, Y.Caratini, Y.Baluais, R.Einhaus, S.Martinuzzi and I.Perichaud (2004), *Refining of metallurgical silicon for crystalline solar cells*, 19th European Photovoltaic Solar Energy Conference and Exhibition, in press

Harris R. and W.G.Davenport (1982), *Vacuum Distillation of Liquid Metals: Part I. Theory and Experimental Study*, Metallurgical Transactions B, Vol.13B, 581-583

Klevan S. (1997), *Removal of C and SiC from Si and FeSi during ladle refining and solidification*, PhD-thesis 1997:11, Institute of Materials Technology, Norwegian Technical University (NTNU)

Ottem L. (1993), *Løselighet og termodynamiske data for oksygen og karbon i flytende legeringer av silisium og ferrosilisium*, SINTEF Report, STF34 F93027

Sakaguchi K. and M.Maeda (1992), *Decarburization of silicon melt for solar cells by filtration and oxidation*, Metallurgical Transactions B, Vol. 23B, 423-427

Schei A., J.K.Tuset and H.Tveit (1998), *Production of high silicon alloys*, Tapir Forlag, Norwegian Technical University (NTNU)

Yuge N., M. Abe, K.Hanazawa, H.Baba, N.Nakamura, Y.Kato, Y.Sakaguchi, S.Hiwasa and F.Aratani (2001), *Purification of Metallurgical-grade Silicon up to Solar Grade*, Progress in Photovoltaics Research and Applications, 9, 203-209

Part II

Si_3N_4- and SiC inclusion formation in industrially produced multi-crystalline silicon

Chapter 4 Experimental

Parts of the experimental work was carried out at ScanWafer ASA's plant in Glomfjord, this is the melt sampling experiments. The characterisation work on selected parts of the ingot was carried out at the university. In the following section a short introductory description of the furnace is given. This is followed by a description of the melt sampling unit, procedure and analyses. Description of the subsequent solid phase characterisation is given. The latter consisted of measurements of carbon content in the wafers and a study of the larger inclusions present in the material (top-cuts and selected wafers).

4•1 Furnace

The furnace design is new, details and industrial drawings of the furnace will not be presented for confidentiality reasons, but a simple principle schetch showing the approximate melt sampling position is given in Figure 4•1. The furnace principle is closest to the Heat Exchanger Method (HEM), since heat is extracted from the bottom, and the crucible is in a static position. The furnace takes four crucibles at a time. Graphite supporter plates surround each crucible and keep it together after cracking during cooling down. The furnace is covered with a watercooled lid of stainless steel which is sealed to the furnace. Figure 4•2 shows the different crucible positions in the furnace.

During these experiments the temperature is measured at crucible position one, and in the graphite insulation plate just below the crucibles, between crucible position three and four. In crucible position one the temperature is measured with a two-colour pyrometer, while in the graphite insulation plate temperature is measured by a thermocouple. We had no possibility of measuring the temperature directly in the melt by use of a thermocouple in these experiments. In order to have an indication of the sampling temperature we therefore used the pyrometer readings from crucible position one. These

are not precise temperature measurements since they are pyrometer readings AND because they are measured in crucible position one which is not the melt sampling position (crucible position three). In addition the pyrometer reading measure the surface temperature, whereas we retrieve the melt samples at a position ~ 50 mm beneath the melt surface (this is approximately 1/5 of the total bath height at $f_s = 0$). A problem with the pyrometer readings is that the silicon melt surface act as a mirror, and therefore may reflections from the furnace chamber disturb the measurements. The standard deviation for the pyrometer readings in Glomfjord has been estimated to ±15 °C [Personal communications, Erik Sauar at REC].

A rough description of the standard program is given in Table 4•1. The process is normally run at a pressure below 1 bar, and under Ar-flow. Of confidentiality reasons more details cannot be given.

.

Table 4•1: Program steps in the furnace

Step no.	Procedure	Remarks
1	Melt-down	visual verification
2	Holding period	
3	Crystallisation	
4	Cooling	

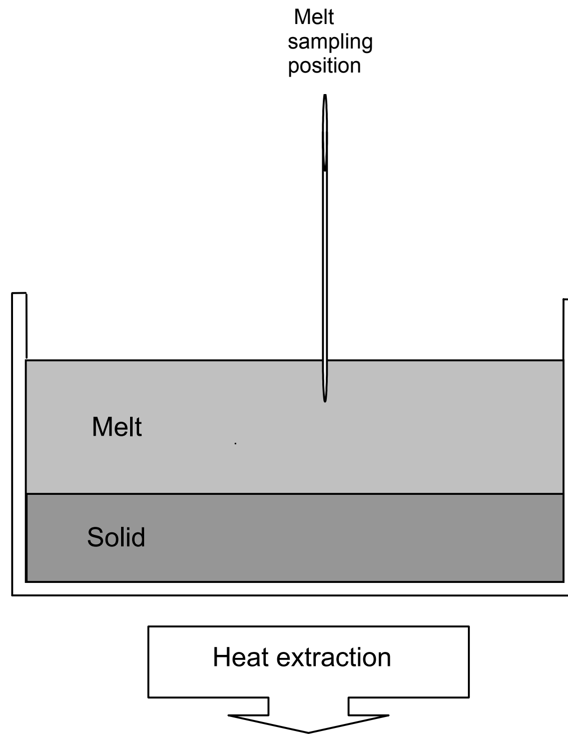

Figure 4•1: Principle sketch of furnace, showing one crucible and the melt sampling position. Heating zones are not shown for confidentiality reasons.

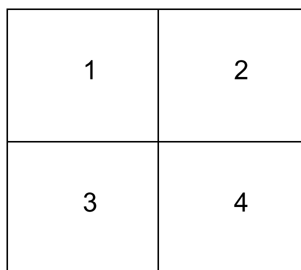

Figure 4•2: Crucible positions in the furnace

4•2 Crucible and coating

The crucibles employed are fused silica crucibles (690x690mm^2). The typical purity of these crucibles is > 99.6%, the main impurities are Al_2O_3, Fe_2O_3 and TiO_2. The crucibles are loaded in a clean room with a charge consisting of recycled material, “tops and tails” and “chips and chunks”, as described in Table 1·1.

The coating is of silicon nitride and is synthesized from silicon tetra-chloride and ammonia by the liquid interfacial reaction method. This gives a product of > 95% α-phase silicon nitride and the residual part is the β-phase silicon nitride. X-ray analysis verified that the coating mainly consists of the α-phase, see Appendix 2. The specific surface area is 4~6 m^2/g The purity of the coating particles as given by UBE Advanced Ceramics is listed in Table 4•2. A slurry containing coating particles, organic solvent, deionized water and a wetting agent is sprayed on to the crucible surface, and is then heated at a high temperature for a couple of hours. Figure 4•3 shows an image of the coating particles

Table 4•2: Purity of coating particles (data sheet from UBE Advanced Ceramics)

Element	Content in coating
O	< 2%
C	< 0.2%
Cl	< 100 ppm mass
Fe	< 100 ppm mass
Al, Ca	trace

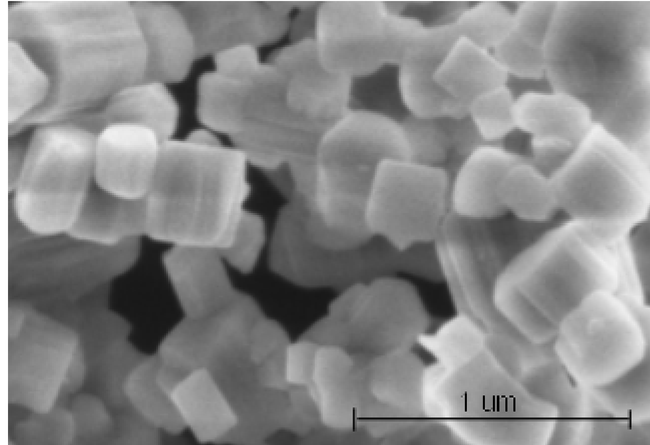

Figure 4•3: SEM-image of the coating particles (loose powder before mixing the slurry)

4•3 Sampling of the melt

4•3•1 Sampling unit for molten metal

A special sampling unit needed to be constructed for the melt sampling experiments. The planning and construction of the sampling unit was done at the university. A drawing of this unit is given in Figure 4•4. It is constructed in stainless steel with a cooling zone of ~50 mm at the top, and the lower part consists of a ball valve. The cooling zone could not be longer for practical reasons; there is a limitation in the length of the sampling unit since the tubes employed had a maximum length of 1 m. At the top part there is also a connection to a vacuum unit, so that the gas inside the quartz tube and sampling unit can be evacuated prior to sampling. Cooling in these experiments was by air flushing through the cooling channel. The cooling had actually two purposes; to cool the sample, but also to cool the o-sealing placed between the sampling tube and the adapter.

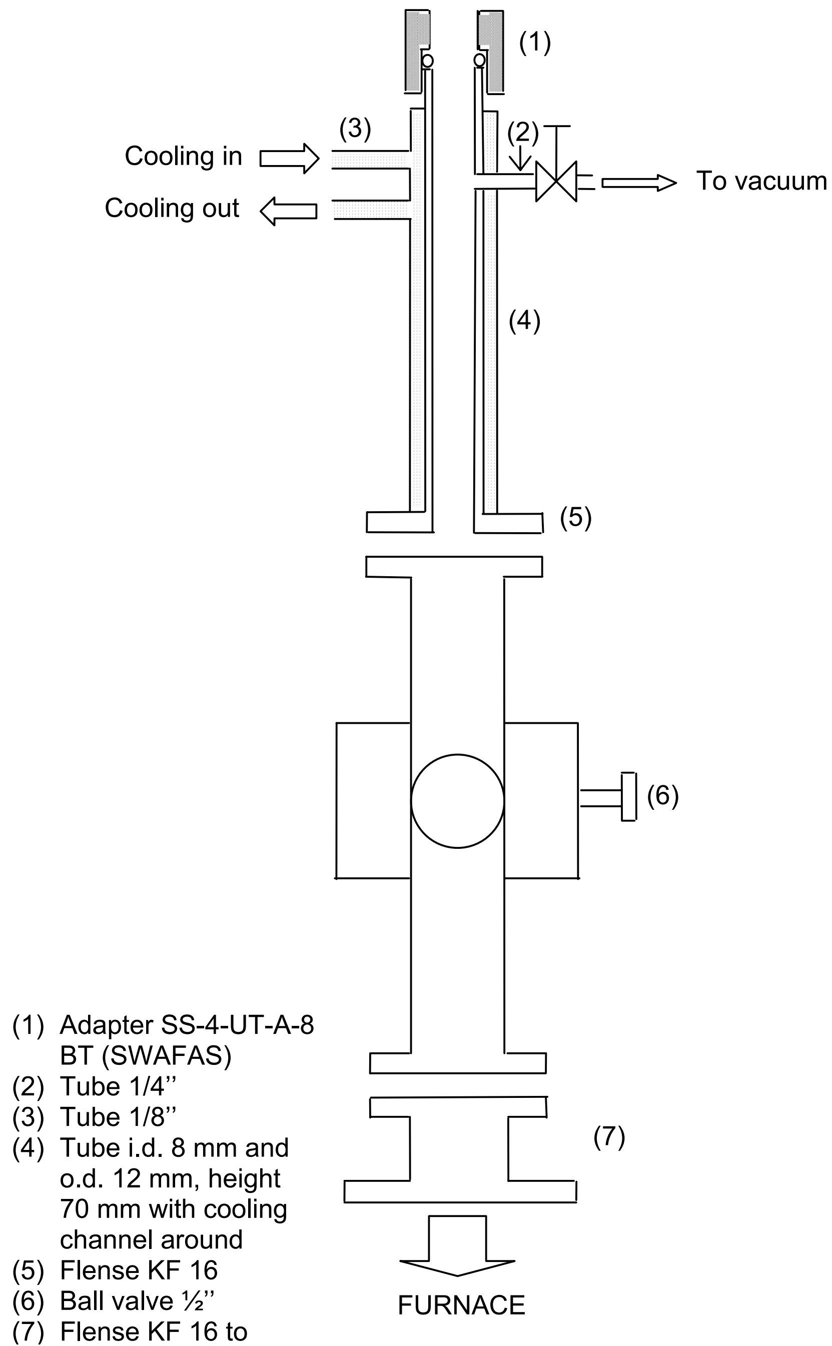

Figure 4•4: Cross-sectional drawing of the melt-sampling unit.

4•3•2 Sampling procedure

For these experiments the sampling unit was mounted at crucible position three in the furnace, where it was attached to the melt sampling entrance (see Figure 4•1). For sampling of the melt, quartz tubes of inner diameter 4 mm and outer diameter 6 mm (length 1 m) were used. Quartz tubes were chosen to minimize the contamination from other elements. The tubes had as thin walls as practically possible to ensure a fast cooling of the sample. Before opening the valve to the furnace the quartz tube is installed in the sampling unit and the whole assembly is evacuated, to prevent air contamination in the furnace chamber. Some seconds after this the valve is opened and the tube inserted into the melt (~50 mm below the melt surface). This position will be slightly deeper into the bath when solid is formed due to the smaller density of solid silicon. At high fraction solidified, the sampling position was adjusted to ensure a distance of 20 mm to the interface (solidification front). The melt sample is sucked into the tube with a syringe, and immediately after the tube is rapidly withdrawn from the melt. The part of the tube containing the melt sample is kept in the cooled area of the sample holder and the valve is closed.

Since the furnace is operated at a lower pressure (< 1 bar) sampling was not straightforward. Also the long distance the tube had to pushed before attaining the actual sampling position made the sampling delicate. Two persons were necessary both for security and practical reasons when sampling. One person controlled the quartz tube, pushed it in and out of the melt, while the other controlled the valve and the syringe. The solidification rate in the tube is estimated to be roughly ~ 1000 μm/s. Large deviations from this rate may occur depending on how fast the tube is pulled out from the melt. Sometimes depositions of SiO-gas on the tube made it difficult to pull the tube rapidly through the narrow upper part of the sampling unit.

4•3•3 Samples for analysis

Generally the samples were easily removed from the quartz, showing that little interaction between the quartz and the molten silicon took place. The quantity retrieved from the melt, however, varied from 10-20 mm up to 100-150 mm. This is because it was difficult to suck out the sample due to the reduced pressure in the furnace chamber. For the analysis the

middle 10-20 mm of the sample was used. Since the samples are solidified towards the center, the distribution of carbon over the cross section will not be uniform due to segregation. The degree of inhomogeneity is dependent on the concentration of carbon and how effective the quenching was.

The error of the LECO-analysis for carbon is described in section 4•3•4, but both the sampling and preparation of the samples will affect the total error of the measurements. This error is not known, but seems to be dependant on both parametres. That is how "good" (rapid) the sampling was, giving a more homogeneous sample, and on how the samples were prepared. It appeared to be an advantage to prepare the samples as neat sylinders, as discussed in 6·1·3. This technique was used on most samples (a part from MS-Exp 1) when the sample size was sufficiently large.

4•3•4 Analyzing technique for the melt samples

For the carbon analyses of the melt samples combustion IR-absorption was chosen as analyzing technique. The analyses were conducted by ELKEM Research in Kristiansand, which uses a LECO CS-444 apparatus for carbon and sulphur measurements. ELKEM Research has long experience in analysing for carbon in silicon, they also have experience in analysing quite low values of carbon in high purity silicon, and were therefore chosen as laboratory for these analyses.

The principle of the method is to heat (burn) the material in an O_2 atmosphere, the carbon in the material reacts to CO_2, which is transported by the oxygen to an IR-compartment where the CO_2 absorption is detected. Relating this absorption to calibration curves of samples with known C-content, the carbon content of the sample is obtained. For each sample three parallels are measured, the weight of each parallel is around 0.2 g. Previous work has shown that crushing of such samples is not recommended, since the samples often are inhomogeneous over the cross section [Ottem, 97]. This is due to segregation of carbon during cooling. Therefore the analysed parts were lumps or sylinders of the maximum size, that is 0.2 g. The calibration of the instrument is conducted on steel samples of known carbon content, the 0-point calibration is performed on copper and iron. These elements are normally added to each sample to act as an accelerator in the induction furnace. The error in the measurements is 6% + 1.5 ppm mass. Where 6% is the error in

the calibration curve and 1.5 ppm mass is the error of the blank. A higher standard deviation than the error will then indicate the inhomogeneity of the sample [Personal communication Eivind Bergland, ELKEM Research]. Thus, quenching of the sample is important to avoid/minimize segregation. The samples are boiled in hydrochloric acid prior to the analyses.

Other methods that were considered were Glow Discharge Mass Spectrometre (GDMS) and Secondary Ion Mass Spectrometre (SIMS). Both these methods are very expensive, and GDMS has a low reliability for carbon measurements below 100 ppm mass. SIMS was tried as method on three samples (see Appendix 3), but the method has a too narrow analysing area, and proved unsuitable on these samples due to the inhomogeneity in the samples.

Some of the samples were also analyzed for oxygen- and nitrogen- contents. These analyses were performed by Shiva Technologies Europe. The technique employed was also an inert gas fusion method, LECO analyzer TC436. The principle is the same as for the carbon analyses, but the gas is detected either by IR-absorption or by a thermal conductivity detector. The samples were cut with a diamond saw and the surface layer was etched away prior to the analyses. Usually, three parallells of 0.2 g were run for each sample. More parallells were run if the results were not reproducible. The accuracy of the method is estimated to 20-30% at these low levels of concentration [Personal communications Nicole Cuq at Shiva Technologies].

4•3•5 Contamination sources

In these experiments the most important contamination source is considered to be the sampling tube itself. The analyses that would be the most influenced by the silica sampling tube are the oxygen analyses. These measuremtents (see section 6·1·6) are low and in reasonable agreement with FTIR-measurements of ingots from the same type of furnace (see rr-test, chapter 5). In addition the samples were easily removed from the sampling tube, so the interaction between the melt and the tube must have been low.

The carbon content in these tubes has been measured to 26 ppm mass (±2.6) by combustion IR-absorption. When considering a sample size of 0.2 g, an amount of 8 mg of the quartz tube must dissolve to give a contribution of 1 ppm mass to the analysis. It

seems thus unlikely that there would be a significant contribution from the quartz tube in these experiments, which also indicated by the low oxygen analysis.

4•3•6 Fraction solidified and growth rate

The fraction solidified and growth rate was measured by dipping a solid quartz rod of 10 mm in diameter and 150 mm length into the melt, as illustrated in Figure 4•5.

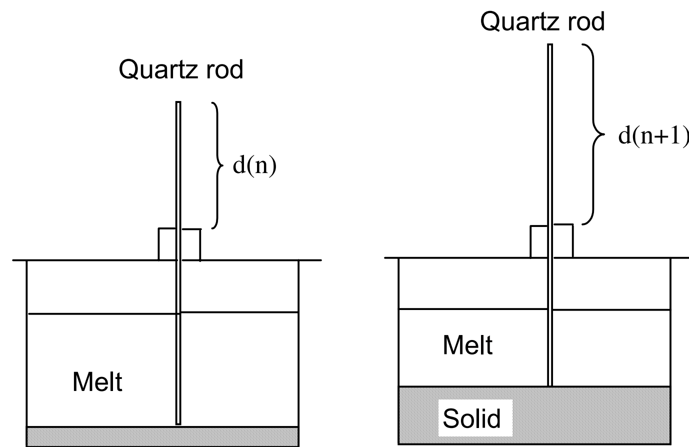

Figure 4•5: Sketch of quartz rod dipping of fraction solidified and the local growth rate.

where d(n) is measured distance of the quartz rod that is above the entrance channel at sampling (n).

The fraction solidified is then:

$$f_s = \frac{d(n+1) - d(0)}{\text{total block height}} \qquad \text{eq•4•1}$$

The local growth rate is then:

$$v = \frac{d(n+1) - d(n)}{\text{time elapsed between (n+1) and (n)}} \qquad \text{eq•4•2}$$

The distances is measured manually by use of a meter. These measurements give only rough estimates of f_s and v. Especially the local growth rate is not a reliable measure due

to various experimental factors. Depositions of SiO gas on the quartz rod tip may occur, resulting thus in a longer rod. Changes in the shape of the interface will also have an effect on these measurements. The measurements should, however, be more reliable for f_s because the distances measured here will be longer, since it measures the total growth from the start of crystallisation and not only the difference in growth between two subsequent samplings.

4•4 Convection in the melt

The combination of gravity and temperature distribution produces natural convection in the crucible. Davis and Jones [1983] described laminar natural convection in a square cavity, and that this type of convection could apply also to crystal growth systems. In a model of heat transfer for directional crystallisation of silicon ingots Meese *et al.* [2004] also takes into account fluid flow due to natural convection. The convection pattern in the melt of the furnace has been modelled by SINTEF Materials and Chemistry group, but this is a confidential report. We assume that natural convection also applies to our case, resulting thus in a small solute boundary layer. It is therefore assumed that the melt samples gives an indication of the concentrations of carbon and nitrogen in the bulk melt.

4•5 FTIR-measurements

For measurements of the substitutional carbon content in silicon wafers the most employed method is FTIR. This method is widely used by the industry and research institutes for measuring both dissolved carbon and oxygen. It measures only carbon that is at substitutional sites in the lattice. It is thus possible to measure from 0.1 ppma up to the maximum amount of substitutional carbon soluble in solid silicon [ASTM, 2000]. For oxygen it measures oxygen that is at an interstitial position in the lattice, it measures from 0.2 ppma to the maximum amount of interstitial oxygen soluble in silicon [ASTM 93a]. The FTIR method has the advantage of being non-destructive, inexpensive and the measurements are rapid, 2-5 min for each measurement.

Since this instrument had not been employed for such measurements before at the institute, some time and effort was needed to get control of the measurements. A round

robin test was conducted with the participation of two other research institutes and controlled against SIMS-measurements. The results of this test are presented in Chapter 5.

4•5•1 Principle of FTIR-measurements

In infrared spectrometry the radiation emitted excites molecular vibrations when it is absorbed. The absorption occurs at a wavelength (frequency) that is specific for these vibrations, and the energy needed for a type of vibration is determined by the atoms that are bonded together and their environment. The vibrations are stretching or bending of the bonds. Only vibrations producing a shift in the dipole moment are infrared active, and give rise to absorption bands. Figure 4•6 shows a principle sketch of the transmission spectroscopy.

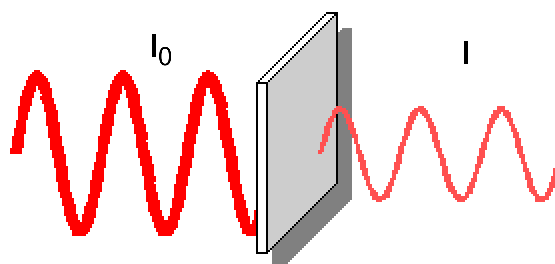

Figure 4•6: Infrared radiation passing through a specimen, where I_0 is the incident intensity and I the intensity after passing the sample.

The relationship between the absorption and the concentration of the species giving rise to the absorption is given by Beer-Lambert's law [Atkins, 1978]:

$$-\log(I/I_0) = -\log(T) = A = \alpha \times c \times d \qquad \text{eq•4•3}$$

where I is the intensity after passing the sample, I_0 is the incident intensity, T is the transmittance, A is the absorbance, α is the molar absorption coefficient of the actual specie, c is the concentration of the specie and d is the thickness of the sample.

Single carbon impurities in silicon occupy substitutional sites where they are bonded tetrahedrally to silicon atoms. Newman, Willis and Smith [1965 and 1969] ascribed an infrared absorption band at 607 cm^{-1} (at 77 K) to the vibrations of carbon

atoms that occupy such sites. Later, these findings have been developed into a standard method for measuring the substitutional atomic carbon content in silicon, as given by the American Society for Testing and Materials (ASTM).

4•5•2 Measurement procedure

The instrument settings for these measurements are given in Table 4•3. Information on the type of surface treatment employed for the reference and samples are included in Table 4.4., as well as size and thickness. Both the round robin test samples and wafer samples from the melt sampling experiments represent different height positions in the block. The wafer samples from the ingot after the experiments were taken out at approximately the same fraction solidified material as the corresponding melt samples. The wafer samples were measured at their centre point. The wafer samples from the melt sampling experiments were measured twice each.

Table 4•3: Instrument type and settings for FTIR-measurements

Instrument	Software	Region	Resolution	No. of scans
Nexus spectrometer from Thermo Nicolet	Thermo Nicolet's OMNIC	900-500 cm^{-1} (C-meas.) 1300-500 cm^{-1} (O-meas.)	2 cm^{-1}	128 256 only for round robin test

When measuring the samples with FTIR a background spectrum is first collected. This spectrum represents the absorption from the atmosphere in the chamber. All the sample spectrum and reference spectrum are automatically ratioed against this background spectrum. In Figure 4•7, a typical sample spectrum is shown. The peak at 605 cm^{-1} with full width at half maximum (FWHM) less than 6 cm^{-1} is the carbon absorption peak. The peak at 1107 cm^{-1} with FWHM of 32 cm^{-1} is the oxygen absorption peak. To calculate the thickness of the sample the reference spectrum is used. In the region between 600-900 cm^{-1} there are several absorption peaks due to silicon lattice vibrations, these peaks are used to calculate a scale factor for thickness, k. The reference spectrum is multiplied by this

scale factor and substracted from the sample spectrum, this gives a “pure” sample spectrum.

$$\text{Pure sample spectrum} = \text{Sample spectrum} - k \times \text{Reference spectrum} \qquad \text{eq•4•4}$$

where k is the scale factor for thickness.

The scale factor is then adjusted by use of a mathematical tool in the program to the value that gives a complete removal of the silicon lattice peaks and the “best” (flattest) baseline. It is thus simply the ratio of the sample thickness and the reference thickness. Since the thickness of the reference is 1 mm, the scale factor represent actually the sample thickness.

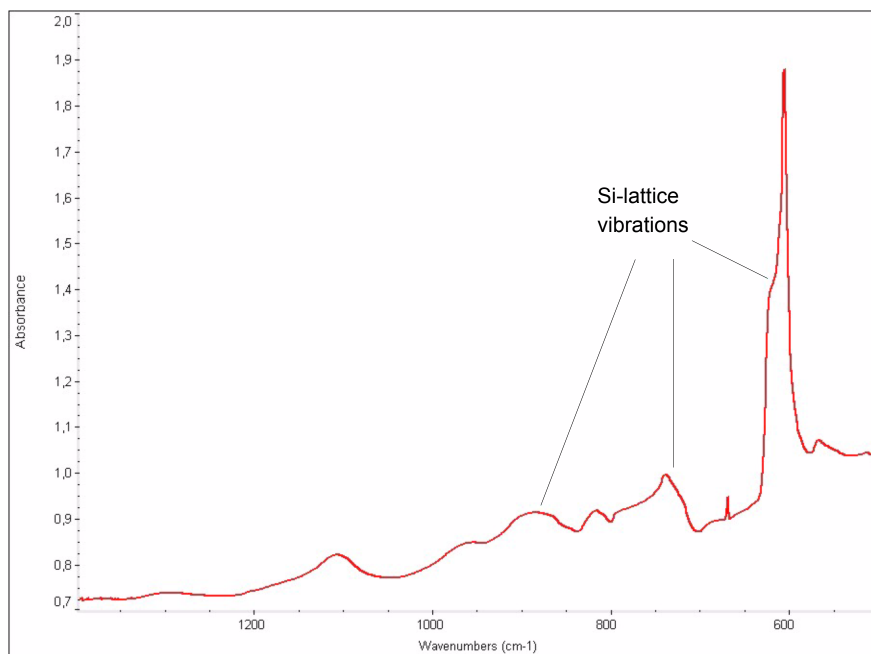

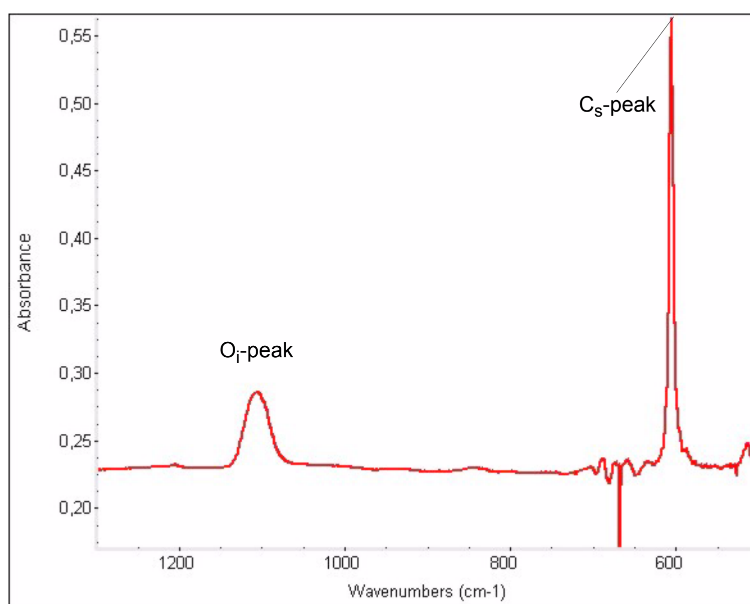

Figure 4•7: FTIR-spectra of a silicon sample in (a) raw spectrum before subtracting the spectrum of the standard, (b) "pure" spectrum after subtraction of the standard spectrum

Table 4•4: Sample and reference information

Material	Surface treatment	Thickness & Size	C- and O- conc.	Resistivity
Wafer samples	Etched for ~ 5 min. in polysetch (50% HF, 70% HNO_3 and CH_3COOH, in ratio 1:3:1)	~ 1.5 mm 3x3 cm^2	see results, chapter 6	~ 1 ohm cm
Round Robin Test samples	Mechanically polished on both sides	1.5- 2 mm 4x4 cm^2	see chapter 5	~ 1 ohm cm
Reference sample (FZ)	Polished on both sides	1 mm diametre 7.5 cm	0.4 ppma	~ 2.5 ohm cm

4•5•3 Calculation of carbon- and oxygen- concentration

The the following expressions from ASTM have been used to calculate the carbon- and oxygen- concentrations in a sample:

Carbon concentration:

The absorption coefficient, α, is calculated from the expression below:

$$\alpha = \frac{23.03}{x} \times (A_p - A_b) \qquad \text{eq•4•5}$$

where x is the sample thickness, A_p is the peak value of the carbon-only absorbance spectrum, and A_b the baseline value of the carbon-only absorbance spectrum. For room-temperature measurements the carbon concentration is calculated from:

$$\text{Carbon conc. (ppma)} = 1.64 \times \alpha \qquad \text{eq•4•6}$$

[ASTM, 2000]

Oxygen concentration:

The peak and baseline absorption coefficients are calculated from the following equations:

$$\alpha_p = -\frac{1}{x}\ln\left[\frac{(0.09\text{-}e^{1.70x}) + \sqrt{(0.09\text{-}e^{1.70x})^2 + 0.36T_p^2 e^{1.70x}}}{0.18T_p}\right] \qquad \text{eq•4•7}$$

$$\alpha_b = -\frac{1}{x}\ln\left[\frac{(0.09\text{-}e^{1.70x}) + \sqrt{(0.09\text{-}e^{1.70x})^2 + 0.36T_b^2 e^{1.70x}}}{0.18T_b}\right] \qquad \text{eq•4•8}$$

where α_p is the peak absorption coefficient, α_b the baseline absorption coefficient, x is thickness (in cm), T_p is peak transmittance and T_b is baseline transmittance. The net absorption coefficient due to interstitial oxygen, α_O, is then expressed as:

$$\alpha_O = \alpha_p - \alpha_b \qquad \text{eq•4•9}$$

The interstitial oxygen content is calculated from:

$$\text{Oxygen concentration (ppma)} = 6.28 \times \alpha_O \qquad \text{eq•4•10}$$

This gives the oxygen concentration at room temperature [ASTM, 1993].

The conversion factors have been determined from calibration curves. Since the discovery of the C_s - and O_i - infrared bands these conversion constants have been continually changed/updated. The conversion constants used in this work are latest versions from ASTM, and were chosen since they are employed by different research institutes.

4•5•4 Factors influencing the measurements

Constants for calculating the concentrations from the absorption coefficient, that is the constants in eq 4•6 and eq 4•10 are different when the measurements are performed at cryogenic temperature (77 K). Variations in the temperature between the recording of spectra can therefore influence the measurements, but for measurements within a

temperature difference of ±2 °C this difference is negligible. In our case the temperature is very close to room temperature and the temperature difference between the measurements is probably smaller than 2 °C [ASTM, 2000].

Scattering of the light at the surface reduces the energy that pass through the sample and thereby reduces the sensitivity. Therefore also, the surface treatment can affect the measurements. It is recommended to measure on double-side polished wafers. The round robin wafers were mechanically polished on both sides, while the wafer samples from the experiments were etched in polish-etch. The polish-etched samples show more topography on the samples (visible grain boundaries), that may give more reflection. When comparing the two surface treatments on the same wafer, the resulting difference in the FTIR-measurements was negligible. Possibly, the surface treatment has a larger effect on thinner samples (less absorbance of the actual energy), and when measuring lower carbon contents in the sub-ppma level.

The measurements are influenced by the resistivity. It is recommended to measure on samples of resistivity greater than or equal to 3 ohm cm for p-type material. Below this resistivity there is a significant free carrier absorption that will reduce the available energy. In samples of very low resistivity the reduction in available energy can be so high that it is impossible to measure the carbon and oxygen concentration. We used samples from ScanWafer ASA, and the resistivity was therefore ~1 ohm cm (p-type material).

4•6 Characterisation of inclusions

Different preparation methods were tried for the study of inclusions. These were mechanical polishing, chemical/mechanical polishing and dissolution. The technique employed on most of the samples were dissolution, because it permitted to study large volumes of the samples, in addition the entire inclusion is revealed and not only a section of it.

4•6•1 Mechanical polishing and chemical/mechanical polishing

For the mechanical polishing the samples were first polished on different emery papers (from 80 mesh to 2400 mesh), finishing with diamond paste of 3 μm and 1 μm. The chemical/mechanical polishing is polishing with a slurry containing silica particles and an alkaline solution. The samples were subsequently polished with water for removal of the silica particles from the slurry that were sticking on to the wafer surface.

4•6•2 Dissolution

The samples were completely dissolved in a traditional etching solution for silicon that contains one part HF (conc. ~50%) and three parts HNO_3 (conc.~70%) [f.in. Kulkarni and Erk, 2000]. This etching solution dissolves silicon, but not SiC, and Si_3N_4 may dissolve very slowly in the etch. In this manner the matrix (silicon) is removed and the inclusions that are resistent against the etching solution remains intact, and can be collected on a filter. The samples were contained in plastic bottles during ethcing. The etch reacts violently with silicon, but the reaction seems to slow down rapidly, and it was necessary to shake the bottles regularly in order to maintain the reaction. The inclusions on the filter paper were rinced in water before being manually transferred to a glass plate with an acetone layer to "glue" the inclusions on to the plate. Also, carbon tape was employed to stick the inclusions to the glass plate. Parametres for the dissolution experiments are given in Table 4•5. Sample parametres are detailed in Tables 6·10 to 6·12. The total reaction for the dissolution is according to Kulkarni and Erk [2000] as follows:

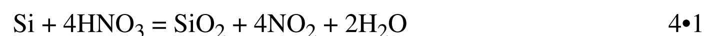

$$Si + 4HNO_3 = SiO_2 + 4NO_2 + 2H_2O \qquad 4•1$$

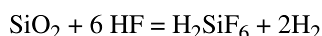

$$SiO_2 + 6\ HF = H_2SiF_6 + 2H_2 \qquad 4•2$$

As is seen from the dissolution reaction above silica particles will dissolve in this etching solution.

Table 4•5: Parametres for dissolution experiments

Etching solution	Solution quantity	Etching time	Filter holder material	Temperature	Filter paper type
HF(50%): HNO_3(70 %) (1:3)	~ 500 - 1000 ml	~ 1-2 days	Ceramic	~ Room temperature, (reaction produces heat)	Cellulose < 2 µm (Schleicher & Schüll)

4•6•3 Inclusion analysis

Both Scanning Electron Microscope (SEM) and Electron Probe Microanalyzer (EPMA) were employed for studying the inclusions. In SEM the Energy Dispersive Spectrometer (EDS) analysis was used for identifying the elements present in the particles. The Electron Backscatter Diffraction (EBSD) in SEM was used for identification of the crystallic structure (phase modification). When using the EPMA, both EDS- and Wavelength Dispersive Spectrometer (WDS) were used for element identification. The EDS-technique scans the energy emitted after bombardment of the sample with high energy electrons, while WDS scans the wavelength of the X-rays emitted. The latter technique (WDS) has better sensitivity than EDS and generally is more accurate [Hjelen, 1989]. In EBSD the sample is tilted ~70° to a plane perpendicular to the electron beam. The sample is tilted to give a higher yield of backscattered electrons. The electrons are diffracted on their way out of the sample, and this diffraction pattern is recorded on a fluorescent screen [Hjelen, 1989]. If the pattern obtained is of good quality an automatic determination of the phase modification is obtained by use of the program package.

The particle size distribution was measured using a Coulter LS 230 laser diffraction particle size analyzer. This method involves the detection and analysis of the angular distribution of light produced by a laser beam passing through a dispersion of particles, in this case the particles were dispersed in water. For a specific material, the scattering

pattern is unique for its size. Correlating the scattering pattern with an optical model (Fraunhofer or Mie) results in the particle size distribution [Delft Solid Solutions web page, 2004]. The method measures from 2000 μm down to 0.04 μm.

4•7 Minority carrier lifetime

As a routine control, of the blocks, the minority carrier lifetime of the blocks is measured in the industry. The material is illuminated with short pulses of light, resulting in a non-equilibrium distribution of carriers. The return of these excess carriers back to equilibrium is measured as a function of time. This decay curve is dependent on the recombination rate. A high lifetime will then indicate a low recombination rate, which is desired for solar cell purposes. Typical recombination centers are crystal defects, impurities in the material and the surface. The minority carrier lifetime gives thus an indication of the quality of the material for solar cell purposes. At ScanWafer the minority carrier lifetime is measured by a Semilab-WT 85.

4•8 Experimental overview

Experimental details on the experiments at ScanWafer ASA's plant in Glomfjord are assembled in Table 4•6. The ingots were sawn in 16 blocks, each of cross section 150x150 mm^2. Block no. 10 and 13, see Figure 4•8, were taken out for FTIR-analysis and study of inclusions. Wafers were sawn from these blocks at heights corresponding approximately to the same fraction solidified as the melt samples were taken. These wafers had a thickness of 1.5 mm. Smaller wafer samples of 30x30 mm^2 were sawn from each large wafer and these were used in the FTIR-measurements. The residual parts of the large wafers were used for inclusion studies. Sawing into wafers was carried out at Meyer & Burger, Switzerland. A schematic overview of the cutting of the ingot is shown in Figure 4•8.

Table 4•6: Experimental data for the experiments at ScanWafer ASA, Glomfjord

Exp.no.	Furnace no.	Mean growth velocity / cm h^{-1}	Total charge /kg	Amount of recycled material in the charge / kg	Ingot rejected	Growth velocity measurements	Melt sampling frequency	FTIR wafer measurements
1	22	1.75	265	50	Yes	In position 4	~ each hour	Yes
2	23	1.75	265	50	No	In position 3	~ each hour	Yes
3	23	1.1	255	25	Yes	-----------------	~ each 2 hours	Yes
4	23	1.3	265	Only “tops and tails” + “chips and chunks”	No	In position 4	~ each 2 hours	No

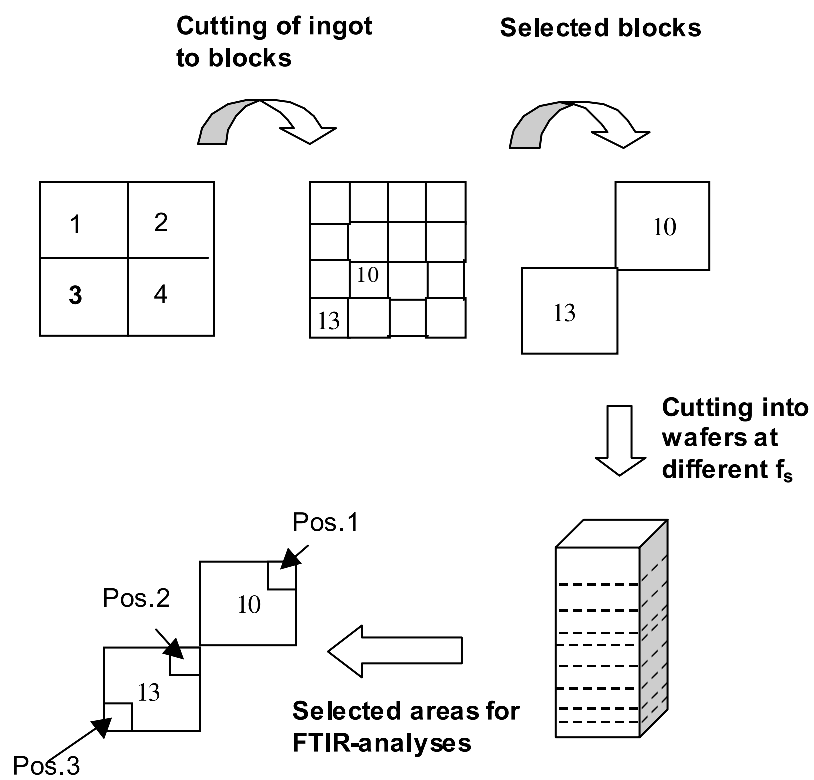

Figure 4•8:Schematic view of the cutting of the ingot after melt sampling, selection of areas for FTIR-measurements and inclusion study

REFERENCES

The American Society for Testing and Materials (ASTM) (1993), *Standard test method for Interstitial Atomic Oxygen Content of Silicon by Infrared Absorption*, Designation: F 1188 - 93a

The American Society for Testing and Materials (ASTM) (2000), *Standard Test Method for Substitutional Atomic Carbon Content of Silicon by Infrared Absorption*, Designation: F1391 - 93 (Reapproved 2000)

Atkins P.W. (1990), *Physical Chemistry*, 4th edition Oxford University Press

De Vahl Davis G. and I.P.Jones (1983), Natural convection in a square cavity: *A comparison exercise, International journal of numerical methods in fluids*, Vol.3, 227-248

Delft Solid Solutions web page, http://www.solids-solutions.com/sizing.html, accessed May 2004

Hjelen J. (1989), *Scanning elektron-mikroskopi*, Institute of Materials Technology, Norwegian Technical University, Trondheim (Norway)

Kulkarni S.M. and H.F.Erk (2000), *Acid-Based Ethcing of Silicon Wafers: Mass-Transfer and Kinetic Effects*, J.Electrochem.Soc., Vol.147, no.1, 176-188

Meese E.A., E.J.Øvrelid, H.Laux and M.M'Hamdi (2004), *Modelling of directional crystallization of silicon ingots - Heat transfer and experimental validation*, 19th European Photovoltaic Solar Energy Conference and Exhibition, Paris

Newman R.C. and J.B.Willis (1965), *Vibrational absorption of carbon in silicon*, J.Phys.Chem.Solids 26, 373-379

Newman R.C. and R.S.Smith (1969), *Vibrational absorption of carbon and carbon-oxygen complexes in silicon*, J.Phys.Chem.Solids 30, 1493-1505

Chapter 5 Round robin test

In order to verify our measurements a round robin test (rrt) was conducted with two other research institutes. Participating in the test was the University of Milano-Bicocci (UniMiB) and the Energy Research Centre of the Netherlands (ECN).

As a final control of the FTIR measurements, Secondary ion mass spectrometre analysis was performed on three of the samples. The SIMS analysis were conducted by Cascade Scientific.

Some samples were also measured in industry (SiNor AS, Glomfjord) with FTIR. These measurements were automatic, performed directly by the software.

5•1 Results round robin test

The samples employed in the round robin test (rrt) are from a block of an ingot, samples were retrieved at different height positions (f_s), see Table 5•1. The samples were squares of 40x40 mm^2 and 1.5-2 mm thick. The resistivity decreases slightly with increasing f_s due to segregation of boron, see Table 5•1.

The samples were mechanically polished on both sides. For instrument settings see Table 4·3. The samples were measured at their centre point and five consecutive measurements were carried out on each sample.

The results of the round robin test together with the results of the SIMS-measurements are presented in Figures 5•1 and 5•2. The standard deviation for the FTIR-measurements (UniMib and NTNU) and the estimated error (ECN) are given in brackets in Table 5•2. The measurements by SiNor AS (FTIR) and Cascade Scientific (SIMS) are also listed in Table 5•2.

The SIMS-technique is destructive and measures the total amount of elements. The analysing area is small. LOM-studies of the rrt-samples, revealed no inclusions. It is

therefore assumed that SIMS will measure the content of dissolved carbon in the samples. This assumption correlates well with the results.

Table 5•1: Approximate f_s for the round robin test samples

Sample no.	Approximate fraction solidified, f_s	Resistivity / ohm cm
1	0.98	1.14
2	0.83	1.20
3	0.66	1.33
4	0.50	1.34
5	0.33	1.35
6	0.16	1.42
7	0.13	1.58

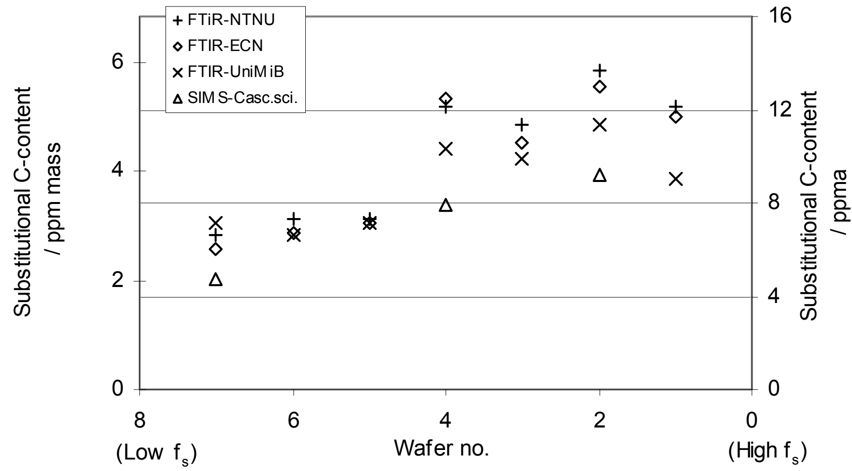

Figure 5•1: Substitutional carbon concentrations for the wafers. Results of round robin test.

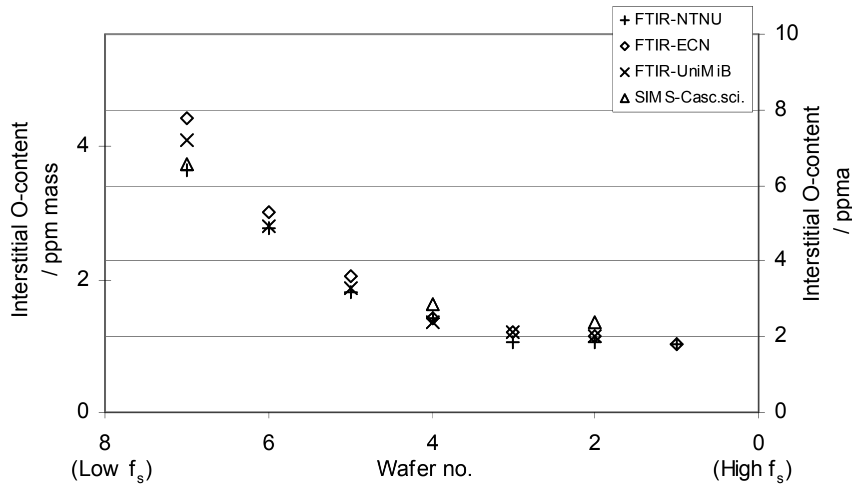

Figure 5•2: Interstitial oxygen concentrations for the wafers. Results from round robin test.

Table 5•2: Results of the Round Robin Test, values in brackets are standard deviation for NTNU, UniMiB, SiNor AS, Cascade Scientific and estimated error for ECN

Sample no	NTNU (FTIR)		ECN (FTIR)		UniMiB (FTIR)		SiNor AS (FTIR-automatic)		Casc.Sci. (SIMS)	
	C-conc. /ppma	O-conc. /ppma	C-conc. /ppma	O-conc. /ppma	C-conc. /ppma	O-conc. /ppma	C-conc. /ppma	O-conc. /ppma	C-conc. /ppma	O-conc. /ppma
1	12.10 (0.13)	1.79 (0.07)	11.7 (0.76)	1.8 (0.87)	9.07 (0.10)		9.35 (0.06)	2.25 (0.01)		
2	13.65 (0.34)	1.85 (0.01)	13.0 (0.76)	2.0 (0.87)	11.33 (0.14)	2.01 (0.02)			9.21 (0.60)	2.40 (0.13)
3	11.33 (0.42)	1.85 (0.02)	10.6 (0.76)	2.1 (0.87)	9.88 (0.34)	2.10 (0.02)	8.50 (0.09)	2.45 (0.00)		
4	12.14 (0.15)	2.47 (0.01)	12.5 (0.76)	2.5 (0.87)	10.36 (0.35)	2.40 (0.06)			7.95 (0.23)	2.87 (0.10)
5	7.34 (0.16)	3.20 (0.01)	7.1 (0.76)	3.6 (0.87)	7.14 (0.07)	3.30 (0.01)	5.76 (0.02)	3.47 (0.02)		
6	7.30 (0.21)	4.87 (0.04)	6.7 (0.76)	5.3 (0.87)	6.64 (0.19)	4.90 (0.10)	5.45 (0.02)	4.75 (0.02)		
7	6.59 (0.22)	6.41 (0.04)	6.0 (0.76)	7.8 (0.87)	7.14 (0.13)	7.20 (0.13)			4.71 (0.16)	6.57 (0.34)

5•2 Summary

There is a fairly good accordance between the oxygen measurements. This is not the case for the carbon measurements. The measurements by ECN and NTNU show good correspondence, but the SIMS measurements are remarkably lower. The SIMS technique is one of the best surface analysing techniques. If we consider that the carbon concentration is constant over the sample thickness (1.5 mm) and that there are no inclusions in the analysed area, then the SIMS analysis should give a precise analysis of the amount of dissolved carbon in the sample. The precision and accuracy for these SIMS analyses are 10-20%. Detection limits for carbon is 0.3 ppma ($1.5x10^{16}$ atoms cm^{-3} and for oxygen 1.2 ppma ($6x10^{16}$ atoms cm^{-3}) with the instrument conditions employed for these analyses.

The FZ-silicon sample used as reference sample in the FTIR-measurements was also analysed with SIMS, the carbon content they obtained was 0.33 ppma. From the purchaser of this FZ-sample the C-content, Virginia Semiconductor, the carbon content should be 0.4 ppma (the measurement method was not given). This is a good correspondence, and the SIMS measurements seem to give a rather precise carbon analysis. Therefore the FTIR measurements probably overestimates the carbon content. This can be explained by the previously mentioned free carrier absorption in the samples, caused by their low resistivity (Recommended resistivity on p-type material is > 3 ohm cm for carbon measurements). Energy is absorbed not only from substitutional carbon, but also from the free carrier concentration in the sample. Thus a higher value is obtained for the carbon absorption. This effect could perhaps have been reduced if the sample and reference had the same resistivity. From Table 4•4 we see that the difference in resistivity between the reference and the samples is 1.5 ohm cm. The free carrier absorption is proportional to the carrier density and to the square of the wavelength [O'Mara *et al.*, 1990], it is thus greater at lower wavenumbers. From our measurements it is also seen that the carbon absorption which occurs at a lower wavenumber (605 cm^{-1}) than the oxygen absorptioin (1107 cm-1), are more affected by the free carrier absorption.

The measurements by UniMiB gave lower carbon values for samples 1-4 than the ones by NTNU and ECN, but not for samples 5-7. Important to notice here is that ECN and NTNU used exactly the same procedure to obtain the carbon contents (the ASTM

procedure), while UniMiB had to make a little change in this procedure. They had to normalise on the 734 cm^{-1} peak instead of the peak at 620 cm^{-1}, because of bad spectrum quality in this area.

The measurements by Sinor AS corresponds the best with the measurements by SIMS. Sinor AS has a software that measures automatically the carbon and oxygen contents, the program package has a reference spectrum that was used in these measurements. In addition the program contains various correction factors.

Looking on the rr-test, the FTIR measurements of 12-14 ppma C is 4-4.5 ppma higher than the SIMS measurements, and the FTIR measurement of 6.6 ppma is 1.9 ppma higher than the SIMS measurements. The fact that the highest difference between the SIMS and FTIR measurements are for samples from high f_s, further reinforce that this discrepancy can be due to the low resistivity. The resistivity decreases with increasing f_s due to segregation of boron.

In conclusion, it is probable that the FTIR measurements conducted on low resistivity samples (< 3 ohm cm) overestimate somewhat the carbon content.

REFERENCES

O'Mara W.C., R.B.Herring and L.P.Hunt (1990), Handbook of Semiconductor Silicon Technology, Noyes Publications

Chapter 6 Results

Presented in this section are the results from the melt-sampling experiments and the subsequent solid phase characterisation. The routine minority carrier lifetime scans (in industry) of the blocks prior to sawing are also presented.

6•1 Results from the melt sampling experiments

The carbon content from the test experiment is presented first in this section. Subsequently the carbon content, local growth rates and temperature (pyrometer readings at the melt surface in crucible position 1) from the four melt sampling experiments are presented (see section 4·1 for details on temperature readings). The carbon contents in the figures are given as mean values with standard deviation bars. As the time span of the experiments is from January-03 till December-03, they are presented in chronological order, starting with the test run. The results from the nitrogen and oxygen analyses, including microscopic studies of selected samples are given at the end of this section.

6•1•1 Test experiment (January-03)

A test of the sampling equipment and procedure was first conducted. This consisted of taking out three melt samples during the holding period prior to crystallisation start, see Table 4·1. The first sample was taken out right after entering the holding stage. The subsequent two samples were taken at 10 minutes intervals.

The carbon content in these three samples range from 9 to 16 ppm mass. There seems to be no systematic change in the carbon content during the time elapse. The variations in content measured are taken to give an indication of the sampling and chemical analysis error.

Table 6•1: Carbon contents from test run (combustion IR-absorption, LECO)

Sample no.	C-content /ppm mass	Mean C-content /pmm mass	Time between sampling /min
1	8/19/20	16	10
2	8/6/13	9	
3	9/8/21	13	

6•1•2 Melt sampling experiment no. 1, MS-Exp 1 (March-03)

Furnace 22 was used in this experiment. Mean carbon contents, temperature and growth rate are shown graphically in Figure 6•1, and their values are listed in Table 6•2, including the carbon contents for all parallels.

The carbon content in the melt starts at 43 ppm mass and increases steadily during the whole crystallisation. Generally the growth rate decreases steadily with increasing fraction solidified due to the low heat conductivity of solid silicon. Larger variations from this general trend may be due to the experimental errors connected to these measurements, as described in section 4·3·5 these measurements have a low reliability.

The temperature prior to crystallisation start is ~1500 °C. The temperature in the melt at this stage is probably homogeneous, since the temperature measurements from the top and bottom are close. The surface temperature decreases steadily during the crystallisation.

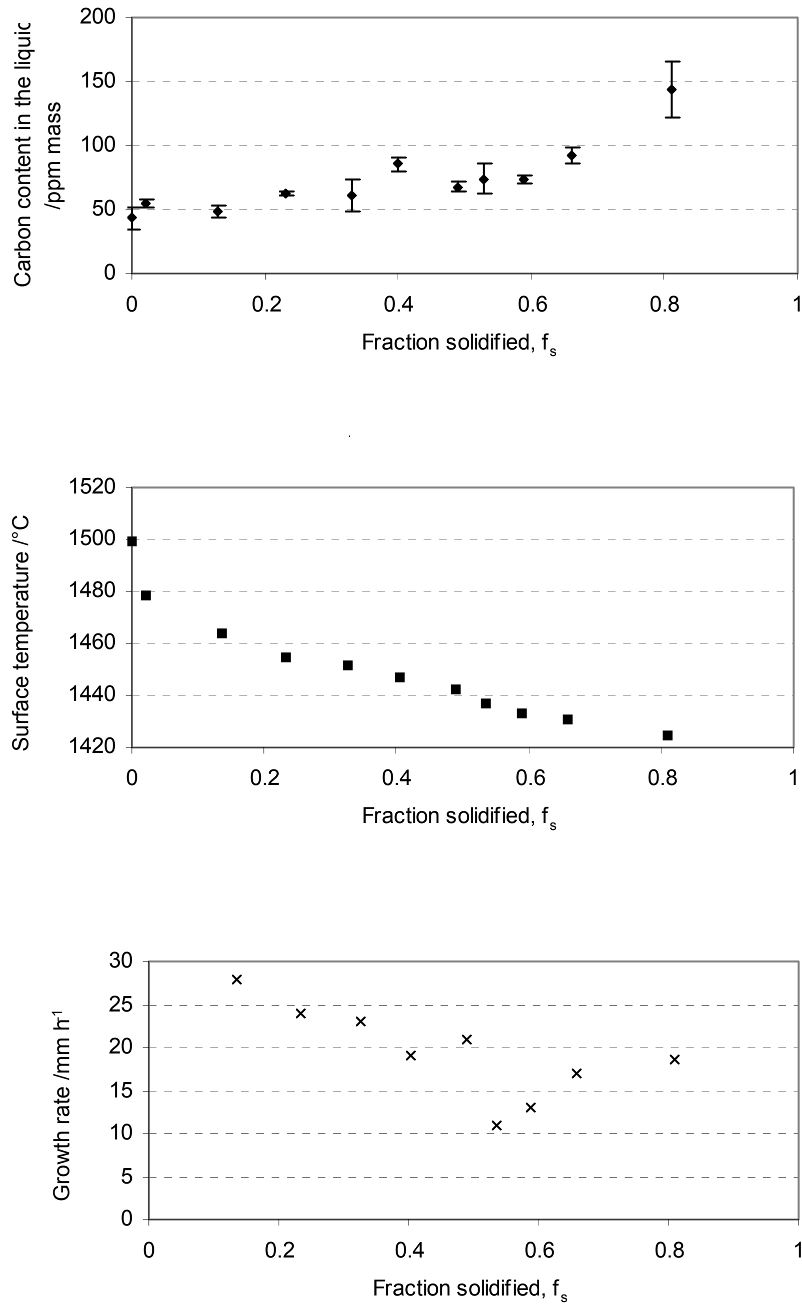

Figure 6•1:Carbon content, surface temperature and growth rate as a function of fraction solidified for MS-Exp1.

Table 6•2: Experimental values from MS-Exp1

Sample no.	Fraction solidified	Carbon content 3 parallells / ppm mass	Mean carbon content /ppm mass	Surface temperature /°C	Surface temperature /K	Local growth rate /mm h^{-1}
1	0	46/34/50	43	1499	1772	---
2	0.02	57/56/51	55	1478	1751	5
3	0.13	44/54/47	48	1464	1737	28
4	0.23	62/61/65	63	1455	1728	24
5	0.33	53/76/56	62	1452	1725	23
6	0.40	92/83/81	85	1447	1720	19
7	0.49	66/69/71	68	1442	1715	21
8	0.53	87/65/69	74	1437	1710	11
9	0.59	70/75/75	73	1433	1706	13
10	0.66	89/99/87	92	1431	1704	17
11	0.81	147/120/164	144	1425	1698	19

6•1•3 Melt sampling experiment no. 2, MS-Exp 2 (May-03)

Furnace 23 was used in this experiment. In this experiment we had the opportunity to measure the growth rate in the same crucible (crucible pos.3) as the sampling occurred. The growth rate was then measured approximately in the middle of the crucible. Two deeper samples were also collected from the melt in this experiment. Figure 6•2 shows the approximate positions for sampling of these deeper samples. For the first deep sample the distance to the bottom of the crucible was approximately 60 mm whereas for the second deep sample the distance to the crystallisation front was approximately 20-30 mm.

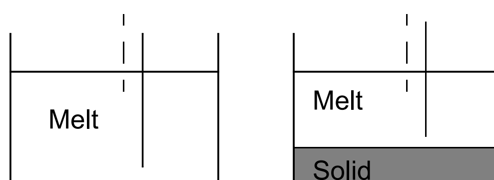

Figure 6•2: Sketch showing the sampling position for the extraction of the deeper samples, dashed lines show the position for "normal sampling"

The results from MS-Exp 2 are shown in Figure 6•3 and Table 6•3. The starting content of carbon in this experiment was 33 ppm mass (27 ppm mass for the deep sample). The carbon content profile during the crystallisation shows sudden high values and increases suddenly to 133 ppm mass at $f_s = 0.72$. Above this f_s it decreases down to 40-50 ppm mass. This observation is not necessarily reliable, and could be caused by fluctuations in the sample and/or preparation quality.

For some of the samples the standard deviation is high, which indicates that carbon is inhomogeneously distributed in the sample. This can stem from a not optimal quenching, see section 4·3·3. Therefore one can expect that the carbon content is highest in the center of the sample sylinder. For this reason some of the samples were not only analysed as lumps, but sliced into neat sylinders (5-7 mm long) with flat sides. The results show a tendency of lower standard deviation for the sliced sylinders compared to the ordinary lump sylinders, see Table 6•4.

The surface temperature profile starts off at 1500 °C also here, and decreases steadily during crystallisation.

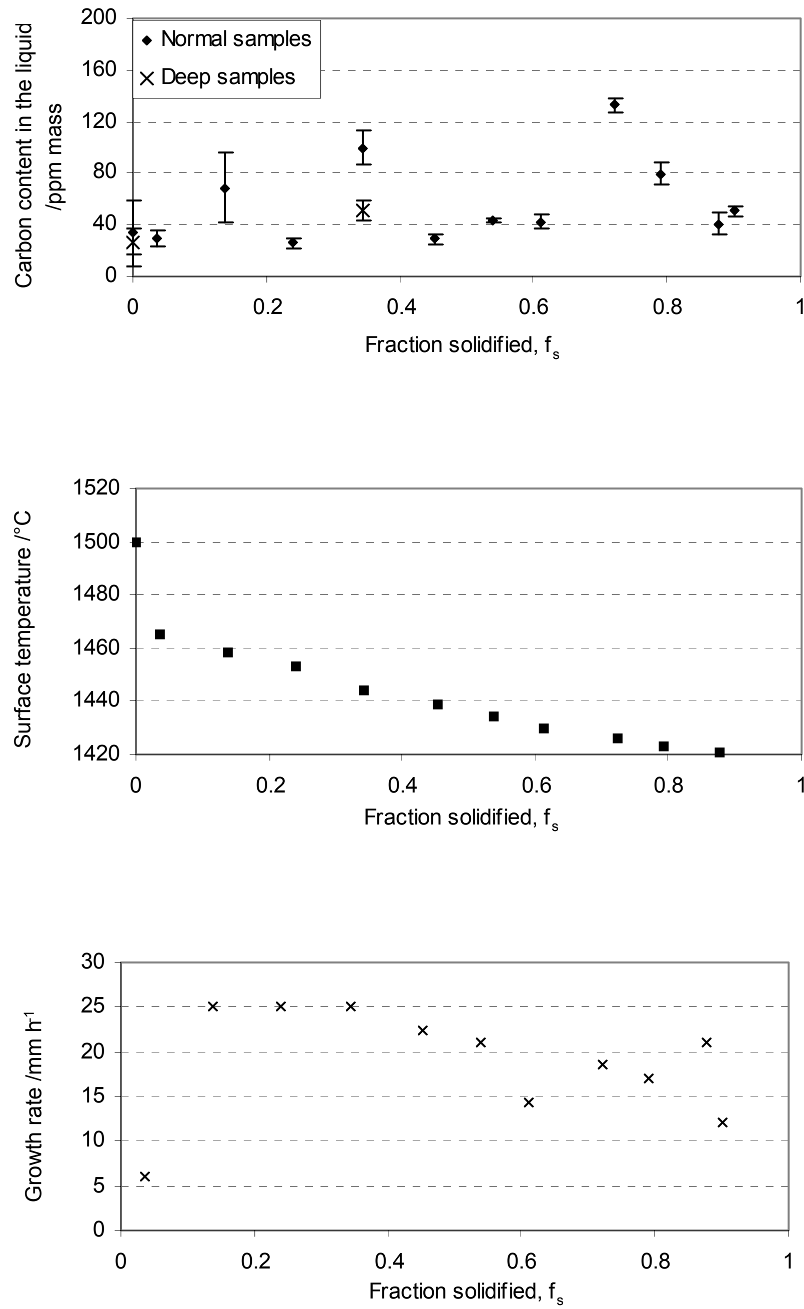

Figure 6•3: Carbon content, surface temperature and growth rate as a function of fraction solidified for MS-Exp 2

Table 6•3: Experimental values from MS-Exp 2, in brackets mean for deep samples

Sample no.	Fraction solidified	Carbon content parallells / ppm mass	Deep sample parallells /ppm mass	Mean carbon content / ppm mass	Surface temperature / °C	Surface temperature / K	Local growth rate / mm h^{-1}
1	0	19/17/33/19/79	29/16/36	33 (27)	1500	1773	---
2	0.04	33/33/22		29	1465	1738	6
3	0.14	47/99/60		69	1458	1731	25
4	0.24	25/30/23		26	1453	1726	25
5	0.34	113/99/88	60/46/47	100 (51)	1444	1717	25
6	0.45	26/34/31		29	1439	1712	23
7	0.54	43/43/45		44	1434	1707	21
8	0.61	49/39/39		42	1430	1703	14
9	0.72	136/127/135		133	1426	1699	19
10	0.79	74/75/89		79	1423	1696	17
11	0.88	47/44/31		41	1421	1694	21
12	0.90	47/54/51		51	1419	1692	12

Table 6•4: Comparison of carbon analysis for lump sylinders and sliced sylinders

Sample no.	Ordinary lump sylinder parallells / ppm mass	Mean (st.dev.)	Sliced sylinder parallells / ppm mass	Mean (st.dev.)
1	34/87/45	55 (28)	19/17/33/19/ 79	33 (26)
5 (deep sample)	170/55/91	105 (59)	60/46/47	51 (8)
6	30/33/68	44 (21)	26/34/31	29 (5)
8	148/204/185	146 (60)	49/39/39	42 (6)

6•1•4 Melt sampling experiment no. 3, MS-Exp 3 (September-03) : Reduced growth rate, reduced quantity of recycled material in the feedstock

Furnace 23 was used in this experiment. The amount of recycled material in the feedstock was lower than in the two previous experiments and the growth rate was reduced, for details see Table 4·6. Due to practical problems during the experiment, the growth rate was not measured. The fraction solidified is therefore an estimate based on comparison with MS-Exp 4 where a similar growth rate was employed. Figure 6•3 and Table 6•5 show the results.

The measured carbon content in these samples are much lower than in the previous experiments, as low as 1 and 2 ppm mass, but higher values of 20-30 ppm mass was measured in some of the samples.

The quality of the melt samples retrieved in this experiment were not as “good” as in the two previous experiments. The samples were this time smaller, only a 10-20 mm long, and some of the samples were actually hollow. This may have affected the analyses. When comparing with the FTIR-measurements from the ingot (see Figure 6•13), these melt sampling results appear to be erroneous. Whether this error comes from the chemical analysis or the sampling procedure is unclear. In the Discussion (chapter 7) these melt-sampling results will be discarded.

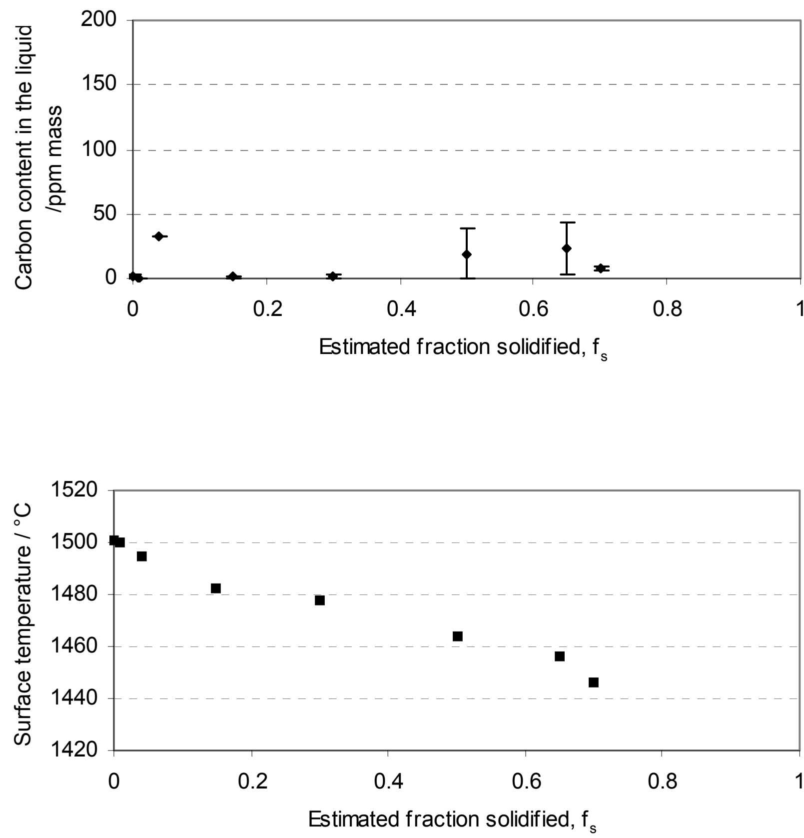

Figure 6•4: Carbon content and surface temperature as a function of time/total time for MS-Exp 3.

Table 6•5: Experimental values from MS-Exp 3

Sample no.	Estimated fraction solidified, f_s	Carbon content parallells / ppm mass	Mean	Surface temperature / °C	Surface temperature / K
1	0	2/0/3	2	1500	1773
2	0.01	0	0	1500	1773
3	0.04	33	33	1494	1767
4	0.15	1/1/2	1	1482	1755
5	0.30	0/2/3	2	1477	1750
6	0.50	41/6/11	19	1464	1737
7	0.65	11/11/46	23	1456	1729
8	0.70	8/10/7	8	1446	1719

6•1•5 Melt sampling experiment no. 4, MS-Exp 4 (December-03) : Reduced growth rate, “pure” feedstock

Furnace 23 was used in this experiment. Also in this experiment the growth rate was reduced compared to the two first experiments. What is special about this experiment is the use of “pure” feedstock. No recycled material was added to the charge. The feedstock used was “chips and chunks” from the polysilicon process (second grade polysilicon) and “tops and tails” from the CZ-process, for further description of these categories of material see Table 1·1.

The results from this experiments are given in Figure 6•5 and in Table 6•6. The first two melt samples were both withdrawn from the melt at $f_s = 0$ (prior to crystallisation start), but with 1 hour between the sampling. This means that the second melt sample was retrieved at the end of the holding period, thus just prior to crystallisation start. The first two samples had a carbon content of 18- and 19-ppm mass, respectively. After these samples the sampling interval was approximately ~ 2 hours. The carbon content increases gradually up to 55 ppm mass and then decreases slightly for the last two samples.

As in the previous experiments the surface temperature starts at 1500 °C, and decreases steadily during crystallisation.

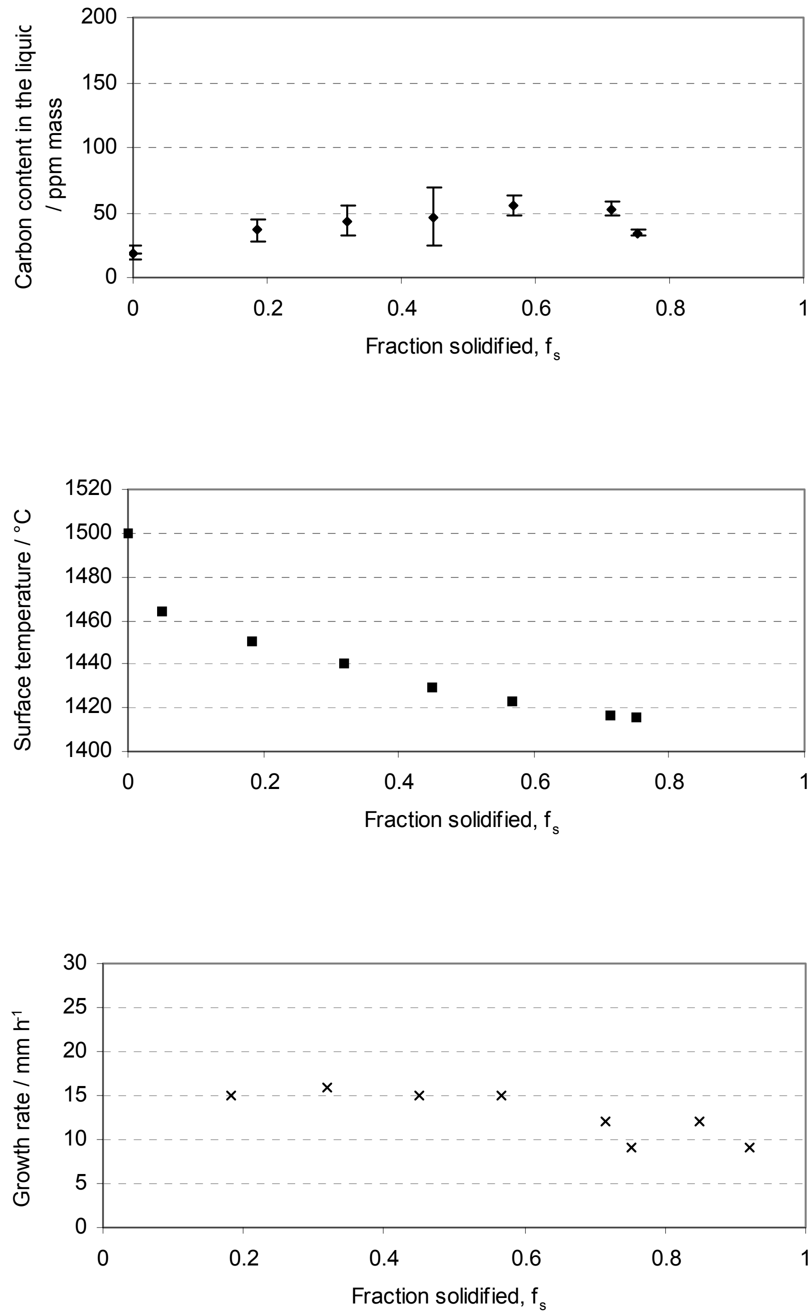

Figure 6•5: Carbon content, temperature and growth rate as a function of fraction solidified for MS-Exp 4

Table 6•6: Experimental values from MS-Exp 4

Sample no.	Fraction solidified	Carbon content parallells / ppm mass	Mean carbon content / ppm mass	Surface temperature / °C	Surface temperature / K	Local growth rate / mm h^{-1}
1	0	18	18	1509	1782	---
2	0	25/16/17	19	1463	1736	---
3	0.18	46/33/30	36	1450	1723	15
4	0.32	41/56/33	43	1440	1713	16
5	0.45	55/64/21	47	1429	1702	15
6	0.57	53/64/49	55	1423	1696	15
7	0.71	50/49/59	53	1416	1689	12
8	0.75	34/35/37/32	35	1415	1688	9
9	0.85					12
10	0.92					9

6•1•6 Nitrogen- and oxygen- analysis of selected melt samples

Some samples from the four melt sampling experiments have been selected for nitrogen- and oxygen- analysis. The results of these analyses are shown in Tables 6•7 and 6•8. The fraction solidified increase with decreasing surface temperature. As the crystalliation proceeds the melt temperature decrease. We see a clear tendency of decreasing nitrogen content in the melt with decreasing temperature (and increasing f_s). The same tendency is observed for oxygen.

Table 6•7: Nitrogen content in selected samples

Experiment	Fraction solidified, f_s	Mean nitrogen content / ppm mass	Standard deviation	Temperature / °C
MS-Exp 1	0	44	±6	1499
	0.23	17	±1	1455
	0.53	14	±3	1437
MS-Exp 3	0	10		1500
	0.30	18	±6	1477
	0.70	8.1	±1	1446
MS-Exp 4	0	12		1463
	0.45	11		1429
	0.75	7		1415

Table 6•8: Oxygen content in selected samples

Experiment	Fraction solidified, fs	Mean oxygen content / ppm mass	Standard deviation	Temperature / °C
MS-Exp 1	0	7.5	±2	1499
	0.23	5.4	±1.6	1455
	0.59	300[1]		1433

Table 6•8: Oxygen content in selected samples

Experiment	Fraction solidified, fs	Mean oxygen content / ppm mass	Standard deviation	Temperature / °C
MS-Exp 3	0	3.2	±1.4	1500
	0.15	2.2	±1.1	1453
	0.65	1.9	±0.9	1434
MS-Exp 4	0	12	±5	1463
	0.45	4.7	±0.4	1429

1. Possibly rest of quartz on the sample

6•1•7 Metallographic studies of selected melt samples

Some of the melt samples were selected for microscopic studies with light optical microscope (LOM), SEM and EPMA. Inclusions were found only in a few samples. All the inclusions were found towards the center of the sample, see Figures 6•6 and 6•7.

The WDS-analysis of all the inclusions indicated that they mainly consist of nitrogen and silicon. However, we also got a small signal on carbon and oxygen, and therefore we performed a quantitative analysis of selected areas. The results of these analyses are presented in Table 6•9. We see from these results that also the pure matrix gives a signal on carbon, that is actually higher than for the particles. We therefore conclude that the carbon signal is probably due to the carbon layer that is added to the sample surface to make them conductive (standard procedure when the samples are moulded in plastic resin).

Table 6•9: Quantitative analyses of inclusions in melt sample by WDS (sample 9 from MS-Exp 1)

Analysis area	Carbon / atom%	Nitrogen / atom%	Oxygen / atom%	Si / atom%
1	8.4	43.8	1.2	46.6
2	12.7	0	0.7	86.4

Table 6•9: Quantitative analyses of inclusions in melt sample by WDS (sample 9 from MS-Exp 1)

Analysis area	Carbon / atom%	Nitrogen / atom%	Oxygen / atom%	Si / atom%
3	8.1	42.2	1.3	48.4
4	6	52.2	0.9	40.9

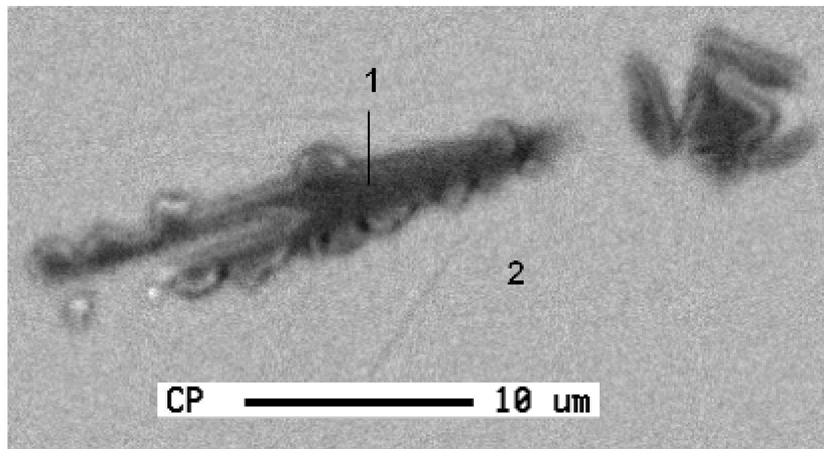

Figure 6•6: Inclusions in melt sample no. 9 (MS-Exp1), WDS-analysis at positions 1 and 2, EPMA picture

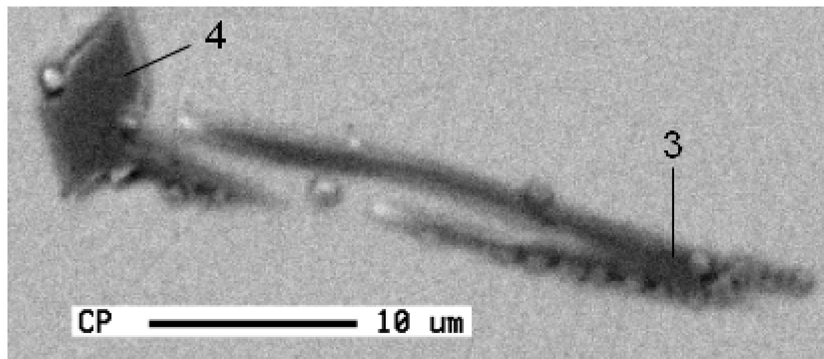

Figure 6•7: Inclusions in melt sample no. 9 (MS-Exp1). WDS-analysis at position 3 and 4, EPMA picture

6•1•8 Minority carrier life-time measurements of selected blocks

Block number 10 (mid-block) from MS-Exp 1, MS-Exp 2 and MS-Exp 4 had a minority carrier life-time scan prior to sawing into wafers. For MS-Exp 1 the minority carrier lifetime scan of one block side is shown as a picture in Figure 6•8, whereas for MS-Exp 2 and MS-Exp 4 the average minority carrier lifetime scan of one block side is graphically shown in Figures 6•9 and 6•10. From these figures it is seen that the minority carrier lifetime measurements from MS-Exp 1 are rather distinctive from the two others, showing a sudden region in the center of the block with abnormally low minority carrier lifetime. The low minority carrier lifetime regions in the top and bottom of the block are "classical" features for lifetime scans of this type of material and common in all three figures. In the bottom and the sides of an ingot the reduction in minority carrier life-time is connected to the diffusion of metallic impurities from the crucible/coating during cool-down, while in the top it is connected to the segregated impurities [Geerligs, 2002 and Acciarri *et al*., 1995].

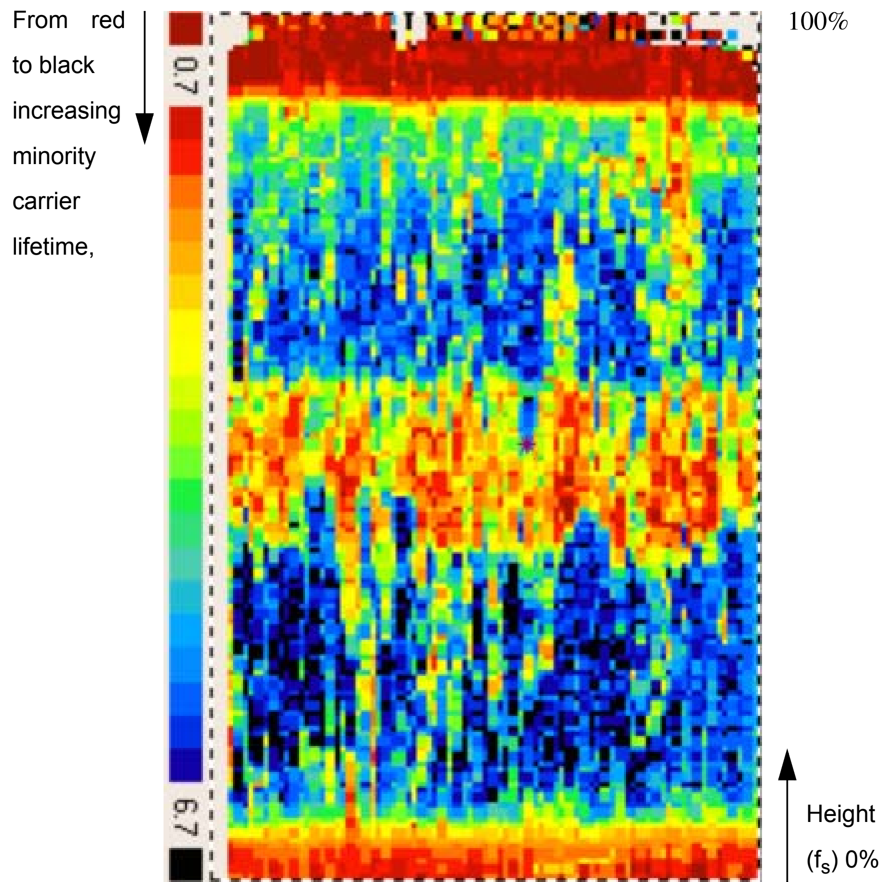

Figure 6•8: Life-time scan of side 1, block 10 from MS-Exp 1. From red to black, increasing lifetime in μs. Measured in Glomfjord.

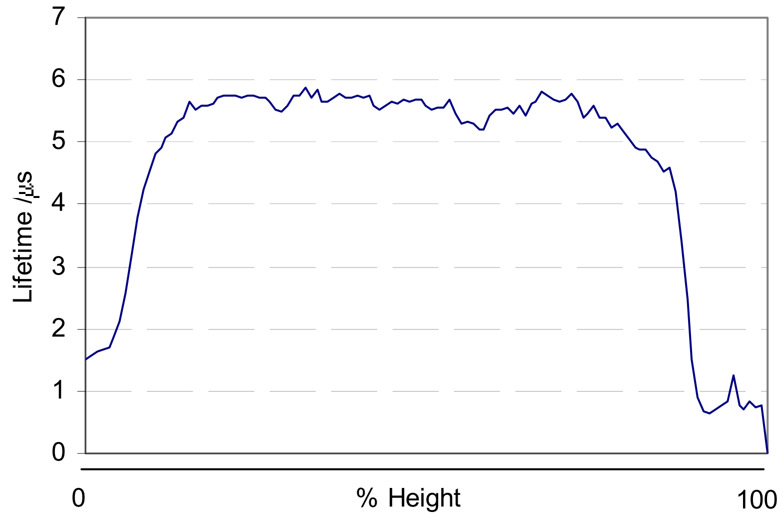

Figure 6•9: Lifetime scan of block 10, side 2 from MS-Exp 2. Measured in Glomfjord.

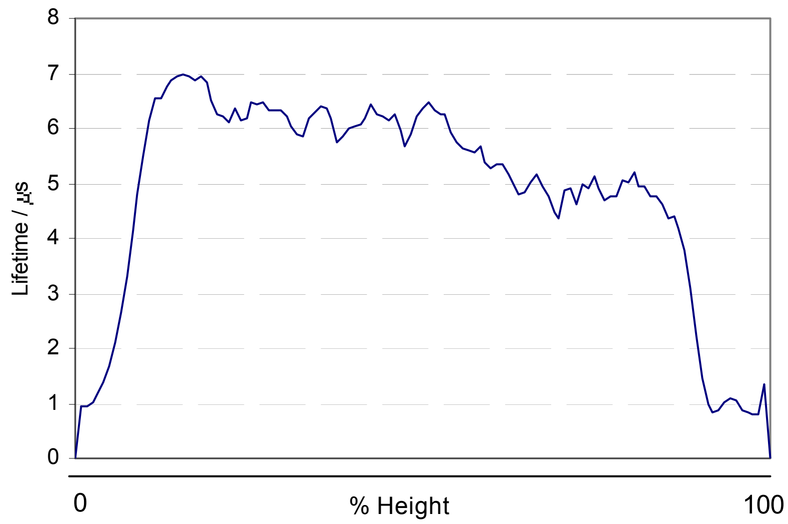

Figure 6•10: Lifetime scan of block 10, side 2 from MS-Exp 4. Measured in Glomfjord.

6•2 FTIR-measurements of wafers

Wafers were sawn from block 10 (mid-block) and block 13 (corner-block) from the ingot at the positions where the melt samples were withdrawn. The measurements in positions 1, 2 and 3 on wafers from MS-Exp1, MS-Exp 2 and MS-Exp 3 are shown in Figures 6•11, 6•12 and 6•13. For raw data values see APPENDIX 3. For references to blocks and position numbers see Figure 4·6 .

The starting carbon content for these three experiments range from 5.0 ppma to 7.2 ppma, it goes through a peak value ranging from 12.2 ppma to 17 ppma, and the end value range from 8.7 ppma to 9.4 ppma.

For MS-Exp 1 there is a clear tendency of lower carbon contents for position 2 and 3 (corner) than for position 1 (middle) for $f_s < 0.6$. At higher f_s the carbon profile flattens out and the carbon contents at the different positions approach each other. The tendency of lower carbon contents at corner positions is not observed for MS-Exp 2, but the carbon profile flattens out at high f_s. For MS-Exp 3 we observe a tendency of lower carbon contents at position 3 compared to positon 1 and 2 for $f_s < 0.6$, and the profile seem to flatten out at high f_s, although less pronounced than for the two previous experiments.

A general trend in these three experiments is that the maximum carbon concentration appears at f_s between 0.4 and 0.6, the carbon profile has a peak at this point. Above the peak value the curve tends to flatten out.

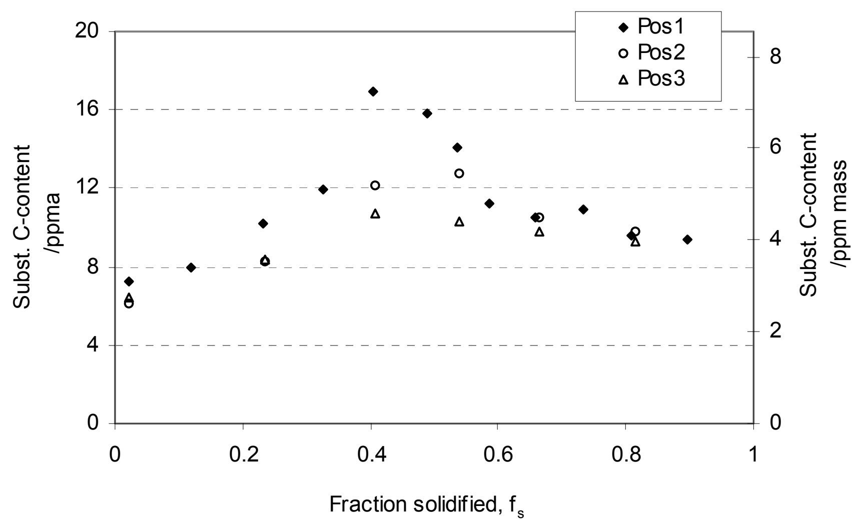

Figure 6•11: Substitutional carbon content as a function of fraction solidified for MS-Exp 1

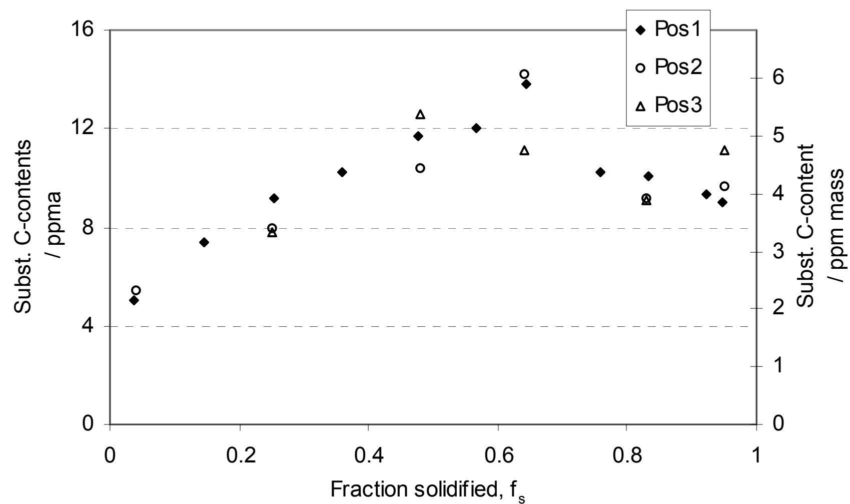

Figure 6•12:Substitutional carbon content as a function of fraction solidified for MS-Exp 2

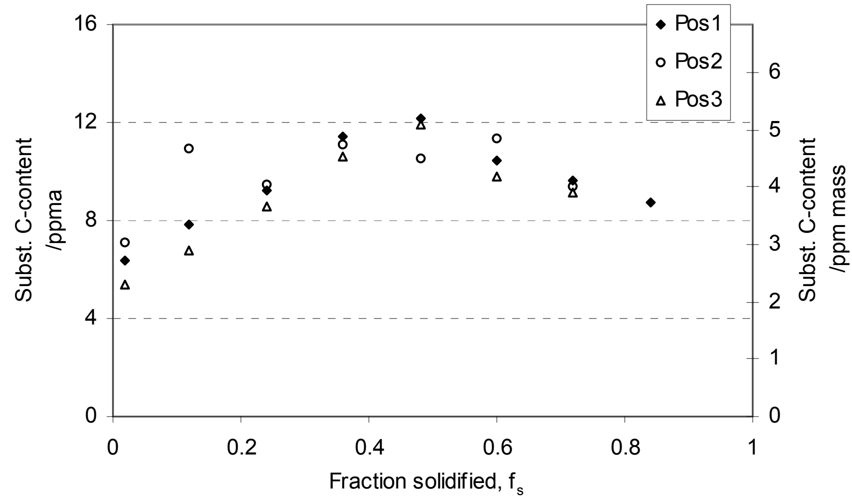

Figure 6•13:Substitutional carbon content as a function of fraction solidified for MS-Exp 3

6•3 Characterisation and identification of inclusions

The characterisation work on inclusions includes both top-cut samples and wafers selected at various f_s , as detailed in Tables 6•10 to 6•12. Top-cut samples refers to the upper cut of the block, which is 20-30 mm in thickness. This means that it includes the “carbide cut” (upper ~5 mm) that is normally rejected by the industry, see illustration below (Figure 6•14).

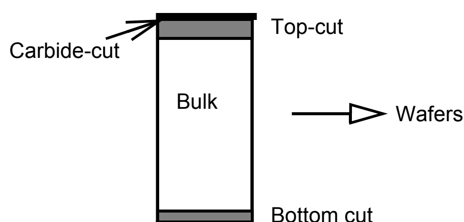

Figure 6•14: Sketch illustrating the different parts of the block

6•3•1Mechanically polished samples

Initially, the study of inclusions started out by investigating mechanically polished areas. These showed only a few inclusions, see Figures 6•15 and 6•16. In total an area of ~ 20 cm^2 was investigated. Two different types of inclusions were found, one that consisted of silicon and carbon and the other composed of silicon and nitrogen (EDS-analysis). Several inclusions like the ones in Figure 6•15 were observed in the samples investigated, these often appeared with hexagonal shape or as elongated needles. They always gave signal on silicon and nitrogen. Only two single carbon containing inclusions were observed in these samples. These seemed to be more resistant to the preparation method, while the nitrogen containing particles often appeared to be partly removed, see Figure 6•16 b), the needle particle.

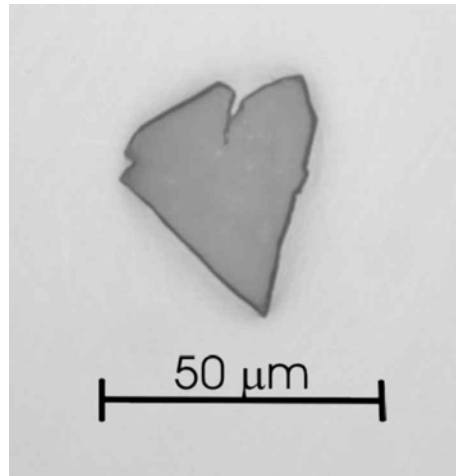

Figure 6•15: Inclusion found in top-cut, silicon and carbon signal by EDS-analysis,. LOM-image.

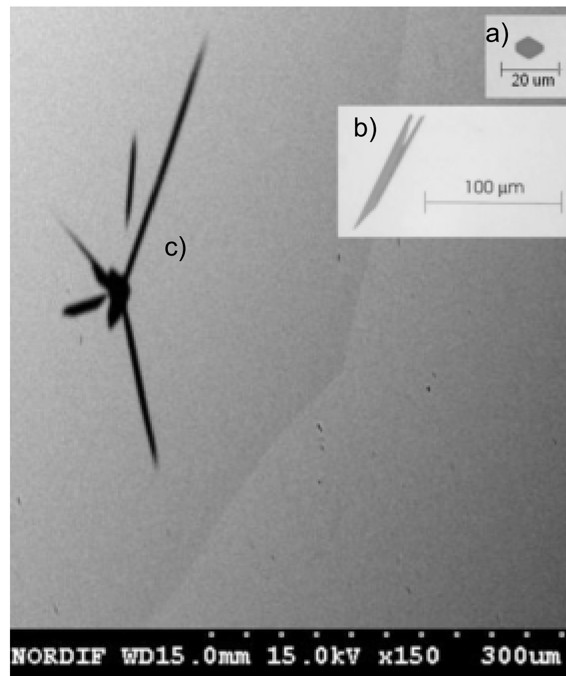

Figure 6•16: Inclusions in top right corner, a) and b) found in top-cut, inclusion cluster to the left, c), found in wafer ~ 5cm from the top. All inclusions consist of silicon and nitrogen, EDS-analysis. SEM-image.

There are only two known phases that consist of silicon and carbon and silicon and nitrogen, respectively, these are SiC and Si_3N_4. The particles found in these samples are therefore considered to be SiC and Si_3N_4. However, there are two different modification of each of these phases, the determination of which phase-modification these particles represent is treated in the section 6•3•5.

6•3•2 Dissolution experiments

Since the mechanically polished samples only revealed a few inclusions, and the inclusions are only seen as a section, we wanted to try another method to investigate the inclusions. We decided to try dissolution, since this permitted to study a large volume of silicon, and if we were able to retrieve inclusions by this method it would reveal the entire inclusion (not only a section). Various samples from the experiments (mainly MS-Exp1 and MS-Exp 3) were analysed, both wafers and top-cuts. Most of the studied top-cuts were in the form of lumps, but two were in the form of wafer sections, large area (15x15 cm^2), and 2-3 mm thick. Parts of a side-cut was also analysed. In Tables 6•10 and 6•12 the results of dissolution of wafers and top-cut samples from MS-Exp 1 are presented. Table 6•11 shows the results of wafers and top-cut samples from mainly MS-Exp 3. The weight employed was an analytical weight BP 210 S (±0.1 mg). The final mass, and thus also the mass% of inclusions, given in the tables are accompanied by some loss during the filtration process, and especially when removing the particles from the paper filter. Thus, they are only of an informative character and can not be considered as accurate values.

Table 6•10: Dissolution results for MS-Exp 1, wafers

Sample no.	From fraction solidified, fs	Mass dissolved / g	Volume dissolved / cm^3	Mass inclusions / g	Mass %
1	0.02	25.9835	11.2	not detectable	
2	0.12	31.7167	13.6	not detectable	
3	0.33	29.0418	12.5	not detectable	

Table 6•10: Dissolution results for MS-Exp 1, wafers

Sample no.	From fraction solidified, fs	Mass dissolved / g	Volume dissolved / cm^3	Mass inclusions / g	Mass %
4	0.40	21.1010	9.1	0.0043	0.02
5	0.59	20.7190	8.9	not detectable	
6	0.66	17.0135	7.3	not detectable	
7	0.90	23.3566	10.0	not detectable	

Table 6•11: Top-cut samples dissolution results for MS-Exp 1

Sample no.	Top-cut selection from block no.	Mass dissolved / g	Volume dissolved / cm^3	Mass inclusions / g	Mass %
8	10	14.8216	6.4	0.0328	0.22
9	10	20.7103	8.9	not detect-able	---
10	10	20.8106	8.9	not detect-able	---
11	10	18.2451	7.8	not detect-able	---
12	13	16.5580	7.1	not detect-able	---

Table 6•12: Dissolution results from top-cut samples, wafers and a side-cut sample (mainly from MS-Exp 3)

Sample no.	Type	Mass dissolved / g	Volume dissolved /cm3	Mass inclusions / g	Mass %
13	Side-cut	13.6613	5.9	0.0473	0.35
14	Top-cut[1] (MS-Exp 3,block 13)	15.0138	6.4	0.2790	1.86
15	Top-cut[1] (MS-Exp 3, block 10)	12.8024	5.5	0.2067	1.61
16	Wafer (MS-Exp 3, f_s = 0.02)	16.5339	7.1	not detectable	---
17	Wafer (MS-Exp 3, fs = 0.48)	13.1377	5.6	not detectable	---
18	Wafer (MS-Exp 2, fs = 0.84)	16.4557	7.1	not detectable	---
19	Wafer (MS-Exp 3, fs = 0.64)	14.1423	6.1	not detectable	---

1. Upper 2-3 mm

We see that only one wafer sample gave a measurable inclusion content by the dissolution method. This was the wafer with the highest substitutional carbon content (Figure 6•11) from MS-Exp 1. In order to see if this was a general trend wafers with maximum substitutional carbon contents from MS-Exp 2 and MS-Exp 3 were therefore also dissolved. However, these two wafers gave no inclusion content by this method. Furthermore, the top-cut samples did not systematically result in measurable amounts of inclusions.

Figures 6•17 to 6•23 show inclusions extracted by dissolution. The inclusion in Figure 6•17 (a) is a silicon carbide particle. It has probably grown on the crucible wall as there are traces of oxygen on the right side of the particle. The inclusions in (b) is silicon nitride to the left, high aspect ratio (needle shaped) and the smaller inclusion on the right side is silicon carbide.

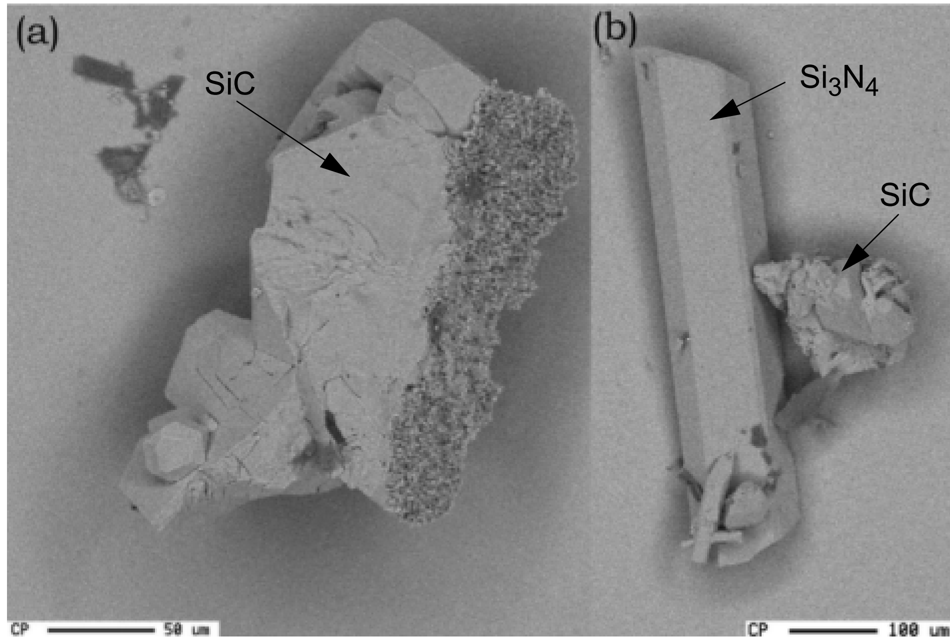

Figure 6•17: Inclusions in top-cut: (a) SiC-particle with traces of SiO_2 on the right side (sample 8). b) Needle-like particle on the left: Si_3N_4 and the smaller and rounder particle on the right SiC (sample 8). See Table 6•11 for sample information. EPMA-image

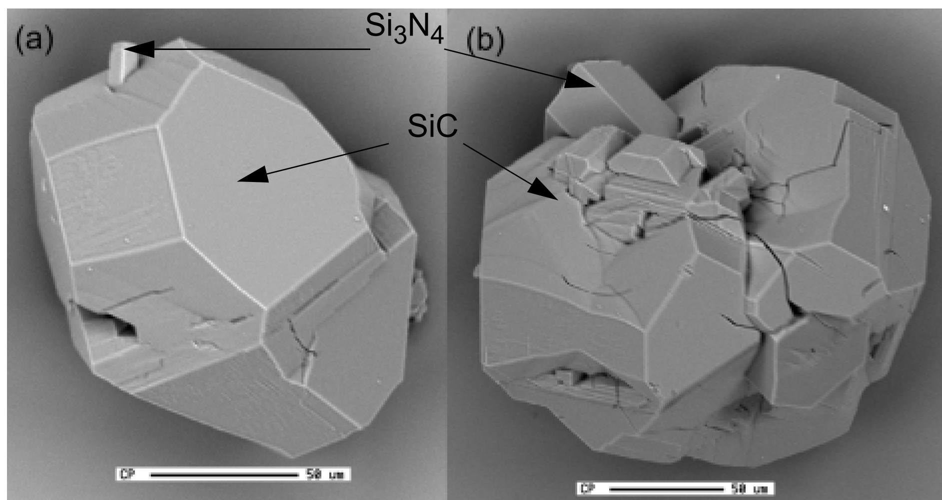

Figure 6•18: Inclusions in wafer: (a) SiC-particle, sticking out on top Si_3N_4 particle (sample 4), b) SiC-particle, sticking out on top Si_3N_4-particle (sample 4). See Table 6•10 for sample information. EPMA-image

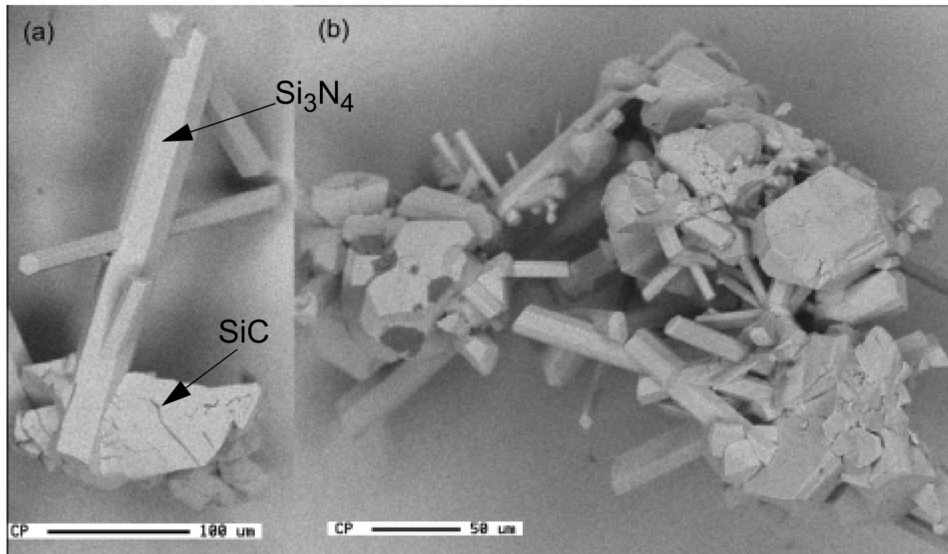

Figure 6•19: Inclusion in top-cut: (a) SiC growth on Si_3N_4 particle (sample 8) (b) Clusters of SiC and Si_3N_4 particles. See Table 6•11 for sample information. EPMA-image.

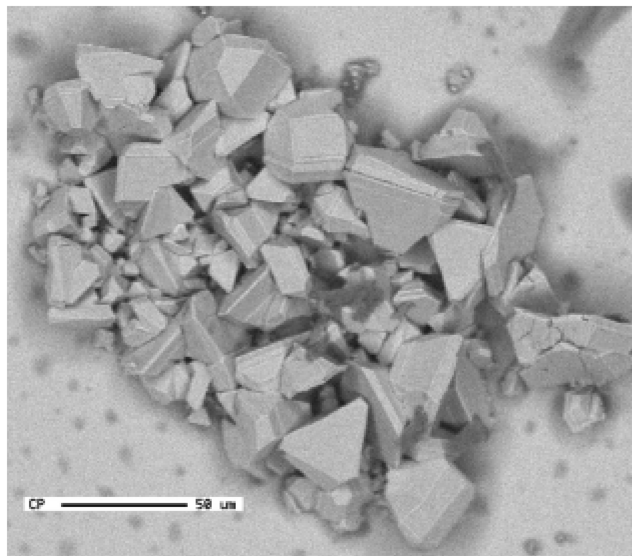

Figure 6•20: Inclusions from top-cut : Agglomerate of silicon carbide particles (sample 8). See Table 6•11 for sample information. EPMA-image.

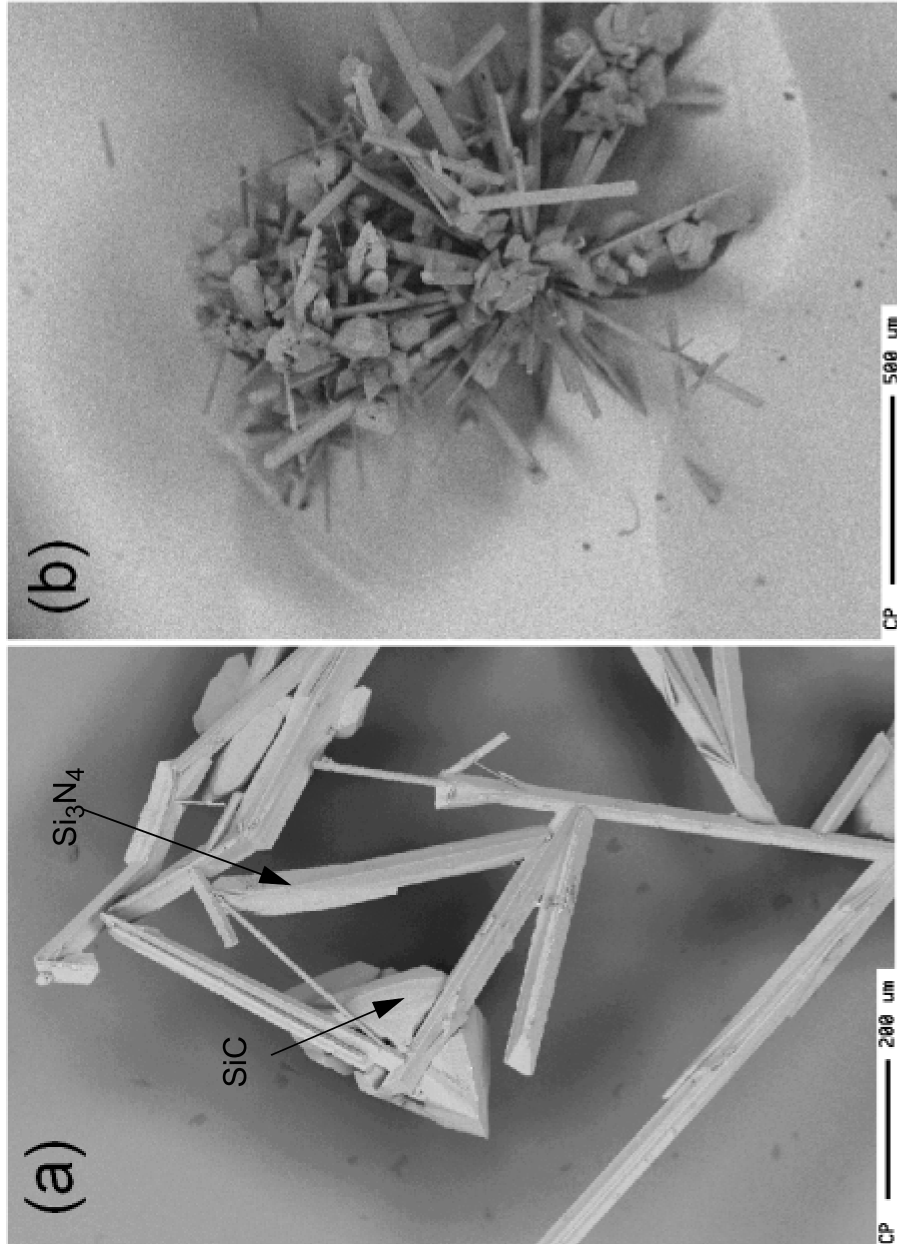

Figure 6•21: Inclusions in top-cut (a) and side-cut (b) : (a) Typical Si_3N_4-network with some SiC-growth in (sample 14), (b) cluster of Si_3N_4- and SiC-particles sticking out from a semi-etched sample in (b) (sample 13). See Table 6•12 for sample information. EPMA-image.

6•3•3 Inclusions in filter paper and in chemical-mechanical polished samples

Since a large number of the samples from the dissolution experiments did not give any measurable inclusion content by weight, and it was probable that some of these samples could contain inclusions, some of the filter papers were analysed by EPMA. These were filter papers where no weight change could be observed and that contained no visible particles.

Analysis of these filter papers revealed a few particles within the fibres of the filter paper. In sample 16, bottom wafer from MS-Exp 3, only silicon nitride particles were found, see Figure 6•22 and 6•23. In 6•22 (a) we see a well shaped silicon nitride crystal where growth seem to develop along the c-axis. It has not yet developped the characteristic needle structure, indicating that we are at an early stage of the growth. The diametre of this particle is ~ 20 μm. As we can see from previous pictures of the silicon nitride particles, even if they are much longer the diametre of many of these are also ~ 20 μm, clearly indicating growth primarily along c-axis. In Figures 6•22 (b) and 6•23 (a) we possibly see the “start” of a silicon nitride network, several distinct silicon nitrides grow out from one particle. In this picture (b) we also see clearly, from the particle pointing out from the picture, the hexagonal cross section distinctive for these particles. In Figure 6•23 (b), which is from a wafer sample from the middle of the block ($f_s = 0.48$), we see a silicon carbide particle. As previously seen in pictures of silicon carbide, these often have voids and channels included in the crystal structure.

Wafers from the same sections as sample 16 and 17 (used in for dissolution) were polished by use of a chemical-mechanical polishing technique. These results are shown in Figure 6•24 containing also typical EDS-spectra. In the bottom wafer (same section as sample 16) a high density of silicon nitride particles was found, most of them were partly removed by the polishing, see Figure 6•24 (a). In the middle-wafer (same section as sample 17, $f_s = 0.48$), some silicon nitrides and silicon carbides were found, but not with the same high particle density as in the bottom wafer, see Figure 6•24 (b) and (c).

The results from the polished wafer samples seem to correlate well with the analysis of the filter papers; small silicon nitride particles were found in the bottom wafer, while in the middle-wafer ($f_s = 0.48$) both silicon nitride and silicon carbide particles were found. Also a polished sample from MS-Exp 2 from the lowest f_s revealed only silicon nitride particles, but the particle density was lower here than in the sample from MS-Exp 3.

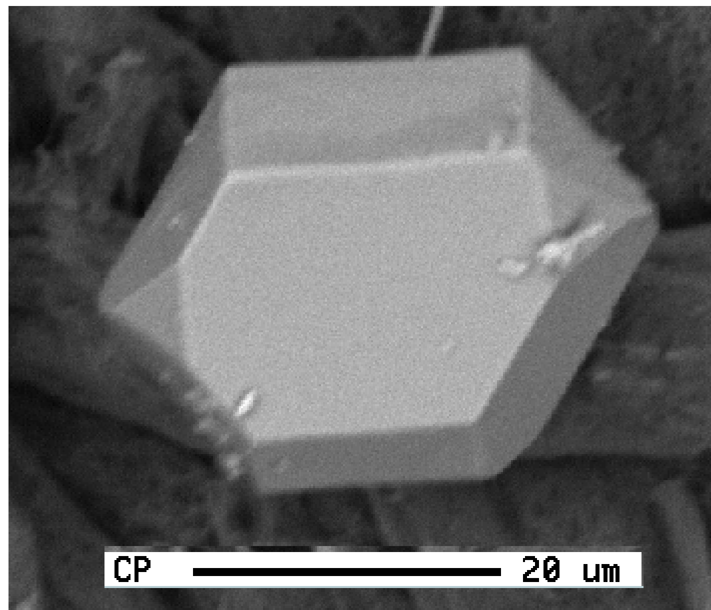

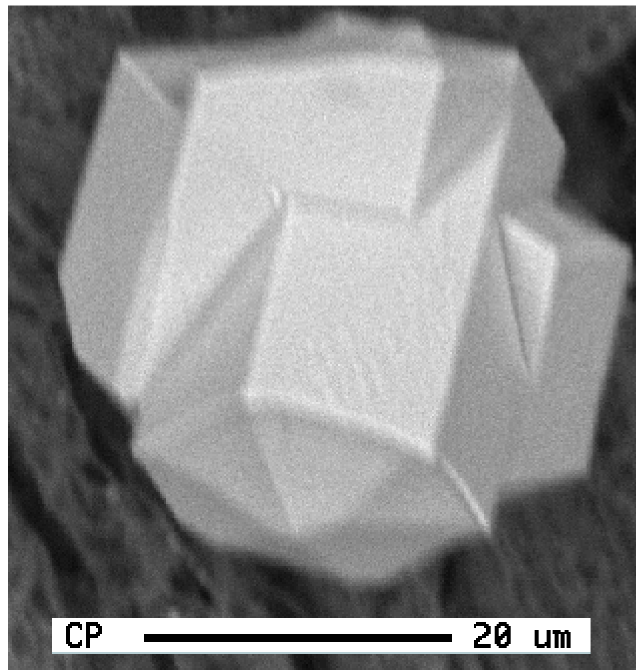

Figure 6•22: Particles found in filter paper; (a) Silicon nitride particle (sample 16), (b) start of silicon nitride network (sample 16). SEM-image.

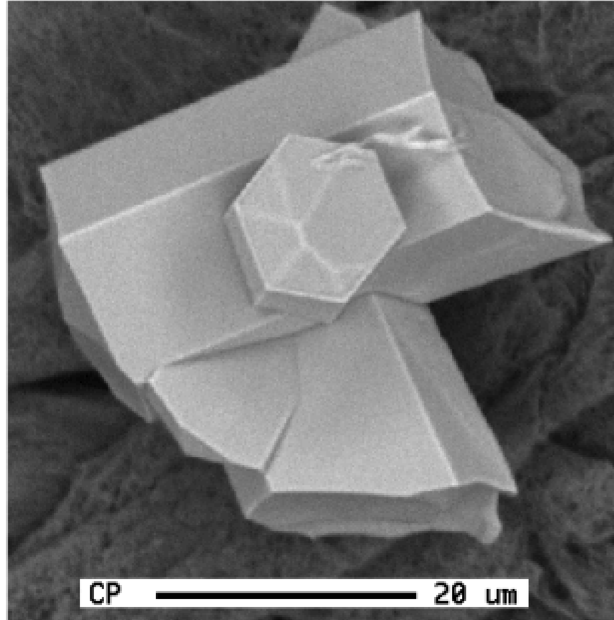

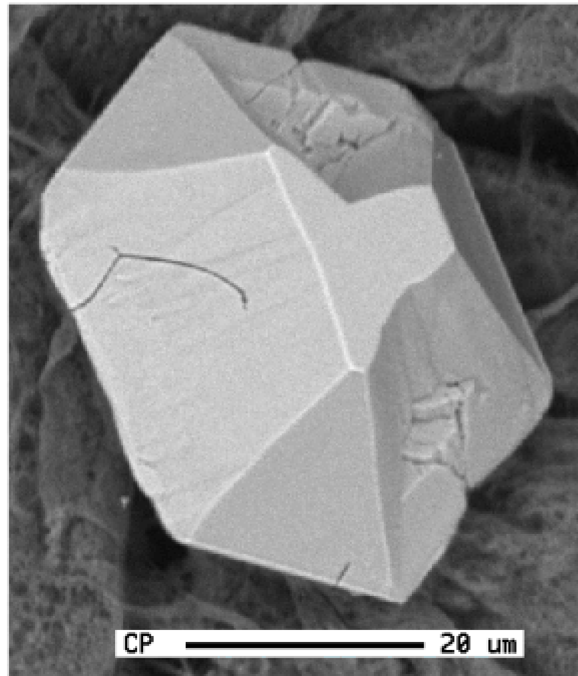

Figure 6•23: Particles found in filter paper (a) Silicon nitride particle (sample 16) (b) Silicon carbide particle (sample 17). SEM-image.

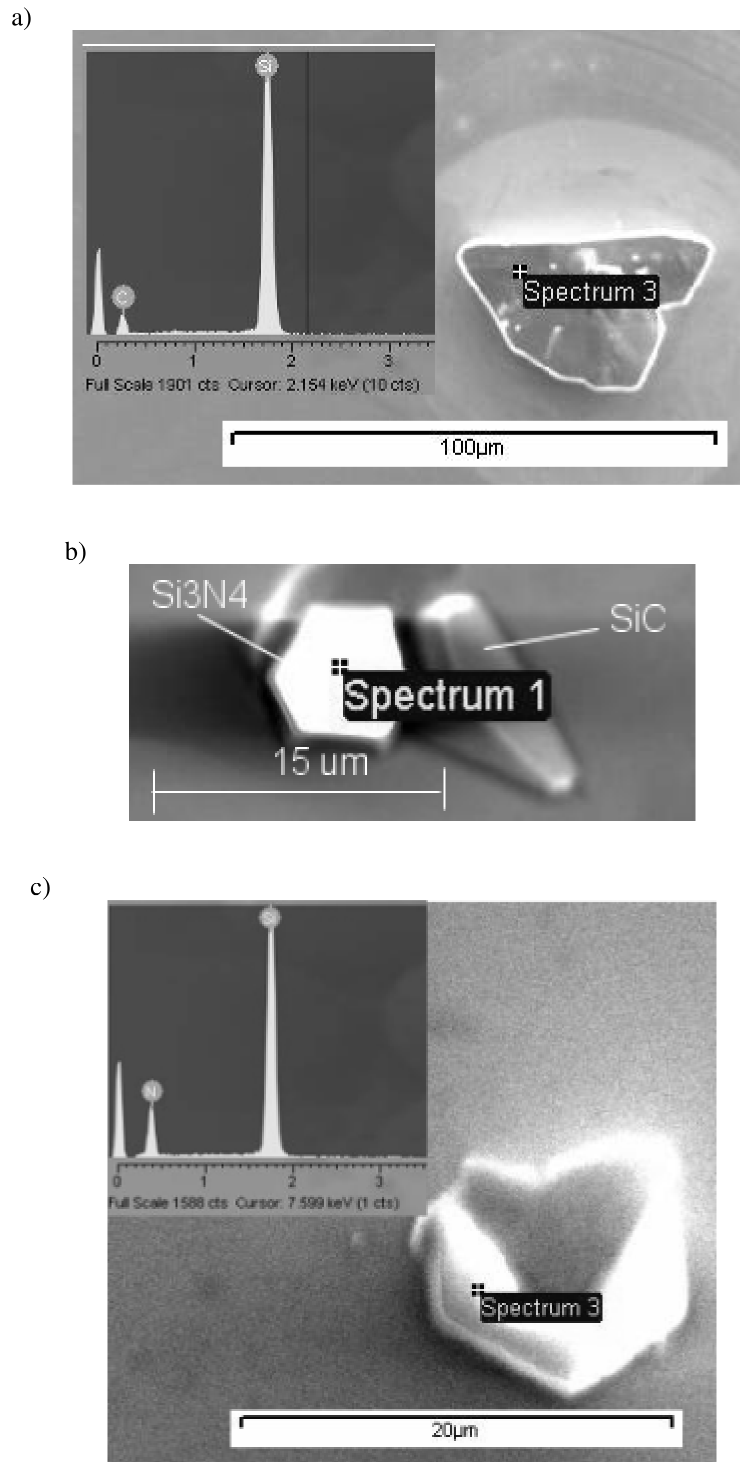

Figure 6•24: Particles on the surface of chemically-mechanically polished wafers. In (a) silicon carbide particle (sample 17), (b) silicon nitride and silicon carbide particle (sample 17) and in (c) silicon nitride particle (sample16)

6•3•4 Summary on dissolution experiments

These experiments revealed large inclusions and clusters in the top-cut samples, whereas most wafer samples (bulk) gave no inclusion content by this method. Smaller inclusions were, however, observed in filter papers from wafer dissolution and chemical-mechanical polishing. Indicating that the wafer samples can contain smaller inclusions even though no weight change was observed after dissolution.

The dissolution technique proved effective for extracting larger inclusions. It permitted to study larger volumes with respect to inclusions. Another important advantage is that it gives information on the shape and appearance of the inclusions. The limitation of the technique as used here is with regard to smaller inclusions (< 20 μm). It is a risc that smaller silicon nitride inclusions may dissolve during the long etching periods. In Figure 6•23 a) one can see an inclusion that seems to have been attacked by the etching solution. The dissolution technique has not been optimised in this work due to limitations in time and resources.

6•3•5 Identification of phase modification

As mentioned in 2·2 and 2·3 both silicon carbide and silicon nitride exist in two different modifications, the α- and β phases. In order to identify the phase modification of the particles EBSD-patterns were collected for various particles stemming from different experiments. By use of a software the patterns were indexed and recognised as one phase modification. For both type of particles the β-modification gave a complete match.

This result is in good agreement with previous work. The β-silicon nitride phase has often been observed to appear as hexagonal needles [f.in. Jennings, 1983 and Inomata and Yamane, 1974]. For silicon carbide the β-phase is the thermodynamically stable one, as seen in Figure 2·1.

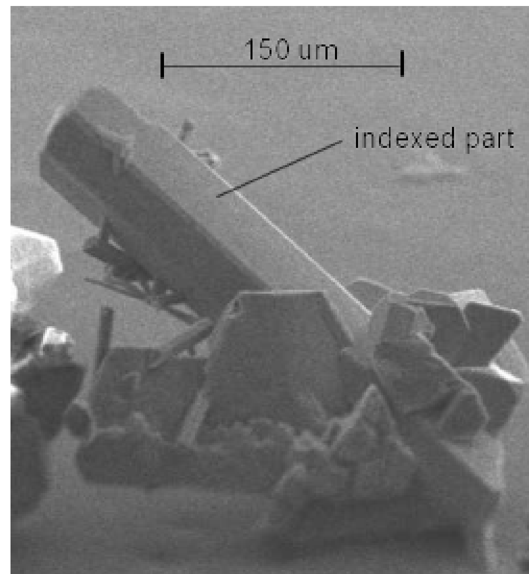

Figure 6•25: Example of tdilted Si_3N_4-particle used in EBSD-analysis

a)

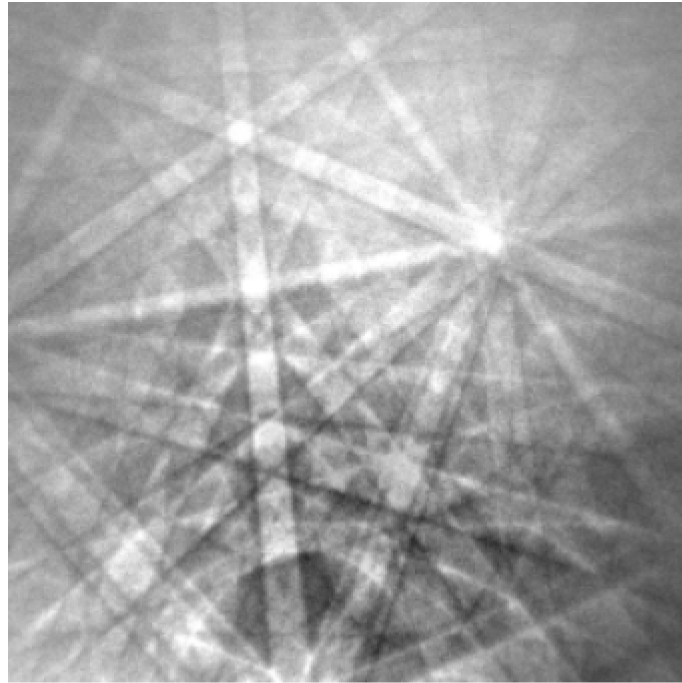

b)

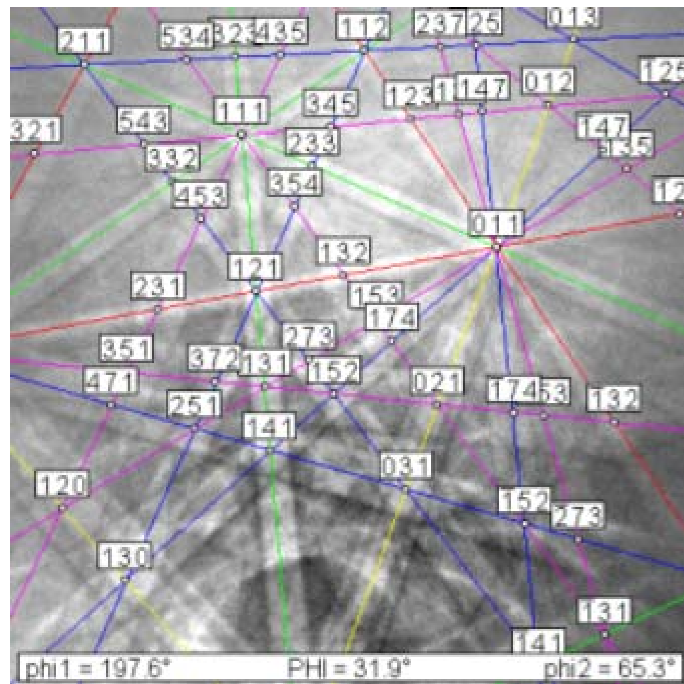

Figure 6•26: (a) EBSD-pattern of a silicon carbide particle and in (b) to the right the corresponding indexing of the the pattern; the phase was identified as the β--phase.

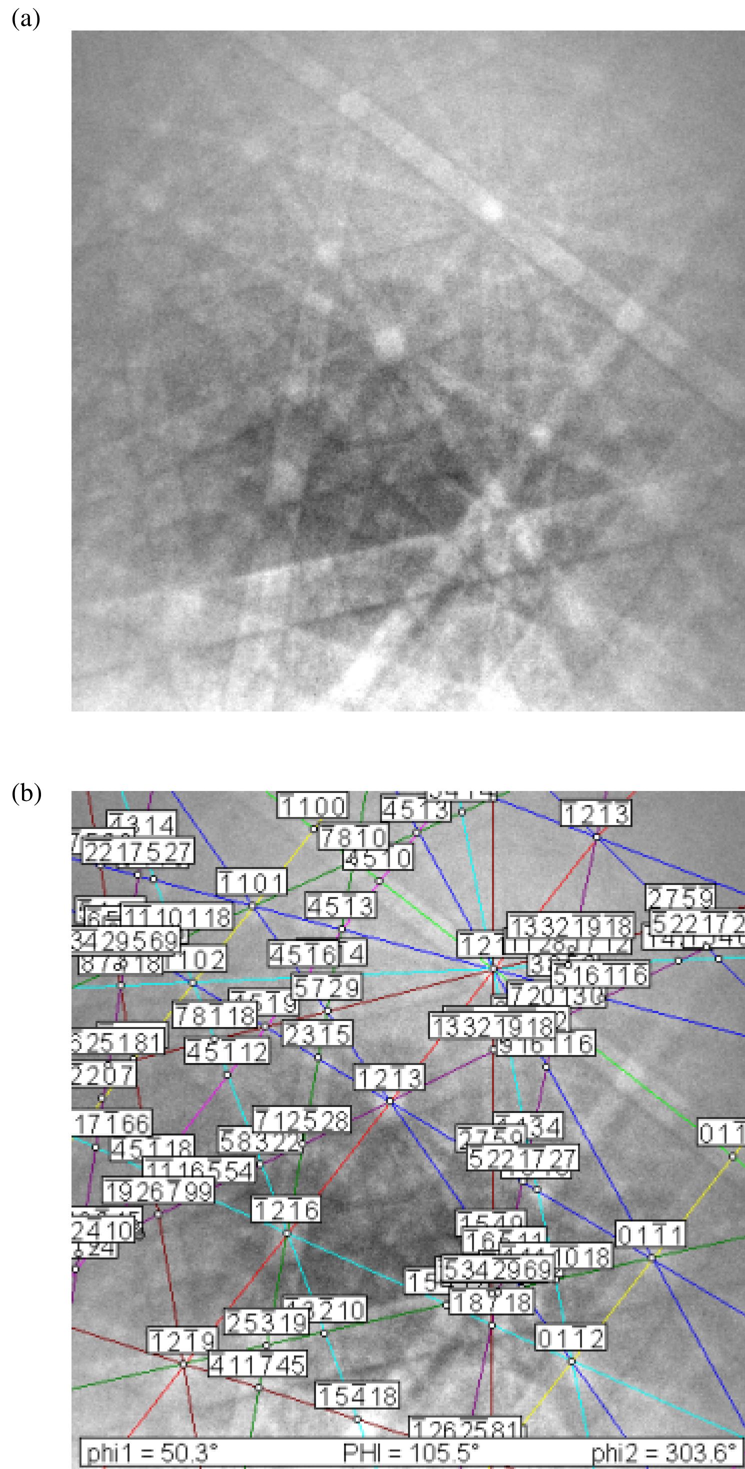

Figure 6•27: (a) EBSD-pattern of a silicon nitride particle, and in (b) the corresponding indexing of the the pattern; the phase was identified as the β--phase.

6•3•6 Cumulative particle size distribution

Some of the dissolved top-cut samples and the side-cut sample contained enough inclusions that a particle size distribution could be measured by the laser diffraction technique described in section 4.7.3.

In the top-cuts from MS-Exp 3, particles or probably clusters up to a size of 1800 μm was measured. The largest portion, 80-90 mass%, lies between 100-1000 μm for these two top-cuts. For the top-cut from MS-Exp 1, 80 mass% lies between 75-385 μm. Also for the side-cut the size of the particles/clusters is smaller than in MS-Exp 3, almost 90 mass% lies between 100-400 μm.

How precise the laser diffraction technique is for our samples that consist of different shaped particles has however not been tested. When comparing with SEM- and EPMA-pictures, the cumulative particle size distribution seem to give at least a rough estimate of the size distribution. It can be questionned if it measures the “true” size of for instance clusters .

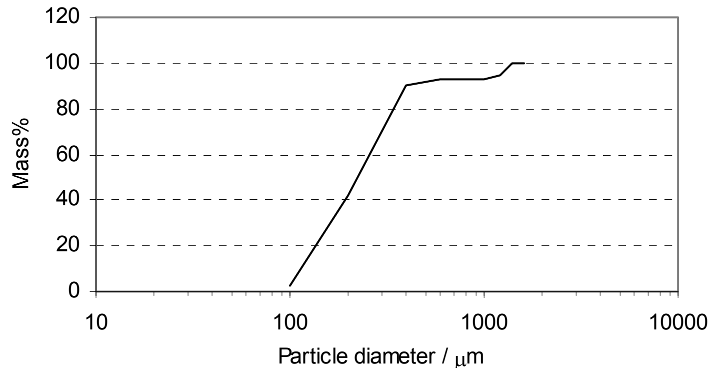

Figure 6•28: Cumulative particle size distribution for side-cut as measured by laser diffraction (Coulter).

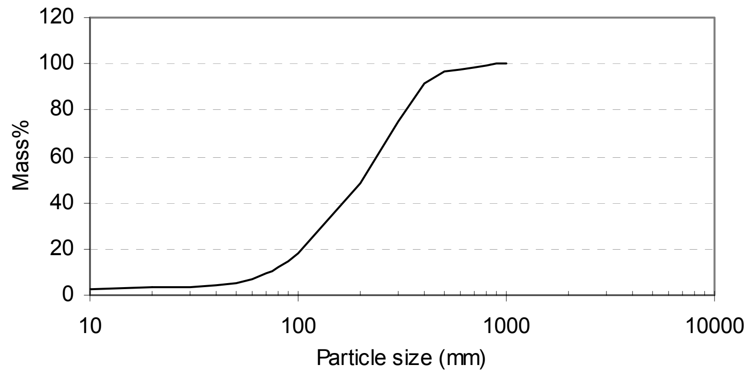

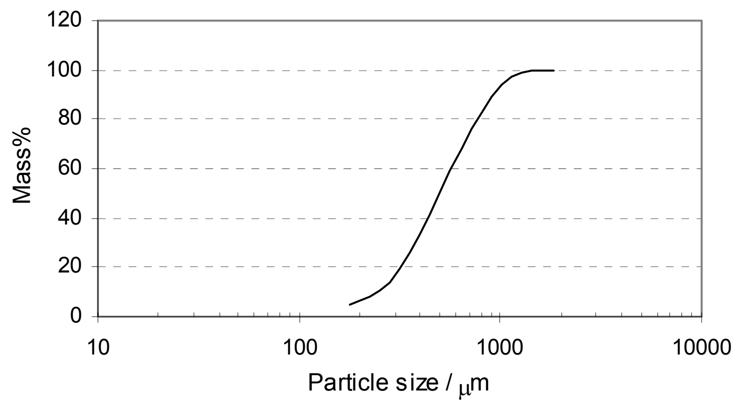

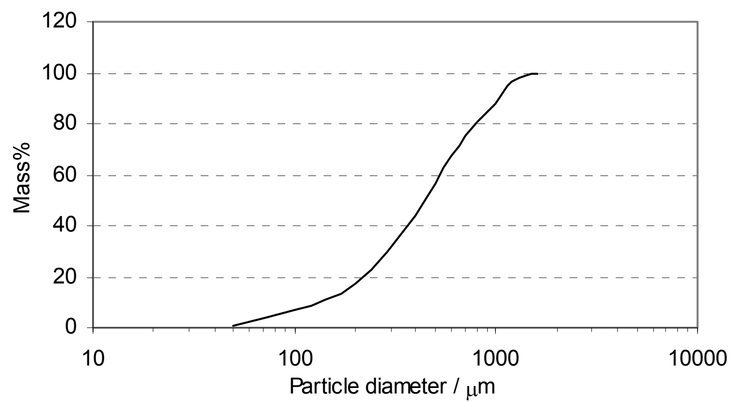

Figure 6•29: Cumulative particle size distribution for (a) Top-cut MS-Exp 1Block 10 (middle), (b) Upper part of top-cut MS-Exp 3 Block 10 (middle) and (c) Upper part of top-cut MS-Exp 3 Block 13 (corner)

REFERENCES

Acciarri M., S.Binetti, S.Ratti, C.Savigni, S.Pizzini, F.Ferrazza and D.Margadonna (1995), *Study and conditioning of defected areas in eurosil multicrystalline silicon, 13th European Photovoltaic Solar Energy Conference*, 1336-1339

Geerligs L.J. (2002), *mc-Si: relation between ingot quality and cell efficiency*, 12th NREL Workshop on Crystalline Silicon Solar Cells, Materials and Processes

Inomata Y. and T.Yamane (1974), *β-Si_3N_4 single crystals grown from Si melts*, J.Cryst.Growth 21, 317-318

Jennings H.M., *Review On reactions between silicon and nitrogen*, J.of Mat.Sci. 18, 951-967, 1983

Chapter 7 Discussion

There are several topics that can be discussed from the results, I have selected a few that I would like to emphasize: silicon nitride formation, silicon carbide formation, the pushing mechanism. The low life-time dip and the carbon solubility are briefly discussed. An estimate of the temperature gradient in the melt, that is $(T_s-T_m)/h$, is given.

7•1 Silicon nitride formation

The results showed that there is a significant formation of silicon nitride during the solidification. This means that there must be a high content of nitrogen in the melt, as was also measured in the melt samples. We will therefore discuss the sources to nitrogen in the melt, and the formation mechanism in the following text. As there is few published works discussing silicon nitride formation in similar solidification systems, this part tries to point out possible mechanisms which are partly based on hypotheses and partly on the experimental results.

7•1•1 Sources to nitrogen in the melt

Besides recycled material containing inclusions there are two sources to nitrogen in this system; a) the atmosphere and b) the crucible coating, the two areas in contact with the melt.

a) For a reaction with nitrogen at the melt surface a certain gas leakage into the system is necessary. The calculated equilibrium pressure for reaction 7•1 is $1.25x10^{-3}$ bar at T = 1693 K (1420 °C).

$$3Si_{(l)} + 2N_{2(g)} = Si_3N_{4(s)} \qquad 7•1$$

$$\Delta G^0_{7.1} = -874 + 0.405 \times T(\text{kJ/mol})$$

Jennings *et al.* [1983] references therein,
(data obtained for formation of both α and β)

This represents an air-leakage pressure of ~1.6x10^{-3} bar. We can then calculate the air leakage velocity necessary to produce this pressure in the furnace employing as an example a total pressure 0.6 bar and a flow rate of 100 Nl/min.

Air-leakage velocity (pV) necessary to produce an air pressure of 1.6x10^{-3} atm:

$p = 1.6 \times 10^{-3}\text{atm} \qquad V(STP) = 100\text{Nl/min}$

$V(\text{at 1000 K, ptot 0.6 bar}) = 10dm^3/s$

$$pV = 10dm^3/s \times 1.6 \times 10^{-3}atm = 1.6 \times 10^{-2}dm^3atm/s = 15mbar \times l/s \qquad \text{eq•7•1}$$

In industry the air-leakage velocity is measured prior to furnace start, that is at ~room-temperature. The maximum accepted air-leakage velocity at room-temperature for furnace run is 1.5 mbar l/s. Therefore the air leakage at 1000 K is then 1.5x 1000/298 = 5 mbar l/s.

The estimated value for the maximum air-leakage velocity at 1000 K is significantly lower than the air-leakage velocity necessary to produce the equilibrium nitrogen pressure of 1.25x10^{-3} bar. Moreover, the nitrogen reaching the surface of the melt will be further reduced because of the transport through the gas-boundary layer, since the gas-transfer coefficient is inversely proportional to the total pressure in the chamber, see 7•2•1. We therefore consider that **nitrogen in the melt is not caused by air leakage**, but from the silicon nitride coating.

b) The coating represents a large surface area (particle size < 1μm) that is in contact with the melt. The dissolution reaction for the coating may be described in terms of the two following reactions with linearized relations for the Gibb's energy difference;

$$Si_3N_{4(s)} = 3Si_{(l)} + 2N_{2(g)} \qquad 7•2$$

$$\Delta G^0(7{\cdot}2) = 874 - 0.405 \times T(\text{kJ/mol})$$ eq•7•2

From Jennings *et al.*[1983]

$$1/2\ N_{2(g)} = \underline{N}$$ 7•3

$$\Delta G^0(7{\cdot}3) = -44.5 + 0.0664 \times T(\text{kJ/mol})$$ eq•7•3

From Iguchi and Narushima [1993]

Dissolution reaction:

$$Si_3N_{4(s)} = 3Si_{(l)} + 4\underline{N}$$ 7•4

$$\Delta G^0(7{\cdot}4) = (\Delta G^0(7{\cdot}4) + 4 \times \Delta G^0(7{\cdot}3)) = 696 - 0.1394 \times T(\text{kJ/mol})$$ eq•7•4

The Van't Hoff equation can be expressed as: ,

$$\frac{d\ln K}{d(1/T)} = -\frac{\Delta H^0}{R}$$ eq•7•5

where K is the equilibrium constant, ΔH^0 is the enthalpy change and R is the gas constant. For the dissolution reaction above the enthalpy change is positive (taking ΔH^0 = 696 kJ/mol). When the temperature increases a positive enthalpy change favours the formation of products (K increases with T), as can be seen from the Van't Hoff equation. Therefore according to literature data for reactions 7•2 and 7•3, the solubility of nitrogen in liquid silicon equilibrated with Si_3N_4 should increase with increasing temperature, which was also observed by Iguchi and Narushima [1993] in their study of the nitrogen solubility in liquid silicon.

7•1•2 Nitrogen contents in the melt- comment on the nitrogen solubility

In Table 6·7 we saw that the nitrogen contents decreased with increasing f_s. The surface temperature of the melt also decreases with increasing f_s. One can assume from the melt-sampling measurements that the melt is at the solubility limit already at crystallisation start. This is also supported by the observation of silicon nitride inclusions at an early

stage in the crystallisation (at low f_s). The surface temperature of the melt decreases as the growth proceeds, that is T decreases with increasing f_s, see temperature profiles for the melt sampling runs. Since the ΔH for the dissolution reaction (7·4) is positive the solubility of nitrogen in equilibrium with silicon nitride will decrease with decreasing temperature. Which means that as the solidification proceeds the nitrogen content in the melt should decrease. Therefore, the observed decrease in nitrogen content for the melt samples with decrease in temperature supports the assumption that the melt is saturated with nitrogen already at $f_s = 0$.

Since there is a large scatter in the data for the nitrogen solubility (see Table 2·3) it is interesting to plot our nitrogen data against temperature and extrapolate to the melting point of silicon. Figure 7•1 shows the relation that is obtained between the nitrogen content and the temperature.

.

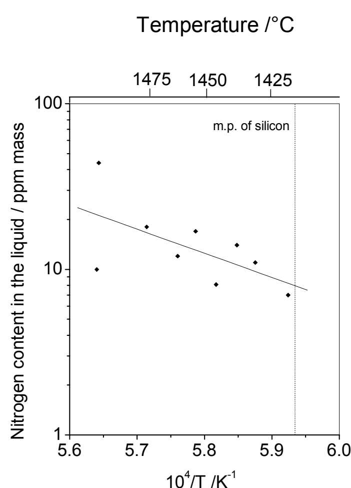

Figure 7•1: Nitrogen contents in selected melt samples as a function of temperature, from Table 6·7.

The extrapolated value we obtain for the nitrogen content in silicon at its melting point is 8 ppm mass.

There is of course a large uncertainty in the temperature at which our samples were taken, see section 6·1. Nevertheless, the nitrogen content extrapolated to the melting point

of silicon obtained from our data is in fairly good agreement with the solubility from Iguchi and Narushima [1993], which was 4 ppm by mass. Especially when comparing with the values reported by Kaiser and Thurmond [1959] and Yatsurugi *et al.* [1973], which were 100 and 60 ppm by mass, respectively. These results support therefore the solubility obtained by Iguchi and Narushima [1993].

7•1•3 Silicon nitride inclusions

The silicon nitride inclusions in this study have been identified as the β-modification of the phase, whereas the coating consists mainly of the α-phase. This leads to the conclusion that we are dealing with a dissolution-precipitation mechanism. There is also consensus in the literature that the β-phase is the one that forms in liquid silicon supersaturated with nitrogen [f.in. Jennings, 1983, Mukerji and Biswas, 1981, Inomata and Yaname, 1974 and Kaiser and Thurmond, 1959]. Furthermore, the nitrogen contents from the melt as a function of approximate sample temperature indicate that it is saturated with nitrogen prior to crystallisation start.

The melt becomes then hypereutectic when the crystallisation starts, resulting in the formation of primary crystals of silicon nitride. The silicon nitrides grow as faceted crystals, where the crystal shape is bounded by the slowest growing faces. They also appear in a large range of size (10-20 μm up to ~1500 μm in top-cuts). This means that they are formed and grow in the melt, some melt samples also contained silicon nitride inclusions, see section 6·1·7.

The nucleation is probably heterogeneous as this nucleation type has a smaller energy barriere than homogeneous nucleation, and the latter type of nucleation has been reported to be difficult for this system [Jennings, 1983 and Kaiser and Thurmond, 1959]. Actual nucleation sites are crucible walls and for particles formed in the bulk melt they are possibly detached crucible particles. The result is then silicon nitride particles growing from the crucible walls/bottom and silicon nitride particles growing in the melt. Particles growing on the wall are frequently observed by the industry, they appear in high concentration in side-cuts [Personal communications, P.C.Hjemås and F.Hugo at ScanWafer ASA].

When the crystallisation starts the supersaturation will be at the highest, both since the temperature drop is the most significant and because of the high temperature in the holding period giving a high content of dissolved nitrogen. Since the supersaturation is high it is probable that it will lead to the nucleation of many silicon nitride particles. Nucleation is dependent on the degree of supersaturation in a system, whereas growth is less dependant on the supersaturation, so it is expected that growth of particles will dominate in the later stages of the process, when the supersaturation is lower. Silicon nitride particles at the bottom that are “loose”, not adhering to the coating may act as nucleation sites for the precipitation. Providing thus heterogeneous nucleation sites. Coating particles are also susceptible to being ripped off the walls during the process, especially during melt-down when material slides down in the crucible. The coating may also scale off [Personal Communication F.Hugo at ScanWafer ASA]. There is therefore a high probability of coating particles in the melt.These particles may then be pushed (as discussed in 7•4) and grow in the melt until they are engulfed. It could be interesting to measure the content of such loose particles at the bottom of the crucibles prior to loading them with silicon, that is taking an imprint of the bottom.

Silicon nitrides growing in the melt has recently also been reported by Hejjo Al Rifai *et al.* [2004] who studied two solar cells from a region close to the top of an ingot. They observed two different types of particles, one type is fibre- like growing in bundles with diameter < 1 micron, and the other type was thick monocrystalline silicon nitride rods. The second type of particle is similar to the one we have observed in our study. We have, however, not observed the first type in our study (SEM and LOM). The dissolution method is probably too rough to retrieve this type of filament, since they are so thin. However, they were not observed in the microscopic studies of polished samples either. These filament-like particles were also observed by Lawerenz *et al.* [2003] who studied the upper part of an ingot produced by Deutsche Solar AG. He suggested that they grew from the melt, but at the liquid-solid interface. This is not what Hejjo Al Rifai *et al.* [2004] suggest: that they grow in the melt and get trapped in the material when they fall down to the bottom of the melt due to their higher density. However, since these filament-like particles are different in both shape and appearance from the crystal-type particles, it seems likely that there can be different growth mechanisms for the two types of particles.

The investigated material of Hejjo Al Rifai *et al.* [2004] was from yet a different manufacturer of multi-crystalline silicon. The precipitation of silicon nitrides during crystallisation of multi-crystalline silicon ingots therefore seems to be a rather general phenomenon, but there may be different formation mechanisms.

7•1•4 Effect of the coating on the silicon nitride formation

The wetting ability of the coating defines the contact area with the melt. Wetting is defined by the contact angle of a droplet with the substrate. Measured contact angles of silicon with silicon nitride from literature are summarized in Table 7•1.The contact angle can be expressed by the Young equation:

$$\frac{(\sigma_{sg} - \sigma_{sl})}{\sigma_{lg}} = \cos\theta \qquad \text{eq•7•6}$$

where σ_{sg} is the interfacial energy solid-gas, σ_{sl} is the interfacial energy solid-liquid and σ_{lg} the interfacial energy liquid-gas.

Table 7•1: Contact angle of silicon with silicon nitride, from literature

Contact angle	Reference
90°	Mukai and Yuan [2000]
55°	Duffy *et al.* [1980]
0-134°	Li and Hausner [1992]
> 10°	Cröll *et al.* [2003]

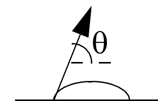

There is a large scatter in the measurements of contact angle, ranging from poor to good wetting ability. Li and Hausner [1992] explained this variation in contact angle by the degree of oxydation of the silicon nitride coating forming oxynitride SiO_xN_y. The oxynitride will alter the σ_{sg} and σ_{sl} values of eq. 7•9, resulting in a different contact angle. According to Li and Hausner [1992] and Cröll *et al.* [2003] the oxynitride gives a poor wetting, whereas the silicon nitride gives good wetting.

A contamination of the Si_3N_4 surface by oxygen can be expected already at low oxygen partial pressures [Li and Hausner, 1992]. As the coating in industry is exposed to

air, one can therefore assume that it contains some oxygen. Thus, resulting in an initially poor wetting. The oxygen layer may decompose at high temperature or in contact with the melt, increasing thus the wetting.

Even though the wetting may be poor, since the solubility is low, the contact area with the melt does not necessarily need to be high to obtain a nitrogen saturated melt. What could increase the dissolution rate would be if particles are loose (f.inst. at the crucible bottom) in the melt, both convection and a larger contact area available would then facilitate the dissolution. In addition the coating particles are small and thus the surface area is large.

Calculation of the amount of coating particles necessary to produce a nitrogen saturated melt prior to the crystallisation :

The relation for solubility as a function of temperature derived by Iguchi and Narushima [1993] is given in eq 7•7.

$$\log(N mass\%) = 2.410 - \frac{9759}{T} \quad \text{eq•7•7}$$

Using this relation we obtain the solubility at temperature of the melt just prior to crystallisation start, at ~1500 °C, is 8 ppm mass. As the melt quantity is 265 kg. This means that the amount of nitrogen is 2.12 g, which is 0.15 moles. One mole of Si_3N_4 dissolving gives 4 moles of nitrogen.

Therefore the quantity of coating particles becomes :
(0.15 moles/4) x M (Si_3N_4)= 0.0378 moles x140.31g/mole = 5.3 g.

The quantity of coating employed per crucible is ~ 300 g, the amount that “needs” to dissolve represents only 0.018 (~2%) parts of the total coating amount.

α-β phase transformation:

Another factor that might have a considerable effect on the silicon nitride formation could be the phase modification of the coating. The actual coating consists mainly of the α-phase. The α-phase transforms irreversibly into the β-phase at high temperature [Meléndez-Martínez and Domínguez-Rodríguez, 2003]. This transformation takes place through a reconstructive process involving the breakage and construction of bonds. It is suggested that it takes place through a solution-precipitation mechanism, since it seems to occur only in the presence of a liquid phase. The α-phase will then dissolve and the β-phase precipitate. Jennings [1983] suggested that the α-phase forms from reaction with molecular nitrogen whereas the β-phase forms from reaction with atomic nitrogen. When Si_3N_4 dissolves the nitrogen present will be atomic, resulting thus in precipitation of the β-phase.

The free energy of the α-phase is slightly higher than the β-phase (~30 kJ/mol at 25 °C) after the calculations of Grün [1979]. As the coating is in contact with liquid silicon, which seems to be necessary for the formation of the β-phase, and this phase is slightly more stable than the α-phase, there is then a driving force for the formation of the β-phase in the system. How much of the α-phase that transforms into the β-phase may then be dependant on how fast the crystals grow in the melt. If such a mechanism exists it should be interesting to test a coating which consists mainly of the β-phase. This may reduce the precipitation of silicon nitride in the melt. Duffy *et al.* [1980] actually reported in their study of CVD-coatings that the β-Si_3N_4 seemed much more resistant to chemical attacks from molten silicon than α-Si_3N_4.

Coating adhering to silicon after crystallisation was examined by X-ray analysis. A similar diffractogram as for the analysis of loose coating particles (prior to run) was obtained, that is mainly α-phase present, only small quantities of the β-phase, see Appendix 2. This indicates that there is no phase transition occurring directly in the solid phase, and is thus in agreement with the above mentioned theory.

7•2 Silicon carbide formation

7•2•1 Carbon contents in the melt

Our measurements of the initial carbon concentration in the silicon melt, prior to solidification, range between 10-43 ppm mass, see 6·1. Since the temperature at this stage in the process is ~ 1500 °C, the initial carbon concentration for all the melt sampling experiments is well below the solubility limit for carbon in liquid silicon, see 2·2. These carbon concentrations are however much higher than a "pure" feedstock should give. Besides recycled material there may be contamination from (a) the gas phase (CO) and from (b) dust particles.

(a) Gas phase contamination

In section 2·3, CO-incorporation in the melt was discussed. A certain CO-content is expected in the furnace atmosphere due to reactions between silica and graphite and also SiO reacting with graphite. The following sketch for the incorporation of CO may be proposed:

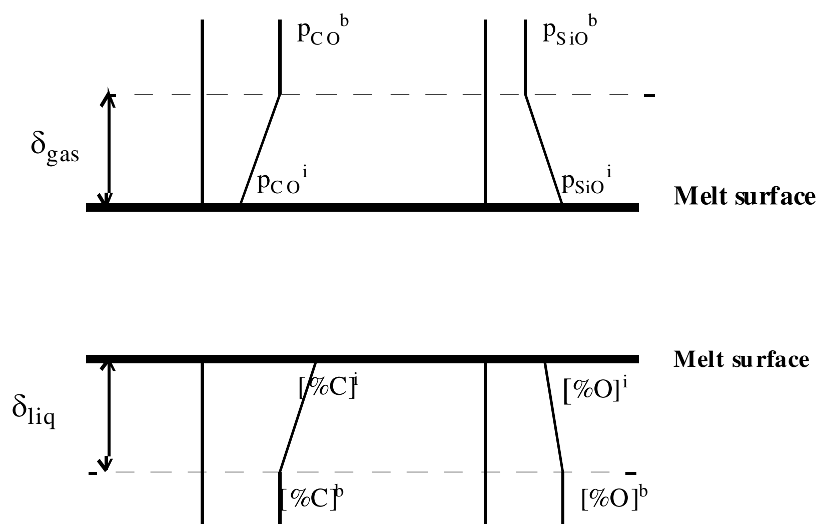

Figure 7•2: CO-incorporation scheme, assuming continually drive off of oxygen as SiO gas

From the sketch in Figure 7•2 we see that CO has to pass a gas-boundary layer before reaching the melt surface. Once dissolved in the melt there will be a liquid-boundary layer where the carbon concentration is higher than in the bulk. The mass-transfer coefficient for carbon in the melt be important for the transport of carbon to the bulk. The incorporation reaction when a CO-concentration exists in the ambient atmosphere can therefore be divided into three major steps:

1) Transport of CO through the gas-boundary layer
2) Reaction 2·4
3) Transport of carbon through the melt-boundary layer

The reaction at the surface where CO dissolves (see section 2·3·2) has a high equlilibrium constant ($K = 1.04x10^7$), and thus the thermodynamics represent no hindrance for the reaction to occur. Previous works have shown experimentally that the reaction with the melt does happen readily [Endo *et al.*, 1979, and Schmid *et al.*, 1979]. The reaction itself, once CO has reached the melt surface, is therefore not considered as a rate-determining step. The transport through the melt-boundary layer determined by the mass-transfer coefficient might be rate-determining. If this was the case, one would, however, expect the formation of a silicon carbide layer due to the high $[\%C]^i$ building up at the interface. Such a silicon carbide layer has not been observed in the four melt sampling experiments, nor when studying the top-cuts from the corresponding ingots.

The transport through the gas boundary layer can be described by:

$$\dot{n} = \frac{k_g}{R \times T}(p_{COb} - p_{COi}) \qquad \text{eq•7•8}$$

As seen from eq 7•8 the transport through the gas boundary layer depends on the partial pressure of CO in the chamber and the mass transfer coefficient for the gas phase. Therefore, we will look closer at the mass transfer coefficient for the gas phase. To estimate k_g we consider flow along a plate. We calculate k_g by use of the following equations [Engh, 1978].

$$Sh = \frac{k_g \times L}{D} \qquad \text{eq•7•9}$$

where L is plate length, *Sh* is Sherwoods number, *D* is the diffusion coefficient for the diffusing species.

where *Sh* , *Sc* and *Re* is Sherwoods, Schmidts and Reynolds number, respectively, these are given as:

$$Sh = 0.68 \times Sc^{1/3} \times Re^{1/2} \qquad \text{eq•7•10}$$

$$Sc = \frac{\nu}{D} \qquad \text{eq•7•11}$$

$$Re = \frac{v_g \times L}{\nu} \qquad \text{eq•7•12}$$

where v_g is the gas velocity and ν the kinematic viscosity of the gas.

By use of the equations above k_g has been estimated for different total pressures. The details in the calculations are shown in Appendix 6. The gas considered is Ar, since this is the purge gas used. The effect of P_{tot} on k_g is shown in Table 7•2. We see that k_g decreases with increasing pressure. This is because k_g is proportional to the diffusivity of the gas, D, which in turn is inversely proportional to the pressure. Although k_g here has been calculated for a special case (flow along a plate), for all systems kg will increase with decreasing total pressure..

Table 7•2: Effect of P_{tot} on k_g for a gas temperature of 1673 K

P_{tot} / bar	k_g / ms^{-1}
1	$1.3x10^{-3}$
0.6	$2.2x10^{-3}$
0.05	$2.6x10^{-2}$

In section 2·3 previous work on the CO-incorporation in Si-melts was presented.In the study conducted by Schmid *et al.* [1979] a silicon carbide layer was formed on the melt surface during the crystallisation, and silicon carbide particles also accumulated at the solid-liquid interface. In this case the operating pressure was, however, 0.1 Torr that is $1.3x10^{-4}$ Bar. At this low pressure k_g will be high. Consequently there is a small resistance for transport in the gas boundary layer. The observation of a silicon layer formation on the top indicate that in this experiment the rate- determining step was probably the transport in the melt boundary layer. One will thus have a high $[\%C]^i$ at the interface that is slowly transported to the bulk phase. This is also supported by the fact that the HEM-type furnace they used suppresses convection in the melt, giving thus a lower mass transfer coefficient in the melt.

In the work by Carlberg [1983] on CO-incorporation in Cz-Si melts the pressure was 10 Torr that is $1.3x10^{-2}$ Bar. They concluded that the rate-determining step here was the mass transfer coefficient for the transport through the ambient atmosphere. In this work their k_g includes transport from the graphite furnace parts to the ambient atmosphere above the melt surface and the transport through the gas boundary layer. They have estimated the k_g from experimental data found in literature.

Comparing these results with our observations: no silicon carbide layer formed on the ingot surface and a relatively high operating pressure, it seems reasonable that the rate determining step in our experiments was the transport through the gas phase.

If there was a significant CO-incorporation in the melt, one would expect the carbon content in the melt to increase steadily during the holding period prior to crystallisation start. When the crystallisation starts the carbon concentration will also increase because of segregation, it is thus difficult to distinguish the contribution from the exterior from the contribution from segregation. In the holding period the melt is held at the highest temperature during the process. Both k_g and p_{CO} increases with increasing temperature. In the testing experiment, 3 samples were taken out during this holding period (see 6·1·1). There is no increase in the carbon content with time elapsed; it seems to be rather constant. The variations in carbon contents measured are probably due to inhomogeneity in the samples and the uncertainty in the analysis. Also in MS-Exp 4 two

samples were taken out, one at the beginning of the holding period and the other at the end of the holding period, no increase in the carbon content was measured.

In conclusion, carbon incorporation from the gas phase may occur since CO is present in the ambient atmosphere due to the contact between the silica crucible and graphite components and SiO reacting with graphite. However, the degree of incorporation in the melt is unclear. It is probably controlled by transport through the gas phase; that is the transport from the graphite parts to the ambient atmosphere and the transport through the gas boundary layer. Based on the few results from the holding period it seems that the CO-incorporation for this system is a slow process, but further work is needed to quantify this. The flow pattern is of course important also for the CO-incorporation. In these large furnaces controlling the flow is not straightforward, and there may be differences for one crucible position to another, resulting in a different situation with regard to CO-incorporation.

(b) Contamination from dust particles

Another source to high carbon contents could be dust particles. In these furnaces there is an extended use of graphite components such as insulation, heating and supporting elements. After some use the surface of the graphite parts is covered with SiC from reaction 7•5.

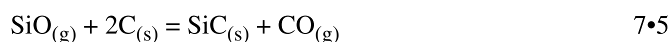

$$SiO_{(g)} + 2C_{(s)} = SiC_{(s)} + CO_{(g)} \qquad 7•5$$

Dust particles that can be both SiC and C may be incorporated into the charge both prior to furnace start and during the crystallisation process. In the first case this would be when the furnace lid is installed on the furnace, since the crucibles are covered before this. In both cases the dust particles would come primarily from the insulation plate above the crucibles. The amount of carbon needed to give 40 ppm mass in the melt is 10.1 g. This represents a volume of ~ 4.5 cm^3, with a density of carbon of 2.267 g/cm^3 [Lide, 1991-1992].

Below the solubility limit of carbon in liquid Si the carbon dust particles would dissolve, but once the carbon content is above the solubility limit one may expect that the carbon dust particles would react with the melt, resulting in a silicon carbide layer around

the particle. Such particles have not been observed in this work, but carbon inclusions have been observed in this material [Personal communications B.Johansen and F.Hugo at ScanWafer ASA, Wakshum 2004]

7•2•2 Evolution of carbon concentration in the melt after Scheil equation

Assuming that the silicon carbide precipitation occurs first at a certain stage in the crystallisation, that is at $f_s > 0.5$, we can compare our measurements in this area with the evolution after the Scheil equation, see eq 2·2. As k_0 we have used 0.07 the value from Nozaki *et al*. [1970]. Since we have used k_0 and not k_{eff} (see eq 2·3) which is unknown for this system, the carbon evolution in the melt will give the maximum carbon content possible in the melt for the measured initial carbon concentration, since k_{eff} is higher than k_0 (since $k_0 < 1$ for C). With regard to a continuous contamination of the melt from CO or carbon dust particles it is interesting to see where our measurements lie compared to the Scheil curve. Figures 7•4 to 7•6 show the Scheil curve and our melt measurements for MS-Exp 1, MS-Exp 2 and MS-Exp 4.

For MS-Exp 1 the measured values seems to follow the Scheil curve quite well up to $f_s = 0.4$. When it comes to MS-Exp 2 most of the measurements, except two, are well below the Scheil curve up to $f_s \sim 0.6$. Whereas for MS-Exp 4 all the measurements lie above the Scheil curve up to $f_s = 0.6$. Taking into account that k_{eff} is higher than k_0, and that k_{eff} would give a more correct Scheil curve for this system, then the Scheil curve would be displaced towards lower carbon concentrations in the melt for this system. This could mean that one can assume that a smaller continuous carbon contamination occurs, since our measurements for MS-Exp 1 and MS-Exp 4 then would be significantly higher than the Scheil curve for most of the measurements at low f_s. It should be mentioned that k_{eff} for this system is not constant during the solidification, as can be easily seen from the decreasing growth rate with f_s. Also the convection in the melt may change with f_s as the melt height is reduced.

What is interesting when comparing these curves with the measurements is the evolution at high f_s. It is seen particularly for MS-Exp 2 and MS-Exp 4 that a strong deviation from Scheil occurs, which would be the case when a silicon carbide precipitation

occurs. The Scheil equation will no longer describe the system when there is a formation of silicon carbide.

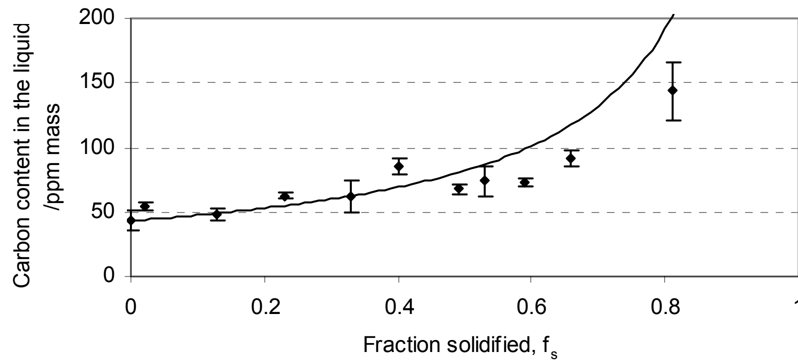

Figure 7•3: MS-Exp 1, our measurements and the Scheil curve for k_0=0.07 (solid line)

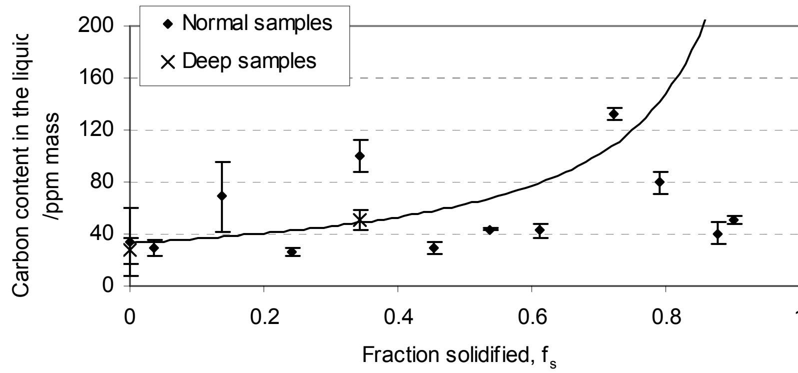

Figure 7•4: MS-Exp 2, our measurements and the Scheil curve for k_0=0.07 (solid line)

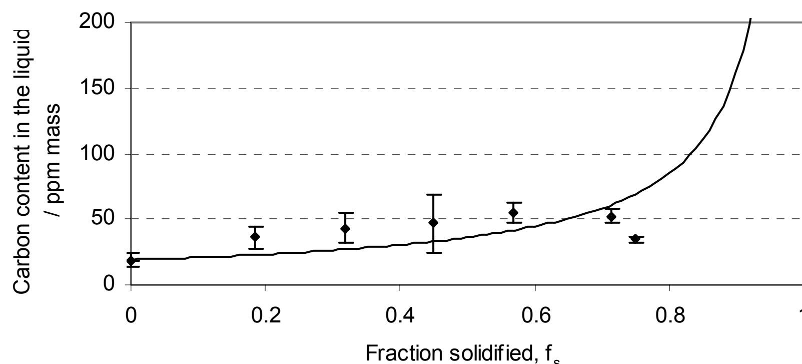

Figure 7•5: MS-Exp 4, our measurements and the Scheil curve for k_0=0.07 (solid line)

Summary on carbon contamination

As detailed above there are several carbon contamination sources in this system. A source that has not been discussed here is the crucible and coating. Concerning the crucible this contains non-measurable amounts of carbon according to Vesuvius. The coating particles contain ~ 0.2% carbon, see Table 4·2. Assuming that ~2% of the coating particles dissolve (see section 7•1•4) the increase in carbon content would be only 0.04 ppm mass, and thus negligible.

Distinguishing one of the above discussed sources as the major one is, however, difficult. The reason may be that there is no major source, but several "smaller" ones. There are indications of a smaller continuous contamination. However, the results from MS-Exp 4 ("pure feedstock", no recycled material), giving lower initial carbon content and lower maximum value than MS-Exp 1 and MS-Exp 2, could indicate that it is possible to reduce the carbon content to a certain degree by controlling the charge, in particular the amount and quality of the recycled material in the process.

7•2•3 Silicon carbide inclusions

The measured carbon contents in the melt prior to crystallisation start range from 10-40 ppm mass, see section 6·1. Since the melt temperature is ~1500 °C at this point in the process the initial carbon contents are all well below the solubility limit, and the melt is

thus hypoeutectic. In the solid phase the wafers below f_s = 0.1- 0.2 have carbon contents below the solid solubility limit. However, the solid phase reaches the solid solubility limit around f_s = 0.2. The carbon profiles for both the solid- and liquid phase increase with increasing f_s (up to a certain f_s). This is in contrast to the observation on the nitrogen profiles in the melt, where the content in the melt decrease with increasing f_s. The latter evolution would expected when if the melt is saturated with nitrogen, since the temperature decrease with increasing f_s, and the solubility will decrease with decreasing temperature as mentioned in section 7·1·1. This indicates that the eutectic for Si-N seem to occur close to equilibrium already from the start of crystallisation.

For carbon the situation is however different. The carbon profiles for the solid samples as a function of f_s are characteristic. The carbon content increases up to f_s = 0.5-0.7 where it is supersaturated , then drops down and approaches a content of 8 ppma. This clear profile in the solid samples has also been evidenced in previous measurements for this kind of furnace [Hjemås, 2002]. Recent furnace improvements after this work have reduced this tendency [Personal communications Erik Sauar, 2004] . In the work of Schönecker *et al.* [2004] carbon profiles from various multi-crystalline silicon ingots were measured by FTIR. Also a few of these show the same kind of profile with peaking values around f_s = 0.5. Moreover, for the melt samples from MS-Exp 2 and 4, a similar profile as for the solid samples is weakly observed, but displaced towards higher f_s.

These particular profiles passing through supersaturated levels indicate that the precipitation of silicon carbide does not proceed to equilibrium during a large part of the crystallisation. However, reaching above f_s = 0.5, the carbon contents in the solid phase decrease and flatten out. We associate this drop in carbon contents with silicon carbide precipitation. What exactly brings about this change in the system is unclear. The drop in carbon content could perhaps be explained by a situation where the carbon content in the solute boundary layer reaches a level where silicon carbide crystals may precipitate as a primary phase. These crystals can then act as seeds on which the carbide formed by the eutectic reaction can grow at conditions closer to the equilibrium state. Thus, the degree of supersaturation of the silicon decreases as the experimental results indicate.

Nozaki *et al.* [1970] mention in his work that "usually silicon carbide will not precipitate immiediately when the liquid phase has become supersaturated..... In order for

the carbon to precipitate many carbon atoms must condense. The probability of their encounter, however, should be quite small because of their low soubility. " This can explain the necessity of a carbon build-up in the solute boundary layer before it precipitates. It has also been suggested that a high interface energy and volume decrease associated with carbon precipitation in the solid phase made it difficult [Taylor *et al.*, 1993], see section 7·4.

The inclusion study revealed growth of silicon carbide on the silicon nitride inclusions, on the crucible wall, and also "single" silicon carbides. The latter ones may have nucleated on silicon nitride coating particles in the melt, or smaller precipitated silicon nitrides. The fact that the carbides grow on the precipitated nitrides and not vice versa is a further indication that the silicon nitrides form first and that the silicon carbides are formed at a later stage.

As presented in 2·4 different types of silicon carbide particles have been reported to occur in multi-crystalline silicon. Especially in EFG ribbon silicon SiC particles are frequently observed due to the use of graphite dies and crucibles thus giving a melt highly saturated with carbon. Rao *et al.* [1976] reported in their study large (0.5 mm) SiC-particles and clusters of SiC-particles that appeared as inclusions in the material. These particles are formed at the silicon die interface and some of these particles may be incorporated in the growing ribbon. The particles in that study resembles the ones observed in our study, being large particles with a high crystalline nature and well faceted faces.

Another type of SiC-precipitates were reported by Hejjo Al Rifai *et al.* [2004]. These were filaments of $< 1\text{-}3\ \mu m$ in diameters lying in grain boundaries, but similar filaments lying outside of grain boundaries were also observed. This type of precipitates lead to strong ohmic shunts. The investigated cells in this work came from the upper part of an ingot from a different manufactureur than in our work. This filament-type SiC-precipitate has not been observed in our work. Since only small areas have been investigated microscopically, this type of precipitate may very well occur in certain regions of the ingot. As described in 2·8 SiC-precipitation has also been connected to twinning

The SiC-precipitation seem to occur by different growth mechanisms, resulting in precipitates/particles of different morphology. The type of growth mechanism occurring in a region is possibly dependent on several factors such as the carbon concentration in the melt and conditions at the growth front. Also precipitation in the solid phase may occur during cooling, this is possibly seen as smaller precipitates at the grain boundaries where diffusion is faster.

<u>"Corrected" carbon contents in solid phase</u>

Based on the rr-test it was assumed that the FTIR-measurements of substitutional carbon overestimate this concentration, see chapter 5. If we consider a fix value of 30% as the overestimation, we can calculate a "corrected" profile. This value is based on the difference in NTNU-FTIR and the SIMS measurements, and we are not considering the slight decrease in resistivity with increase in fraction solidified.

Such "corrected" values are shown in Figure 7•6 for position 1 (centre of ingot) for MS-Exp 1 to MS-Exp 3.

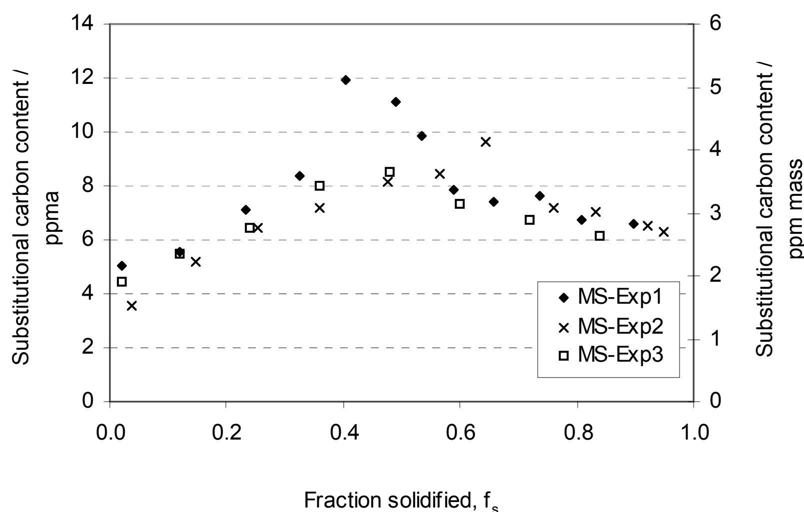

Figure 7•6: "Corrected" FTIR-profiles as a function of fraction solidified, when considering an overestimation of 30%.

We see from Figure 7•6 that the peaks now are at 11.9 ppma, 9.7 ppma and 8.5 ppma, the levels at the lowest f_s are at 5.1 ppma, 3.5 ppma and 4.4 ppma, while the “equilibrium” levels now approach 6 ppma.

7•3 Oxygen contents in the melt

From Table 6·8 it is seen that the oxygen contents in the melt decreases with increasing fraction solidified. The oxygen levels are also below the solubility limit in the liquid phase, reported to ~ 23 ppm mass [O’Mara, 1990, reference therein]. Decreasing oxygen contents with increasing f_s in the solid phase have been frequently measured for similar crystallisation systems [f.in. Schönecker *et al.*, 2004], and is also seen for the oxygen measurements in the rr-test. The decrease in oxygen content with fs has been explained by the decreased contact with the crucible surfaces as the crystallisation proceeds, decreasing thus the contact with the primary source to oxygen in the system which is the crucible and/ or coating. Also the continuous evaporation of SiO contributes to the decrease in oxygen as the crystallisation proceeds. The eventual effect from segregation is less clear, since the equilibrium distribution coefficients for oxygen range from 0.3 to 1.48 [O’Mara, 1990, references therein].

7•4 Pushing of particles by a plane front

The inclusion study showed that the inclusions found in the top-cuts contained larger and more clusters than the inclusions from the wafers (bulk). This was especially clear in MS-Exp 3 where small silicon nitride inclusions were found in the bottom wafer, while large networks of silicon nitrides were found in the top-cut of the same block, see Figures 5·19 and 5·20. It is therefore likely that inclusions grow during the crystallisation process. The inclusions, both SiC and Si_3N_4, have a higher density than the melt and will thus sink. We therefore think that the growth occurs in the solute-boundary layer or in the vicinity of this layer, close to the crystallisation front. In this layer there is the highest solute concentrations, since there is a continuous rejection of solute from the crystallisation front. In MS-Exp 1, a wafer at f_s ~ 0.4 contained significant amounts of inclusions, while wafers dissolved above and below this position showed no inclusion content by the dissolution method. This could be due to a sudden engulfment of particles pushed by the

solidification front, giving thus a sudden appearance of large inclusions in the material. Pushing can also explain why we observe larger and more inclusions in the top although the nitrogen content in the melt decreases with increasing height. It is suggested that a pushing mechanism occurs for this system.

The pushing phenomenon was introduced in section 2·8. It was described as a phenomenon occurring when $\sigma_{sp} > \sigma_{sl} + \sigma_{lp}$, where σ_{sp} is the interfacial energy solid-particle, σ_{sl} is the interfacial energy solid-liquid and σ_{lp} is the interfacial energy liquid-particle. Uhlmann *et al.* [1964] derived a model based on this concept. In the later years also a thermal conductivity criterion has been considered. Zubko *et al.* [1973] confirmed experimentally that when the thermal conductivity of the particle was lower than the thermal conductivity of the melt ($\lambda_p < \lambda_l$) the particle was pushed. According to Stefanescu et al. [1988] a positive difference in the heat conductivity between the particle and the melt leads to a trough on the interface, thus engulfing, whereas a negative difference in the heat conductivity leads to a bump on the interface, resulting in pushing of the particle, see Figure 7•7. For SiC the heat conductivity range from 14 to 34 W/mK, whereas the heat conductivity of the melt is 55 W/mK, see Table 7•3, which should lead to pushing according to this criterion.

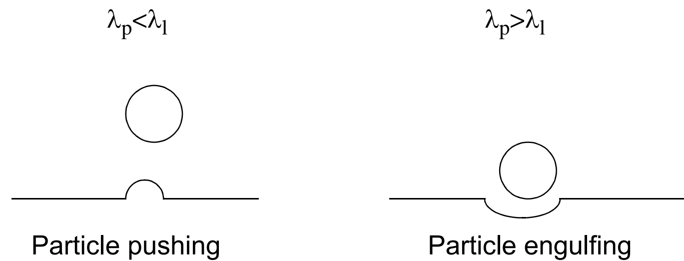

Figure 7•7: Particle pushing/engulfing related to heat conductivity of particle and melt, as explained by Stefanescu et al. [1988]

A heat diffusivity criterion was derived by Surappa and Rohatgi [1981], see eq 7•13.

$$\left[\frac{\lambda_p c_p \rho_p}{\lambda_l c_l \rho_l}\right]^{1/2} < 1 \qquad \text{for particle pushing} \qquad \text{eq•7•13}$$

where λ_p is the thermal conductivity of the particle, c_p is the specific heat capacity of the particle and ρ_p is the density of the particle, whereas the index l denotes the same properties for the melt. We see from this criterion that a low heat capacity, heat conductivity and density for the particle compared to the liquid results in particle pushing. For β-SiC, using the data in Table 7•3, one obtains a value of 0.640 for eq 7•13 when using the lowest value for the thermal conductivity for the particle (14 W/mK), when using the highest thermal conductivity of the particle the value obtained is 0.998. Both values are below one and the criterion for particle pushing according to Surappa and Rohatgi is thus fulfilled. For Si_3N_4 the specific heat capacity at room temperature was reported to be 170 J/kg K, while the thermal conductivity was reported to be between 16-33 W/mK at room temperature [www.ai.mit.edu, 2004], and the density is 3.19-3.2 g/cm^3 at room temperature [Riley, 2000]. Unfortunately, values for the specific heat capacity and thermal conductivity for silicon nitride at the melting point of silicon have not been found. Calculating a value for eq 7•13 based on the room temperature values, gives 0.26 (λ=17 W/mK) and 0.36 (λ=33 W/mK).

As stated in 2·6 pushing depends also on the interface velocity and the particle radius. Kim and Rohatgi [1998] calculated the critical velocity for pushing of a SiC particle of 10 μm in an aluminium melt for the different models presented in Figure 2·18. We see from this table that the calculated values vary from 0.180 μm/s to 14800 μm/s. The lowest values are obtained with the earliest models that did not include thermal conductivity differences. The V_{cr}'s obtained by the models of Stefanescu *et al.* [1990] and Kim and Rohatgi [1998] are the closest to the experimental observation (14800 μm/s) by Wu *et al.* [1994]. The experimental observation is one order higher than what the models predict. Similar literatur for the system Si-SiC nor Si-Si_3N_4 has not been found.

Table 7•3: Values for the thermal conductivity and heat capacity of Si(l) and SiC(s)

Substance	Thermal conductivity, λ / W $m^{-1}K^{-1}$	Specific heat capacity, c / J kg^{-1} K^{-1}	Density, ρ / g cm^{-3}
SiC	14-34 at m.p. [Klevan, 1997, ref. therein]	1293 at 1412 °C [Klevan, 1997, ref. therein]	3.21 at room-temp [Lide, 1992] 3.1 at 1412 °C [Klevan 1997, and ref. therein]
Si	55 at m.p. [Engh, 1992]	968 [Klevan, 1997, ref. therein]	2.57 at m.p. [Lide, 1992]

Using the model of Stefanescu *et al.* (eq 7•12 we have calculated V_{cr} as a function of particle radius for the system Si-SiC (see Figure 7•8) , the parameter values employed in the calculation are listed in Table 7•4. The model is based on a force balance (repulsive and drag force) for the particle in the front of the solid-liquid interface, and includes a term accounting for the difference in thermal conductivity. The repulsive force results from interfacial energy difference.

$$V_{cr} = \frac{\Delta\sigma_0 \times d_0}{6(n-1)\mu r}\left(2 - \frac{\lambda_p}{\lambda_l}\right) \qquad \text{eq•7•14}$$

where $\Delta\sigma_0$ is the difference in interfacial energy, $\Delta\sigma_0 = \sigma_{ps}-(\sigma_{pl} + \sigma_{sl})$, d_0 is the interatomic distance in the melt, μ is the viscosity of the melt, r is the particle radius, λ_p is the thermal conductivity of the particle and λ_l is the thermal conductivity of the melt and n is equal to 2

Table 7•4: Parameter values employed in calculating V_{cr}

Parameter	Value	Reference	Remarks
μ	$9.4*10^{-4}$ Ns m^{-2}	Klevan [1997], reference therein	
$\Delta\sigma_0$	0.1 Nm^{-1}	Klevan [1997]	

Table 7•4: Parameter values employed in calculating V_{cr}

Parameter	Value	Reference	Remarks
d_0	$2.6*10^{-10}$ m		Calculated from density of Si liquid at m.p. (2.57 g cm^{-3})
λ_p	24 $Wm^{-1}K^{-1}$	Klevan [1997], reference therein	Mean value of the range at m.p.
λ_l	55 $Wm^{-1}K^{-1}$	Engh [1992]	

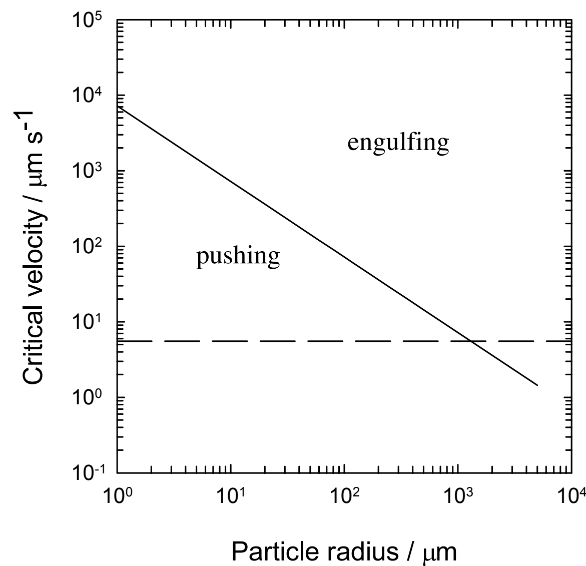

Figure 7•8: Critical interface velocity as a function of particle radius for the system $Si_{(l)}$-$SiC_{(s)}$, dashed line represents the mean growth rate in industry (~20 mm/h=5.55 µm/s). Calculated from the model of Stefanescu et al. [1988]

At a growth velocity of 5.55 µm/s, which represents the mean growth rate in industry, engulfing will occur for a particle radius of 1296 µm or above. This means a particle diameter of ~2500-2600 µm. The maximum particle/cluster sizes obtained from the particle size distribution of top-cuts in 6·3·6 are below this critical diameter, mostly in the range 100-1000 µm.

All the models in Figure 2·18 consider the particles as spherical. The silicon carbides may be approximated as spherical, but not the needle-like silicon nitrides nor the clusters. For non-spherical particles drag is much greater thus giving a lower critical velocity. Unfortunately, data for surface energy difference and the thermal conductivity (at m.p. of Si) have not been found for Si_3N_4. and a calculation of the critical velocity for this particle has not been performed.

Even though the inclusions are concentrated in the top-cuts (also the side-cuts), there are inclusions present in the bulk as well. Especially studies of chemical mechanical polished large wafers (15x15 cm^2) have revealed even high inclusion densities [Wakshum, 2004 and Mjøs, 2004]. Several factors such as interface morphology, fluid flow and especially fluctuations in growth rate may influence the pushing mechanism and lead to engulfing. Stefanescu *et al.* [1990] also observed occurence of bands of particles at certain regions, this was connected to a high content of particles ahead of the interface. When the volume fraction of particles ahead of the front is high, it will increase the viscosity of the melt in this area, which in turn will reduce the V_{cr}. Thus, if the volume becomes significantly high it may lead to engulfing of inclusions. Relative viscosity (eq 6·13, Stefanescu *et al.*, 1990, and references therein) rather than simple viscosity is employed in calculating V_{cr}, when the particle content ahead of the interface is high.

$$\mu_r = \mu(1 + 2.5 \times f_p + 10.05 \times f_p^2) \qquad \text{eq•7•15}$$

where μ_r is the relative viscosity, μ the viscosity of the pure liquid, and f_p the volume fraction of particles

Fluid flow is another factor that is not included in the models and most of the experimental work on pushing. However, Han and Hunt [1994], have investigated the pushing phenomenon under different flows. They observed that under laminar conditions, and with particles of higher density than the melt, considerably less particles were engulfed than under turbulent flow conditions, even though at low flow velocities, for the laminar case, there were an increased concentration of particles near the interface. They concluded that trapping of particles under flow conditions was mainly connected to larger

lateral motion of some particles towards the interface rather than to the larger particle concentration.

In conclusion it is plausible that a pushing mechanism occurs in this system. It must be regarded as a delicate balance. During solidification some inclusions are engulfed (bulk-inclusions) as indicated above, while some remain in the melt and are allowed to grow into larger clusters due to pushing (top-cut inclusions).

7•5 Effects from other elements on the precipitation

In the melt there are elements besides nitrogen and carbon that may be present in high amounts, particularly iron and oxygen. The effect such elements may have on the precipitation has not been studied in this work. On the precipitation in the solid phase, some points may be mentioned.

It has been observed that carbon do not precipitate easily from solid silicon containing supersaturated levels of substitutionally dissolved carbon. However, the presence of high amounts of oxygen or silicon self-interstitials facilitate the carbon precipitation [Taylor *et al.*, 1993]. It was suggested that a high interface energy and the volume decrease associated with carbon precipitation made it difficult. When coprecipitation of carbon and oxygen occurs both the volume decrease and the high interface energy will decrease, due to the effect from oxygen. Oxygen on the other hand precipitates readily and the precipitation is enhanced by carbon [f.inst. Shimura *et al.*, 1985, and Kung *et al.*, 1983].

7•6 Low life-time dip

During crystallisation there seems to be some phenomena that occur around the same fraction solidified. These are the drop in carbon content (solid phase),and a dip in the life-time measurements for occasional runs (not systematic!). In MS-Exp 1 these two phenomena are very pronounced. The life-time scan of block 10 (Figure 5·7) showed a dip in the life-time scan ranging from $f_s \sim 0.4\text{-}0.6$. When comparing with the carbon contents of the solid phase (Figure 5·8), the carbon peak value occurs at $f_s \sim 0.4$, starts dropping and levels out at $f_s \sim 0.6$. We have previously connected this carbon drop with a primary

silicon carbide precipitation. Could the low life-time in this region be due to a sudden and massive silicon carbide precipitation ? Worth noting is that MS-Exp 2 and 4 gave no such band of low life-time, but in these experiments both the initial carbon contents in the melt and the carbon peaking value for the solid phase were lower than in MS-Exp 1. In the industry such bands of low life-time occurs from time to time, these regions may have a microcrystalline appearance [Personal communications Bertil Johansen, ScanWafer ASA]. Sinton *et al.* [2004] also measured a life-time drop in a block produced by different manufacturer than in this study. This low life-time dip seemed to correlate with "trapping[1]" density. However, the physical origin of the traps were not identified.

In conclusion, finding the origin of the occasionally occurring phenomenon of low life-time dips is important for process improvement. A suggestion has been proposed here, however, in order to clarify this point further work and analyses are necessary.

7•7 Carbon solubility

The results on the carbon profiles (solid phase) indicate that dissolved carbon approach equilibrium at the later stage of the crystallisation. For MS-Exp 2 and 4 a drop in the carbon content are also measured in the melt samples. Assuming that at this stage one approaches equilibrium, then these last melt samples could give a rough indication of the approximate carbon solubility in liquid silicon at the sampling temperature. However, the melt is at this stage enriched in various elements (f.in. boron, nitrogen, iron) that may sligthly influence the solubility. The sampling temperature is as previously mentioned not precise. Still, in light of the large scatter in the literature on the carbon solubility it is interesting to take a closer look at these carbon contents. In Table 7•5 carbon contents from these samples are listed. We may assume that the sample temperature at this later stage in the crystallisation probably lies somewhere between the melting point of silicon and 10-15 °C above the melting point. As seen from Table 7•5 the carbon values range from 35 to 51 ppm mass. This could mean that the solubility of carbon at the melting point may be in the vicinity of 30 ppm mass, and thus close to the value from the phase diagram

1. Minority carrier trapping centers

of Nozaki *et al.*[1970]. However, the best way of "circling in" the carbon solubility in liquid silicon would be by laboratory measurements designed for this purpose.

Table 7•5: Carbon contents in selected melt-samples from MS-Exp 2 and MS-Exp 4

Sample	Carbon content / ppm mass	Temperature / K
MS-Exp 2, sample no. 11	41	1694 (1421 °C)
MS-Exp 2, sample no. 12	51	1692 (1419 °C)
MS-Exp 3, sample no. 8	35	1688 (1415 °C)

7•8 Temperature gradient in the melt

From the pyrometer readings and the measurements of fraction solidified we can estimate the temperature gradient in the melt, under the assumption that there is no large deviations in the solidification process for the four crucibles. By temperature gradient we mean here the difference between the surface temperature (T_s) and the interface temperature (T_m = 1685 K) divided on the height of the melt (h). Table 7•6 shows the estimated temperature gradient in the melt for different f_s, measurements at $f_s < 0.1$ are not included since this represents a transient period.

For MS-Exp 1 and MS-Exp 2 where the mean growth rate was the same show nearly constant temperature gradients, a slight decrease with increasing f_s is indicated. The mean temperature gradient for these two runs is 0.22 °C/mm (0.03) and 0.20 °C/mm (0.02), respectively where the numbers in brackets are the standard deviation. The situation is different for MS-Exp 4, where the temperature gradient is clearly decreasing with increasing f_s, it starts at 0.19 °C/ and for the last measurement is down at 0.05 °C/mm. In this run the growth rate was reduced compared to MS-Exp 1 and MS-Exp 2.

Our melt samples were extracted at ~50 mm below the melt surface. Since the temperature profile in the melt is unknown, we decided to use the surface temperature as

an indication of the sampling temperature. This will then indicate the maximum sampling temperature. However, with convection in the system as we assume (see section 4·4) the temperature at the sampling position should be close to the surface temperature. At high f_s where the sampling position is closer to the interface, the surface temperature approaches the interface temperature as seen f.in. in Table 7•5, the temperature difference between the interface and the surface is now small

Table 7•6: Estimated temperature gradient for MS-Exp 1, MS-Exp 2 and MS-Exp 3 at different fraction solidified, f_s

MS-Exp 1		MS-Exp 2		MS-Exp 4	
f_s	$(T_s-T_m)/h_m$	f_s	$(T_s-T_m)/h_m$	f_s	$(T_s-T_m)/h_m$
0.13	0.25	0.14	0.22	0.18	0.19
0.23	0.23	0.24	0.22	0.32	0.17
0.33	0.24	0.34	0.20	0.45	0.13
0.40	0.24	0.45	0.20	0.57	0.10
0.49	0.23	0.54	0.19	0.71	0.05
0.53	0.21	0.61	0.18	0.75	0.05
0.59	0.19	0.72	0.18		
0.66	0.21	0.79	0.18		
0.81	0.17	0.88	0.22		
		0.90	0.19		

REFERENCES

Carlberg T. (1983), *A quantitative model for carbon incorporation in czochralski silicon melts*, J.Electrochem.Soc.:Solid-state science and technology, Vol.130, No.1, 168-171.

Cröll A., R.Lantzsch, S.Kitanow, N.Salk, F.R.Szofran and A.Tegetmeier (2003), *Melt-crucible wetting behavior in semiconductor melt growth systems*, Cryst.Res.Technol.38, No.7-8, 669-675

Duffy M.T., S.Berkman, G.W.Cullen, R.V.D'Aiello and H.I.Moss (1980), *Development and evaluation of refractory CVD-coatings as contact materials for molten silicon*, J.Cryst.Growth 50, 347-365

Engh T.A. (1992), *Principles of Metal Refining*, Oxford University Press

Endo Y., Y.Yatsurugi, Y.Terai and T.Nozaki (1979), *Equilibrium of Carbon and Oxygen in Silicon with Carbon Monoxide in Ambient Atmosphere*, J.Electrochem.Soc.: Solid-State Science and Technology, Vol.126, No.8, 1422-1425

Grün R.(1979), *The Crystal Structure of β-Si_3N_4; Structural and Stability Considerations Between α- and β-Si_3N_4*, Acta.Cryst., B35, 800-804

Han Q. and J.D.Hunt (1994), *Particle pushing: the attachment of particles on the solid-liquid interface during fluid flow*, J.Cryst.Growth, Vol.140, 406-413.

Hejjo Al Rifai M., O.Breitenstein, J.P.Rakotoniaina, M.Werner, A.Kaminski and N. Le Quang (2004), *Investigation of Material-Induced-Shunts in Block-Cast Multicrystalline Silicon Solar Cells caused by SiC precipitate filaments*, Proceedings for the 19th European Photovoltaic Solar Energy Conference and Exhibition, in press

Hjemås P.C. (2002), Fordypningsemne; Karakterisering av multi-krystallinsk Silisium - Måling av oksygeninnhold, kornstørrelser og tekstur, Institute for Materials Technology, Norwegian University of Science and Technology (Trondheim)

Iguchi Y. and T.Narushima. (1993), *Solubility of oxygen, nitrogen and carbon in liquid silicon*, First International Conference on Processing Materials for Properties, The Minerals, Metals & Materials Society, 437-440

Inomata Y. and T.Yaname (1974), *β - Si_3N_4 single crystals grown from Si-melts*, J.Cryst.growth 21, 317-318

Jennings H.M. (1983), *Review On reactions between silicon and nitrogen*, J.Mat. Sci. 18, 951-967

Kaiser W and C.D.Thurmond (1959), *Nitrogen in Silicon*, J.Appl.Phys., Vol. 30, No. 3, 427-431,

Kim J.K. and P.K.Rohatgi (1998), *The effect of the diffusion of solute between the particle and the interface on the particle pushing phenomena*, Acta mater., Vol.46, No.4, 1115-1123

Klevan O.S. (1997), *Removal of C and SiC from Si and FeSi during ladle refining and solidification*, PhD-thesis, Institute of Materials Technology, Norwegian University of Science and Technology (Trondheim)

Kung C.Y., L.Forbes and J.D.Peng (1983), *The effect of carbon on oxygen precipitation in high carbon CZ silicon crystals*, Mat.Res.Bull., Vol.18, No.12, 1437-1441

Lawerenz A., M.Ghosh, K.Kremmer, V.Klemm, A.Müller and H.J.Möller (2003), *Infrared Transmission of Rod-Like Defects in Multicrystalline Silicon*, Solid State Phenomena Vols. 95-96, 501-506

Li J.G. and H.Hausner (1992), *Influence of oxygen partial pressure on the wetting behaviour of silicon nitride by molten silicon*, J.Euro.Cer.Soc. 9, 101-105,

Lide D.R. (1991-1992), *CRC Handbook of chemistry and Physics*, 72nd Ed.

Meléndez-Martínez J.J. and A.Domínguez-Rodríguez (2004), *Creep of Silicon nitride*, Progress in Materials Science, vol. 49, issue 1, 19-107

Mjøs Ø. (2004), *PhD-thesis in progress*, Institute of Materials Technology, Norwegian University of Science and Technology (Trondheim)

Mukai K. and Z.Yuan (2000), *Wettability of Ceramics with Molten Silicon at Temperatures ranging from 1693 to 1773 K*, Mat.Trans., JIM, Vol.41, No. 2, 338-345

Mukerji J. and S.K.Biswas (1981), *Effect of Iron, Titanium, and hafnium on Second-Stage Nitriding of Silicon*, J.Am.Cer.Soc., Vol. 64, No. 9, 549-552,

Möller H.J. (2004), *Carbon-Induced Twinning in Multicrystalline Silicon*, Sol.State.Phen., Vol.95-96. 181-186

Nozaki T., Y.Yatsurugi and N.Akiyama (1970), *Concentration and behavior of carbon in semiconductor silicon*, J.Electrochem.Soc.:Solid state science,Vol.117, No.12, 1566-1568

O'Mara W.C., R.B.Herring and L.P.Hunt (1990), *Handbook of Semiconductor Silicon Technology*, Noyes Publications

Rao C.V., H.E.Bates and K.V.Ravi (1981), *Electrical effects of SiC inclusions in EFG silicon ribbon solar cells*, J.Appl.Phys., Vol.47, No.6

Riley F.L. (2000), *Silicon nitride and related materials*, J.Am.Cer.Soc., Vol.47, No.6, 245-288

Schönecker A., L.J.Geerligs and A.Müller (2004), *Casting Technologies for Solar Silicon Wafers: Block Casting and Ribbon-Growth-on Substrate*, Solid State Phenomena Vols. 95-96, 149-158

Schmid F., C.P.Khattak, T.G.Digges and L.Kaufmann. (1979), *Origin of SiC Impurities in Silicon Crystals Grown from the Melt in Vacuum*, J.Electrochem.Soc.: Electrochemical Science and Technology, Vol.126, No.6, 935-938.

Shimura F., J.P.Baiardo and P.Fraundorf (1985), *Infrared absorption study on carbon and oxygen behavior in Czochralski silicon crystals*, Appl.Phys.Lett., Vol.46, No.10, 941-943

Sinton R.A., T. Mankad, S. Bowden and N. Enjalbert (2004), *Evaluating blocks and ingots with quasi-steady-state lifetime measurements,* 19th European Photovoltaic Solar Energy Conference and Exhibition

Stefanescu D.M., B.K.Dhindaw, S.A.Kacar and A.Moitra (1988), *Behavior of ceramic particles at the solid-liquid metal interface in metal matrix composites*, Metall.Trans. A, Vol.19A, 2847-2855

Stefanescu D.M., A.Moitra, A.Kakar and B.K.Dhindaw (1990), *The influence of buoyant forces and volume fraction of particles on the particle pushing/entrapment transition during directional solidification of Al/SiC and Al/Graphite composites*, Metall.Trans., Vol.21A, 231

Surappa M.K. and P.K.Rohatgi (1981), *Heat diffusivity criterion for the entrapment of particles by moving solid-liquid interface*, J.Mat.Sci.Lett., Vol.16, 562-564

Taylor W.J., T.Y.Tan and U.Gösele (1993), *Carbon precipitation in silicon: Why is it so difficult?*, Appl.Phys.Lett., Vol.62 (25), 3336-3338

Uhlmann D.R. and B.Chalmers (1964), *Interaction between particles and a solid-liquid interface*, J.Appl.Phys., Vol.35, No.10, 2986-2993

Wakshum T.M (2004), *The effects of SiC and Si_3N_4 inclusions in Multicrystalline Silicon Solar Cell Performance*, Master of science thesis in Physics, Department of Physics, Norwegian University of Science and Technology (Trondheim)

www.ai.mit.edu/people/tk/tks/silicon-nitride.html, 2004

Wu Y., H. Liu and E.J. Lavernia (1994), *Solidification behavior of Al-Si/SiC MMCs, during wedge-mold casting*, Acta metall.mater., Vol.42, 825-837

Yatsurugi Y., N.Akiyama, Y.Endo and T.Nozaki. (1973), Concentration, *Solubility, and Equilibrium Distribution Coefficient of Nitrogen and Oxygen in Semiconductor Silicon*, J.Electrochem.Soc.: Solid-State Science and Technology, Vol.120, No.7, 975-979

Zubko A.M., Lobanov V.G. and Nikonova V.V. (1978), *Reaction of foreign particles with a crystallization front*, Soviet physics, Crystallography, Vol. 18, 239-241

Chapter 8 Conclusions and suggestions for further work

This study aimed at improving understanding of the formation of inclusions in multicrystalline silicon ingots during crystal growth. It has given both results with clear directions how to improve the crystallisation process, and results which should be followed up by further studies before a more complete understanding is achieved. Part of the aim was also to develop a method for melt-sampling at the industrial furnace, and to initiate the FTIR-measuring technique for carbon and oxygen at the institute.

Method development:

A method for melt-sampling in an industrial scale furnace operated below 1 bar, has been successfully developed. Establishing knowledge of the contents of various elements in the liquid phase during crystallisation can give information of the quality needed for a SoG-silicon. It can also be used to study the effective distribution coefficients, that in turn will give information on the crystallisation process.

The FTIR-measuring technique of dissolved carbon and oxygen has been initiated at the institute. For oxygen it has given good results while for carbon the measurements overestimate the carbon content. This is probably due to the low resistivity of the investigated samples. To improve the carbon measurements on low resistivity samples one could try out a standard with the same low resistivity as in the samples. Measurements should be conducted also on higher resistivity samples and compared with SIMS-measurements and possibly also other measuring techniques.

Identification of inclusions:

Two different types of large melt-grown inclusions were identified. These were well faceted crystals of β-SiC and β-Si_3N_4. The study revealed growth of silicon carbide on the silicon nitrides, “single” silicon carbides, and also larger clusters of both types of inclusions. These clusters were found particularly in the top-cuts.

Silicon nitride formation:

This study revealed a significant silicon nitride formation, which was somewhat surprising. The proposed formation mechanism is by dissolution-precipitation, where the dissolving part is the coating. During the holding period prior to crystallisation start the melt becomes saturated with nitrogen, as the melt analyses indicate. Precipitation of silicon nitride therefore occurs when the crystallisation starts and the melt becomes hypereutectic. Silicon nitrides are thus forming already at the start of crystallisation.

The coating plays an essential role in the silicon nitride formation. Further work for improvement of the process should therefore focus on the coating. It is important to increase the stability of the coating, especially its ability to stay on the crucible walls, thereby reducing the amount of coating particles in the melt since these are supposed to act as nucleation sites in the bulk melt. It would also be interesting to investigate the effect of the phase modification (α or β) on the formation of silicon nitride in the melt, since the phase transformation (α to β) may be a driving force for the precipitation of β-Si_3N_4.

Silicon carbide formation:

Concerning silicon carbide formation the picture is less clear. The initial carbon contents ranging from 18 to 43 ppm mass are below the solubility limit of carbon in silicon at the initial temperature (~1500 °C), and increases with increasing fraction solidified (f_s). A decrease at high f_s was observed in two of the runs. It is proposed based primarily on the results from the solid phase carbon profiles, that there is a silicon carbide precipitation around $f_s = 0.5$. This precipitation seems to occur first after a carbon build-up in the solid and liquid phases. The eutectic reaction approaches the equilibrium levels for the solid phase after this precipitation. Further studies on the inclusion contents at different height positions would be of help. This could be conducted on primarily large area wafer samples

prepared by, for instance, the chemical-mechanical polishing technique [Mjøs *et al*. 2004]. A comparison of the silicon carbide content at the different height positions would be particularly interesting.

It would also be interesting to follow up the idea of the connection between high carbon content (giving a more massive silicon carbide precipitation) to the low life-time dips occasionally occurring around f_s~0.5. A study of the dissolved carbon profiles in blocks where such a dip is observed compared with the carbon content of blocks without this kind of dip could be a starting point. This could be combined with a study of the microstructure in the material in this area of low lifetime.

Concerning the reduction of the initial carbon content in the melt, one could first focus on the recycled material used in the charge. Upgrading this material by removal of inclusions, by for instance filtration or settling, could be considered.

Pushing mechanism:

A pushing mechanism has been proposed to occur in this system, where some inclusions may be engulfed during crystallisation while a part of the inclusions remain and continue growing in the melt. This may explain the difference in inclsuion content and size between top-cuts and bulk-material observed in this study. A particle diameter of 2500 μm was calculated for a growth rate of 20 mm/h by use of the model by Stefanescu *et al.* [1990].

Solubilities:

The literature survey on the carbon and nitrogen solubility in liquid silicon has shown that there is a large scatter between the different studies. It has been attempted to discuss and evaluate the merits of the various studies on carbon. A value of the solubility in equilibrium with SiC at the melting point of Si ranging from 30-50 ppm mass is indicated. The analyses of the nitrogen contents in the melt obtained in this study support the solubility (4 ppm mass at m.p.) reported by Iguchi and Narushima [1993]. However, it would be interesting to conduct careful experiments for determining solubilities.

REFERENCES

Iguchi Y. and T.Narushima. (1993), *Solubility of oxygen, nitrogen and carbon in liquid silicon*, First International Conference on Processing Materials for Properties, The Minerals, Metals & Materials Society, 437-440

Mjøs Ø., G.Stokkan, A.K.Søiland and L.Arnberg (2004), *Mapping of Silicon Carbide and Silicon Nitride Particles on Chemical Mechanical Polished mc-Silicon Wafers*, 19th European Photovoltaic Solar Energy Conference and Exhibition, in press

Stefanescu D.M., B.K.Dhindaw, S.A.Kacar and A.Moitra (1988), *Behavior of ceramic particles at the solid-liquid metal interface in metal matrix composites*, Metall.Trans. A, Vol.19A, 2847-2855

APPENDIX 1

X-ray diffractogram of coating particles (powder)

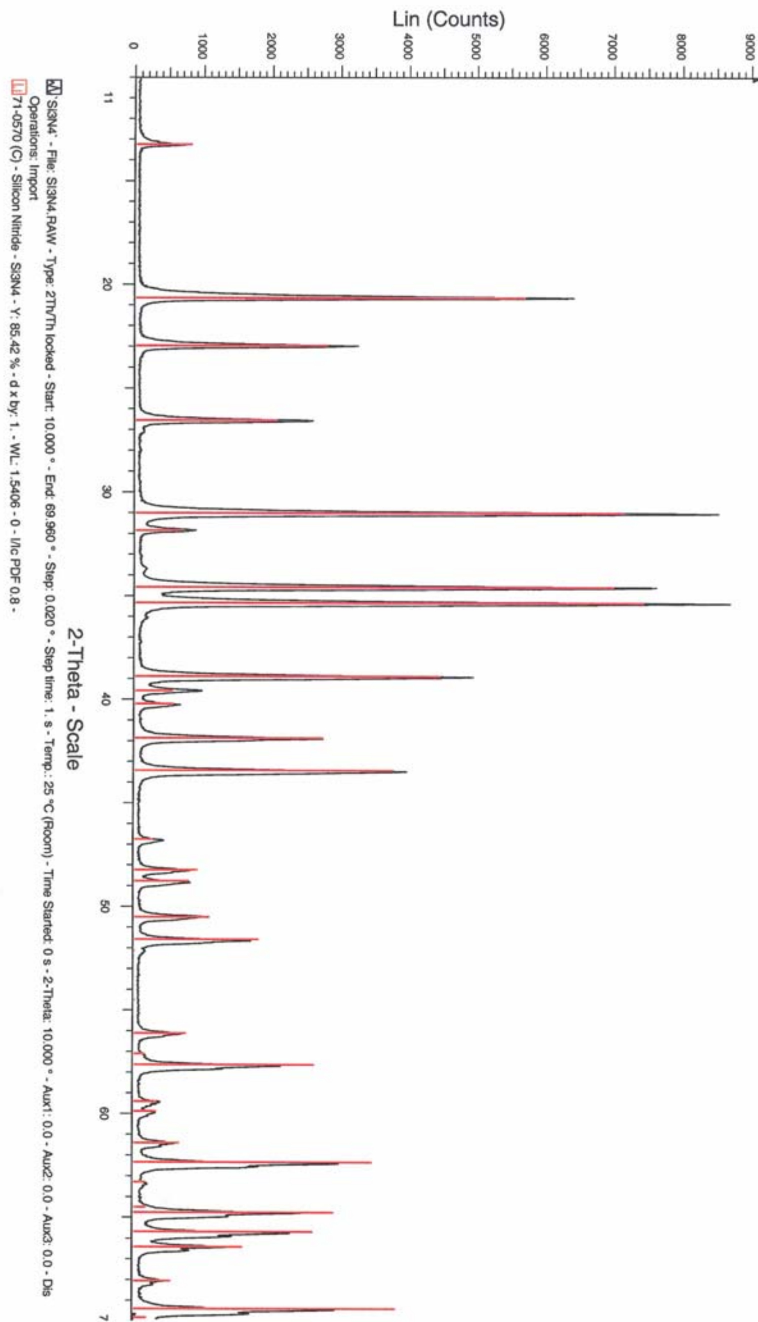

APPENDIX 2

X-ray diffractogram of coating after furnace run

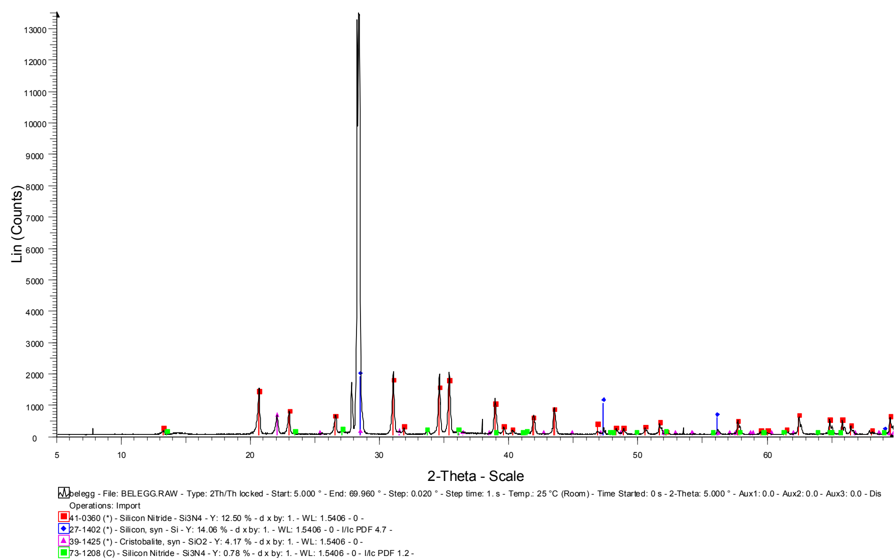

APPENDIX 3

SIMS-measurements of three melt samples.

Table A3•1: SIMS-measurements of three melt samples

Experiment	Sample	Fraction solidified	Carbon content / ppm mass
MS-Exp 1	10	0.66	34
MS-Exp 2	8	0.61	17
MS-Exp 2	1b	0	11

Areas of higher carbon contents were observed, but the analysis was performed away from these areas [Personal communications with Sukanta Biswas at Cascade Scientific]

APPENDIX 4

FTIR-measurements of the blocks (wafers) from the melt sampling experiments

Table A3•2: FTIR-measurements from MS-Exp 1 (Position 1, block 10, see Figure 4·8)

Fraction solidified, fs	Carbon content / ppma	Mean / ppma
0.02	7.18	7.21
	7.24	
0.12	7.87	7.98
	8.08	
0.23	10.46	10.20
	9.90	
0.33	11.61	11.97
	12.32	
0.4	16.80	16.98
	17.16	
0.49	15.99	15.85
	15.70	
0.53	13.82	14.09
	14.37	
0.59	10.95	11.21
	11.46	
0.66	10.61	10.54
	10.48	

Table A3•2: FTIR-measurements from MS-Exp 1 (Position 1, block 10, see Figure 4·8)

Fraction solidified, fs	Carbon content / ppma	Mean / ppma
0.73	10.50	10.95
	11.40	
0.81	9.47	9.63
	9.79	
0.90	9.12	9.37
	9.63	

Table A3•3: FTIR-measurements from MS-Exp 1 (Position 2, block 13, see Figure 4·8)

Fraction solidified, fs	Carbon content / ppma	Mean / ppma
0.02	6.10	6.09
	6.09	
0.23	7.97	8.26
	8.55	
0.40	12.11	12.12
	12.13	
0.53	12.65	12.76
	12.87	
0.66	10.49	10.52
	10.54	
0.81	9.84	9.83
	9.81	

Fraction solidified, f_s	Carbon content / ppma	Mean / ppma
0.02	6.35	6.40
	6.45	
0.23	8.38	8.38
	8.38	
0.40	10.71	10.75
	10.79	
0.53	10.29	10.29
	10.28	
0.66	9.79	9.76
	9.73	
0.81	9.32	9.28
	9.24	

Table A3•4: FTIR-measurements from MS-Exp 2 (Position 1, block 10, see Figure 4·8)

Fraction solidified, fs	Carbon content / ppma	Mean / ppma
0.04	5.02	5.03
	5.05	
0.15	7.33	7.39
	7.45	

Table A3•4: FTIR-measurements from MS-Exp 2 (Position 1, block 10, see Figure 4·8)

Fraction solidified, fs	Carbon content / ppma	Mean / ppma
0.25	9.17	9.17
	9.17	
0.36	10.26	10.25
	10.23	
0.48	11.67	11.68
	11.70	
0.57	11.95	12.03
	12.10	
0.64	13.85	13.78
	13.72	
0.76	10.13	10.25
	10.38	
0.83	9.70	9.80
	9.90	
0.92	9.49	9.31
	9.13	
0.95	9.03	9.04
	9.05	

Table A3•5: FTIR-measurements from MS-Exp 2 (Position 2, block 13, see Figure 4·8)

Fraction solidified, f_s	Carbon content / ppma	Mean / ppma
0.04	5.41	5.41
	5.41	
0.25	8.02	7.95
	7.88	
0.48	10.38	10.36
	10.34	
0.64	14.38	14.24
	14.10	
0.83	9.16	9.19
	9.23	
0.95	9.73	9.64
	9.55	

Table A3•6: FTIR-measurements from MS-Exp 2 (Position 3, block 13, see Figure 4·8)

Fraction solidified, f_s	Carbon content / ppma	Mean / ppma
0.04		
0.25	7.79	7.76
	7.74	

Table A3•6: FTIR-measurements from MS-Exp 2 (Position 3, block 13, see Figure 4•8)

Fraction solidified, f_s	Carbon content / ppma	Mean / ppma
0.48	12.58	12.62
	12.66	
0.64	11.10	11.10
	11.10	
0.83	9.07	9.12
	9.18	
0.95	11.18	11.16
	11.13	

Table A3•7: FTIR-measurements from MS-Exp 3 (Position 1, block 10, see Figure 4•8)

Fraction solidified, fs	Carbon content / ppma	Mean / ppma
0.02	5.59	5.58
	5.56	
0.12	7.91	7.87
	7.82	
0.24	9.19	9.25
	9.32	
0.36	11.40	11.41
	11.42	
0.48	12.27	12.19
	12.12	

Table A3•7: FTIR-measurements from MS-Exp 3 (Position 1, block 10, see Figure 4·8)

Fraction solidified, fs	Carbon content / ppma	Mean / ppma
0.60	10.47	10.45
	10.43	
0.72	9.66	9.62
	9.58	
0.84	8.74	8.81
	8.87	

Table A3•8: FTIR-measurements from MS-Exp 3 (Position 2, block 13, see Figure 4·8)

Fraction solidified, f_s	Carbon content / ppma	Mean / ppma
0.02	7.10	7.09
	7.09	
0.12	11.16	10.95
	10.73	
0.24	9.62	9.47
	9.33	
0.36	11.03	11.08
	11.12	
0.48	10.45	10.51
	10.56	
0.60	11.41	11.34
	11.26	

Table A3•8: FTIR-measurements from MS-Exp 3 (Position 2, block 13, see Figure 4·8)

Fraction solidified, f_s	Carbon content / ppma	Mean / ppma
0.72	9.42	9.43
	9.43	

Table A3•9: FTIR-measurements from MS-Exp 3 (Position 3, block 13, see Figure 4·8)

Fraction solidified, f_s	Carbon content / ppma	Mean / ppma
0.02	5.37	5.41
	5.45	
0.12	6.75	6.76
	6.76	
0.24	8.61	8.61
	8.61	
0.36	10.63	10.61
	10.60	
0.48	11.92	11.90
	11.88	
0.60	9.75	9.79
	9.83	
0.72	9.18	9.12
	9.07	

APPENDIX 5

Calculation of the mass transfer coefficient for the gas, k_g

Considering as an example the following gas flow and temperature;
Gas flow, V = 25 Nl/min at STP. At temperature 1673 K and 0.6 bar V = 0.0043 m^3/s
Temperature = 1400°C = 1673 K
Gas velocity, v_g = V/A = 0.0043 m^3/s /$(0.66m)^2$

Calculation of viscosity of the gas (Ar), μ:
The following relation from Bird *et al.* [1960] has been used for calculating μ:

$$\mu = 2.6693 \times 10^{-5} \times \frac{\sqrt{MT}}{\sigma^2 \Omega_\mu} \qquad \text{eq•6•1}$$

where M is the molecular mass of the gas, T the temperature, σ the collision diameter, Ω_μ is a slowly varying function of the dimensionless temperature $\kappa T/\varepsilon$ (κ is Boltzmann constant and ε is the maximum attractive energy between two molecules)

The following values are found for σ and Ω_μ found in “Transport Phenomena” by Bird *et al.* [1960] :

σ = 3.418 Å	from Table B-1
ε/κ = 124	from Table B-1
Ω_μ = ~ 0.796	from Table B-2
M = 39.948 g/mol	

Then inserting values in 6•1 gives $\mu = 7.42 \times 10^{-5}$ kg/ms.

The density, ρ, of the gas at the different P_{tot} is found from the ideal gas law where:
$n/V = P_{tot}/(RT)$ and $\rho = M \times (n/V)$

Calculation of the binary diffusivity of Ar-CO, $D_{Ar\text{-}CO}$:
The following relation from Bird *et al.* [1960] has been used for calculating $D_{Ar\text{-}CO}$:

$$D_{Ar-CO} = 0.0018583 \times \frac{\sqrt{T^3\left(\frac{1}{M_{Ar}} + \frac{1}{M_{CO}}\right)}}{P_{tot} \times \sigma^2_{Ar-CO} \times \Omega_{D, Ar-CO}} \qquad \text{eq•6•2}$$

where $\sigma_{Ar\text{-}CO}$ and $\varepsilon_{Ar\text{-}CO}$ can be estimated from: $\sigma_{Ar\text{-}CO} = 1/2 \times (\sigma_{Ar} + \sigma_{CO})$, and
$\varepsilon_{Ar\text{-}CO} = (\varepsilon_{Ar} \times \varepsilon_{CO})^{1/2}$

$\Omega_{D,\ Ar\text{-}CO}$ is a dimensionless function of the temperature and of the intermolecular potential field for one molecule of Ar and one molecule of CO. In “Transport Phenomena, Table B-2” it is calculated as a function of $\kappa T/\varepsilon_{Ar\text{-}CO}$

The following values are found for σ_{Ar-CO}, $\varepsilon_{Ar-CO}/\kappa$ and $\Omega_{D, Ar-CO}$ in “Transport Phenomena” by Birds *et al.* [1960]:

$\sigma_{Ar-CO} = 3.504$ Å

$\varepsilon_{Ar-CO}/\kappa = 116.8$ °K

$\Omega_{D, Ar-CO} \sim 0.7$

Using the information above the mass transfer coefficient for the gas, k_g, can be calculated for various total pressures, see Table Table A•5•1:.

Table A•5•1: Calculation of k_g

Calculated value	1 bar	0.6 bar	0.05 bar
ρ	0.29 kg/m^3	0.17 kg/m3	0.014 kg/m^3
$v_g = V/A$	5.8x10^{-3} m/s	1x10^{-2}m/s	1.16x10^{-1}m/s
$\nu = \mu/\rho$	2.6x10^{-4} m^2/s	4.4x10^{-4} m^2/s	5.3x10^{-3} m^2/s
D_{Ar-CO}	3.7 x 10^{-4} m^2/s	6.2x10^{-4} m^2/s	7.4x10^{-3} m^2/s
$Re = v_g L/\nu$	14.72	15	14.45
$Sc = \nu/D_{Ar-CO}$	0.70	0.71	0.72
$Sh = 0.68xSc^{1/3}xRe^{1/2}$	2.32	2.35	2.32
$k_g = Sh\ D_{Ar-CO}/L$	1.3x10^{-3}m/s	2.2x10^{-3} m/s	2.6x10^{-2} m/s

REFERENCES

R.B.Bird, W.E.Stewart and E.N.Lightfoot, *“Transport Phenomena”*, John Wiley and Sons, Inc., pages 23 and 511, 1960